Earthquake Geology, Hazard, Urban Form and Social Vulnerability

along the San Andreas Fault

by

Nathan A. Toké

A Dissertation Presented in Partial Fulfillment
of the Requirements for the Degree
Doctor of Philosophy

Approved May 2011 by the
Graduate Supervisory Committee:

J Ramón Arrowsmith, Chair
Christopher G. Boone
Arjun M. Heimsath
Everett L. Shock
Kelin X. Whipple

ARIZONA STATE UNIVERSITY

August 2011

ABSTRACT

The San Andreas Fault (SAF) is the primary structure within a system of faults accommodating motion between the North American and Pacific plates. Physical models of faulting and characterizations of seismic hazard are informed by investigations of paleoseismology, slip distribution, and slip rate. The impact of earthquakes on people is due in large part to social vulnerability. This dissertation contributes an analysis about the relationships between earthquake hazard and social vulnerability in Los Angeles, CA and investigations of paleoseismology and fault scarp array complexity on the central SAF.

Analysis of fault scarp array geometry and morphology using 0.5 m digital elevation models along 122 km of the central SAF reveals significant variation in the complexity of SAF structure. Scarp trace complexity is measured by scarp separation, changes in strike, fault trace gaps, and scarp length per SAF kilometer. Geometrical complexity in fault scarp arrays indicates that the central SAF can be grouped into seven segments. Segment boundaries are controlled by interactions with subsidiary faults. Investigation of an offset channel at Parkfield, CA yields a late Holocene slip rate of 26.2 +6.4/- 4.3 mm/yr. This rate is lower than geologic measurements on the Carrizo section of the SAF and rates implied by far-field geodesy. However, it is consistent with historical observations of slip at Parkfield. Paleoseismology at Parkfield indicates that large earthquakes are absent from the stratigraphic record for at least a millennia. Together these observations imply that the amount of plate boundary slip accommodated by the main SAF varies along strike.

Contrary to most environmental justice analyses showing that vulnerable populations are spatially-tied to environmental hazards, geospatial analyses relating social vulnerability and earthquake hazard in southern California show that these groups are not disproportionately exposed to the areas of greatest hazard. Instead, park and green space is linked to earthquake hazard through fault zone regulation. In Los Angeles, a parks poor city, the distribution of social vulnerability is strongly tied to a lack of park space. Thus, people with access to financial and political resources strive to live in neighborhoods with parks, even in the face of forewarned risk.

ACKNOWLEDGMENTS

This dissertation was supported by the National Earthquake Hazard Reduction Program grant: 07HQGR0094, the Southern California Earthquake Center geochronology fund, a Geological Society of America student grant, the Troy L. Péwé award for geomorphology, ASU's NSF IGERT in Urban Ecology grant: DGE-0504248, ASU's NSF GK-12 program: DGE-0538701, and follows upon NSF grant: EAR-0310357. The value of the IGERT in urban ecology program was realized through the provocative and the supportive network of student participants, IGERT faculty advisors, and administrators. Thinking outside of one's own disciplinary box often proves challenging, but it continues to inspire me. Interdisciplinary workshop collaborators provided inspiration as I progressed through my Ph.D. program. These workshops, Ed Hackett's ethics course, and Peggy Nelson's mentoring instruction contributed to my maturation as an interdisciplinary scientist. I would also like to thank Alyssa Johnson from Sun Valley Elementary for her patience with me as I worked toward translating scientific lingo into understandable 7th grade curriculum in the GK-12 program.

The multifaceted nature of this dissertation often stretched my multi-tasking abilities, but it was satisfying to experience true academic freedom and for that I thank my dissertation committee including Chris Boone, Everett Shock, Kelin Whipple, Arjun Heimsath, and especially my advisor Ramón Arrowsmith. Ramón was a consistently positive influence for me. Whenever I was feeling bogged down he helped me reflect on my accomplishments. I always walk away from a meeting with Ramón feeling ready to take on anything.

I am grateful to colleagues and friends whom I have shared research and learning experiences with. Including, but not limited to: Olaf Zielke, Erin DiMaggio, Laila El-Ashmawy, Angela Landgraf, Chris Crosby, Jeri Young, David Haddad, Melanie Busch, Josh Coyan, Mau Thayer, Megan Muretta, Lela Prashad, Jessica Block, Wendy Bohon, Kate Darby, Elizabeth Cook, Chris Mead, Troy Benn, Jennifer Brian, Rebecca Hale, Mark Neff, Kristi Diller, Kirsten Chojnicki, Roman DiBiase, JD, Christyanne Melendez, Alysa Snyder, Angela Bond, Sinan Akciz, Lisa Grant-Ludwig, Gabby Noriega, Antonio Azor, Michael Rymer, Steven Semken, Tom Sharp, Julia Johnson, Rick Hervig, Paul Bierman, Keith Klepeis, Andrea Lini, and Manfred Strecker. Many other friends and family members have provided an important support network as a graduate student, but are too numerous to name here.

Debjani Chakravarty helped me focus and relax throughout my last year at ASU. We enjoyed many voyages to the Superstitions for some geological respite. My father, Arun Toké, always inspires me as I work to gear my life towards social and environmental responsibility. My mother, Carolyn Garland, Naomi Goldenson, Doctors (Hao Fang, Adam Brodsky, and Stanford Ho) as well as many excellent people at Banner Good Samaritan Hospital helped me through a successful aortic valve replacement midway through my Ph.D. program. I am forever thankful. Finally, I am deeply indebted to my letter writers Ramón, Peggy, Chris, and Steve Semken who supported me through dozens of job applications. I am eagerly anticipating the start of my career as an Assistant Professor of Earth Science at Utah Valley University in fall 2011.

TABLE OF CONTENTS

CHAPTER Page

CHAPTER Page

APPENDIX

LIST OF TABLES

LIST OF FIGURES

Figure Page

CHAPTER 1

EXPANDING INTERDISCIPLINARY SOCIO-ENVRIONMENTAL RESEARCH RELATED TO THE EARTH SCIENCES

INTRODUCTION

Interdisciplinarity is the integration of disparate epistemologies (methods, models, and data sets) for the purpose of asking, understanding, and answering questions that would not arise from a disciplinary framework. This is the definition that I use when motivating integrative research. It is the product of numerous discussions related my participation in Arizona State University's (ASU) NSF Integrative Graduate Education and Research Training (IGERT) program in Urban Ecology (e.g., Grineski, 2003) and a workshop that I helped lead studying the implementation of interdisciplinary curriculum within new integrative schools (e.g., School of Sustainability) at ASU (Toké et al., 2009).

The underlying ethos of interdisciplinarity is central to my research. In this introduction I briefly review interdisciplinarity and its inherent role in sustainability science. This is followed by a short essay where I advocate the position that earth science research should continue to work toward societally-relevant contributions for the purpose of sustainability. Furthermore, where appropriate, these integrations should extend beyond the economic costs of geologic resources and hazards and should explore the implications of earth science research for health, social wellbeing, planning, and other aspects of social science. Finally, I outline the chapters of this dissertation, where I attempt to

follow my own advice about interdisciplinarity and societally-relevant research directions.

INTERDISCIPLINARITY AND SUSTAINABILITY SCIENCE

Interdisciplinarity can be conceptualized in numerous ways, but it is generally defined along a spectrum of varying levels of epistemological integration between disparate disciplines (e.g., Apostel, 1972; Klein, 1990; Klein, 1996; Lattuca, 2003; Morillo et al., 2003; Graybill et al., 2006; Aboelela et al., 2007; Miller et al., 2008; and Toke et al., 2009). A natural goal of interdisciplinary integration is knowledge synthesis for the advancement of scholarship and for the purpose of asking, understanding, and answering new questions, which would not arise from a single disciplinary framework. Thus, interdisciplinary research presents at least three compelling reasons for its prioritization: 1) It reveals and contextualizes knowledge that lies outside of the methodological bounds of current disciplines. 2) It may aide society to synthesize and integrate disciplinary-based academic knowledge for applications to *real world* complex socio-environmental problems. 3) It promotes sharing of disciplinary methods and tools which benefits scholars engaged in both interdisciplinary and purely disciplinary research and also promote more a holistic understanding of cross disciplinary research results and implications.

Interdisciplinarity has been largely contextualized within the history and politics of academic disciplines and the non-uniform structures of Universities which emerged through the secularization, rationalization, and categorization of

knowledge (e.g., Foucoult, 1972). Indeed, throughout humankind's millennial-scale quest to etch out disciplines and compartmentalize basic pieces of knowledge have been efforts to synthesize and integrate these pieces of knowledge and gain holistic understandings of socio-natural phenomena. Despite a nearly-geologic history of contrasting efforts to break down and build up knowledge, the term interdisciplinarity and theories about interdisciplinary education and research emerged only during the last century (e.g., Apostel et al., 1972; Klein, 1990).

Also surprising is that, even after forty years of interdisciplinary theory, interdisciplinarity within academic institutions is still considered relatively new and transformative. Even at institutions where interdisciplinarity pervades the academic culture, degrees are still predominantly awarded through disciplinary groupings and academic rewards look more favorably upon disciplinary contributions (e.g., Toke et al., 2009). That being said, within some circles, the notion of disciplines is antiquated and a state of transdisciplinarity or even post-disciplinarity pervades. Results from Lattuca's 2003 study revealed that a significant number of scholars look to bypass disciplines completely because they claim that there are too many important questions that lack compelling disciplinary ties.

Sustainability is a compelling discourse which does not have disciplinary ties and calls for integration of knowledge and action at many levels of society. The notion of sustainability comes from the realization that the planet Earth has limited resources and we may exceed its capacity to maintain desired societal and

ecological functioning. From this realization many goals have been set. At the heart of these goals is that society must meet the needs of today without compromising the ability of future generations to meet their needs (e.g., WCED, 1987). The relative role of science in meeting goals of sustainability is still uncertain. However, action within the scientific community has commenced and the field of sustainability science has emerged over the past decade (e.g., Miller, 2011).

Sustainability science is, by definition, interdisciplinary because it's motivations are driven by soceital needs which depend upon complex socio-environmental interactions and relationships. Complexity and interdisciplinary research are intertwined (e.g., Klein, 2004). Earth scientists have played a significant role within sustainability science thus far (e.g., Miller, 2011). This is especially true areound the arena of climate change and the related fields of atmospheric science, hydrology, paleoecology, glaciology, etc. However, climate change should, by no means, be the only integrating problem that draws earth science into issues of sustainability.

EARTH SCIENCE AND SOCIETY: BEYOND ECONOMY

If we do not heed the requirements of sustainability, and society meets its demise, it may mean little from a geologic perspective. Society has existed for only a small portion of the last epoch of the most recent geologic period. Thus, it could be tempting for Earth scientists to ignore the role of humans in the Earth system and focus only on the vast record of ancient environments. However,

society has managed to accomplish significant geologic work over our short tenure. We have significantly impacted rivers (e.g., Gregory, 2006), the atmosphere (e.g., Hansen et al., 1981), the ocean (e.g., Barnett et al., 2005), and the landscape (e.g., Wilkinson and McElroy, 2007). Not only is the subject of human influence on the Earth excellent fodder for high impact research, but basic Earth science knowledge also represents a vast library of past environmental scenarios and outcomes, which can be used to contribute to the discourse of decision making for sustainability.

Earth science research has value to society in the context of providing important resources, monitoring environmental change, and forecasting devastating hazards. These areas of research interface with the fields of planning, health, engineering, economy, and education. However, for obvious reasons, the impetus for societally-integrative Earth science research is usually the economy. This is especially true in resource extraction (how can we make more money?) and hazards research (how can we avoid losing money?). In my view, disproportionately directing interdisciplinary Earth science research within the context of maximizing economic returns does a disservice to the potential applications and contributions of the field, both in an academic sense and for sustainability. However, there is a lot of value in conducting hazards research for the purpose of improving engineering design and helping to set insurance rates, but we should not stop there. We can extend our hazards scenario assessments to move beyond financial impacts. In Chapter 2 of this dissertation, I show that there is a complex and important relationship between earthquake hazard, regulation,

social vulnerability, and urban form within the Los Angeles metropolitan region. This is only one example of how integrative analyses can reveal relationships that are important to consider for urban planning, disaster relief, engineering, and even basic science research. However, the value of this type of research is not often revealed until after it is completed.

Miller's (2011) dissertation on sustainability directions concludes with a call to action for sustainability science to become science of design. The crux of this idea is to organize sustainability science around four themes: creating desirable futures, promoting positive socio-technical change, developing sustainability values, and fostering social learning. It is hoped that this organization will lead science to describe its research in ways that can be used directly for democratic and pragmatic social action and thus sustainability goals.

I contend that a considerable amount of science has already been done that is not labeled as sustainability science, but is aligned with its goals. Obvious integrations between health and social science research (e.g., Rosenfield, 1992), does not call itself sustainability science. However, the goals and motivations within this type of research are aligned with sustainability. Likewise there are instances of integrative research between social science and earth science (e.g., Harlan et al., 2008) which do not claim to be sustainability science, but they are aligned with it. Earth scientists should not be bashful about using their tools, methods, and knowledge to participate in sustainability science. To do so, they would be wise to not limit themselves to single-minded goals related to monetary assessments. Sustainability is a complex issue. To advance sustainability science

at a desired pace our motivations and approaches to integrative socio-environmental research must be diverse and should attempt to consider how the outcomes from this research may enhance pragmatic action and decision making for sustainability.

OUTLINING THE CHAPTERS

The research presented herein covers topics in earthquake geology, fault zone geomorphology and structure, environmental justice, and urban geography. This dissertation is presented in the format of three main chapters which represent individual papers that are either published or in the preparation for publication. I begin by presenting a geospatial analysis of the relationships among earthquake hazard, fault zone regulation, urban form, and social equity in hazard exposure in Los Angeles, CA. This innovative chapter was submitted to the *Annals of the Association of American Geographers* and represents work directly resulting from my IGERT in urban ecology experience in which I worked to develop an additional research focus in urban environmental justice. The second chapter was written for and published as a *Geology* paper covering both paleoseismology and a slip rate estimation for the San Andreas Fault at Parkfield, CA. The third chapter presents LiDAR-based remote sensing analyses revealing how fault structure and complexity is manifest in the morphology and geometry of fault scarps along the central San Andreas Fault. This chapter was written for submission to the journal *Geosphere*. Appendices provide supplementary material related to these chapters. Finally, because materials herein have been published elsewhere, please follow

copyright rules and cite the following published and forthcoming articles appropriately:

Chapter 2: Toké, N.A., Boone, C.G., and Arrowsmith J R., Social vulnerability, earthquakes, and fault zone regulation in Los Angeles, California: environmental hazard or amenity? Submitted to *Annals of the Association of American Geographers* on June 25, 2011

Chapter 3: Toké, N. A., Arrowsmith J R., Rymer, M.J., Landgraf, A., Haddad, D.E., Busch, M., Coyan, J., and Hannah A., 2011, Late Holocene slip rate of the San Andreas fault and its accommodation by creep and moderate-magnitude earthquakes at Parkfield, California: Geology, v. 39, no. 3, p. 243-246.

Chapter 4: Toké, N. A., and Arrowsmith J R., Refining segmentation along the central San Andreas Fault using fault scarp array geometry and morphology from high resolution digital elevation models: In preparation for submission to *Geosphere*.

REFERENCES CITED

Aboelela, S.W., Larson, E., Bakken, S., Carrasquillo, O., Formicola, A., Glied, S.A., Haas, J., and Gebbie. K.M., 2007. Defining Interdisciplinary Research: Conclusions from a critical Review of the Literature: Health Services Research, v. 42, p. 329-344.

Apostel, L., Berger, G., Briggs, A., and Michaud,G., 1972, Interdisciplinarity: Problems of Teaching and Research in Universities: OECD Publications Center, Washington D.C.

Barnett, T.P., Pierce, D.W., AchutaRao, K.M., Gleckler, P.J., Santer, B.D., Gregory, J.M., and Washington, W.M., 2005, Penetration of Human-Indusced Warming into the World's Oceans: Science, vol., 309, no. 5732, p. 284-287.

Foucoult, M., 1972, The Archeology of Knowledge & The Discourse on Language: Translated from French by A.M. Sheridan Smith. Pantheon Books, New York, USA.

Graybill, J.K., Dooling, S., Shandas, V., Withey, J., Greve, A., and Simon, G.L., 2006, A Rough Guide to Interdisciplinarity: Graduate Student Perspectives: BioScience, vol. 56, no. 9, p. 757-763.

Gregory, K.J. 2006. The human role in changing river channels. Geomorphology, 79, 172-191.

Grineski, S.E., 2003, Toward an Integrative Urban Ecology: Voices from the IGERTs: Bulletin of the Ecological Society of America, Commentary, October 2003, p. 200-205.

Hansen, J., Johnson, D., Lacis, A., Lebedeff, S., Lee, P., Rind, D., and Russel, G., 1981, Climate Impact of Increasing Atmospheric Carbon Dioxide: Science, vol., 213, no. 4511, p. 957-966.

Harlan, S.L., Brazel, A.J., Jenerette, G.D., Jones, N.S., Larsen, L., Prashad, L., and Stefanov, W.L., 2008, In the shade of affluence: the inequitable distribution of the urban heat island, in Equity and the Environment: Research in Social Problems and Public Policy, Volume 15, Wilkinson R.C. and Freudenburg W.R. (eds.): Emerald Group Publishing Limited, p.173-202

Hooke, R. LeB. 1994. "On the efficacy of humans as geomorphic agents" GSA Today, 4, No. 9, 224-225.

Klein, J.T., 1990, Interdisciplinarity: History, Theory, and Practice: Wayne State University Press. Detroit Michigan.

Klein, J.T., 1996, Crossing Boundarie: Knowledge, Disciplinarities, and Interdisciplinarities: University Press of Virginia, Charlottesville, Virginia

Klein, J.T., 2004, Interdisciplinarity and complexity: An evolving relationship. E:CO: 2-10.

Lattuca, L.R., 2003, Creating Interdisciplinarity: Grounded Definitions from College and University Faculty: History of Intellectual Culture, vol. 3, p. 1-20.

Miller T.R., Baird, T.D., Littlefield, C.M., Kofinas, G., Chapin III, F.S., and Redman, C.L., 2008, Epistemological Pluralism: Reorganizing Interdisciplinary Research: Ecology and Society, vol. 1, no 2, p. 46.

Miller, T.R., 2011, Constructing Sustainability A Study of Emerging Scientific Research Trajectories, Dissertation: Arizona State University.

Morillo F., Bordons, M., and Gomez. I., 2003, Interdisciplinarity in Science: A Tentative Typology of Disciplines and Research Areas: Journal of the American Society for Information Science and Technology, vol. 54, p. 1237-1249.

Rosenfield, P. L., 1992, The Potential of Transdisciplinary Research for Sustaining and Extending Linkages between the Health and Social Sciences: Social Science & Medicine, vol. 35, p. 1343–1357.

Toké, N. A., K. Darby, E. Cook, C Mead, J. Brian, T Benn, S. Fisher, C.G. Boone, and S. Semken, 2009, Pedagogy in interdisciplinary higher education: an investigation of faculty and student perspectives: Annual Geological Society of America Meeting, Abstracts with Programs, vol. 41, no. 7, Portland, Oregon, October 18-21st.

Wilkinson, B.H., and B.J. McElroy. 2007. The impact of humans on continental erosion and sedimentation. GSA Bulletin, 119, 140-156.

World Commission on Environment and Development (WCED), 1987, Our common future: Oxford University Press, New York.

CHAPTER 2

SOCIAL VULNERABILITY, EARTHQUAKES, AND FAULT ZONE REGULATION IN LOS ANGELES, CALIFORNIA: ENVIRONMENTAL HAZARD OR AMENITY?

ABSTRACT

Public perception and regulation of environmental hazards are important factors in the development and configuration of cities. Throughout California, probabilistic seismic hazard mapping and geologic investigations of active faults have spatially quantified earthquake hazard. In Los Angeles, these analyses have informed earthquake engineering, public awareness campaigns, the insurance industry, and the government regulation of developments near faults. Understanding the impact of natural hazards regulation on the social and built geography of cities is vital for informing future science and policy directions. We constructed a relative social vulnerability index for Los Angeles to examine the social condition within regions of significant seismic hazard; including areas regulated as Alquist-Priolo (AP) Act earthquake fault zones. Despite hazard disclosures, social vulnerability is lowest within AP regulatory zones and vulnerability increases with distance from them. Because the AP Act requires building setbacks from active faults, newer developments in these zones are bisected by parks. Parcel-level analysis demonstrates that homes adjacent to these fault zone parks are the most valuable in their neighborhoods. At a broader scale, a Landsat-based normalized difference vegetation index shows that greenness

near AP zones is greater than the rest of the metropolitan area. In the parks-poor city of Los Angeles, fault zone regulation has contributed to the construction of park space within areas of earthquake hazard, thus turning these zones of hazard into amenities, attracting populations of relatively high social status, and demonstrating that the distribution of social vulnerability is sometimes more strongly tied to amenities than hazards.

INTRODUCTION

Environmental hazards, such as toxic release and storage facilities, are burdens born usually by racial and ethnic minorities and the poor (United Church of Christ Commission for Racial Justice, 1987; Harvey, 1997; Brulle and Pellow, 2006; Mohai and Saha 2007; Downey 2007). The uneven and inequitable patterns are products, in part, of power structures where socially vulnerable groups (Cutter, 1996; Cutter et al., 2003) do not have equal political voice or economic power in controlling where such facilities are located (Schlosberg, 2007). Various forms of discrimination, from overt to unintentional, can lead to these types of environmental inequities (Pulido 2000; Bolin, Grineski, and Collins, 2005). In Los Angeles, a documented history of discriminatory decisions and institutions has led to poor and minority communities living near a disproportionate concentration of toxic release and storage facilities (e.g., Modarres, 1998; Boone and Modarres, 1999; Pulido 2000). Pulido (2000) documented evidence of institutional racism in Los Angeles that enforced the

spatial link between toxic facilities and minorities in the inner city while privileged whites migrated outward to suburbanizing areas.

In addition to being subjected disproportionately to industrial pollution, poor and minority groups are often not afforded equal access to environmental amenities (Boone, 2008) such as parks and open space (Cutts et al., 2009). In rare cases where minority groups are afforded better access to an amenity, such as park space, it is sometimes an unintended consequence of other forms of discrimination (Boone et al., 2009). As an urban area, Los Angeles has relatively limited park space. This disadvantage is exacerbated for poor populations who live in denser neighborhoods with more crowded parks (Wolch et al., 2005; Sister et al., 2009). Moreover, poor people may not have access to transportation allowing them to seek out more distant open spaces.

An important consideration for the wellbeing of Southern Californians is exposure to natural hazards, including wildfires, landslides, and earthquakes. Wildfires are common due to the region's dry Mediterranean climate (Westerling et al., 2004) and are linked to landslides, including debris flows, and intense seasonality of rainfall (Cannon et al., 2007). Both of these hazards are primarily confined to the mountainous topography at the edge of the urban area. This rugged topography is due to its location within a geometrically complex section of the San Andreas Fault system, the transform plate boundary between the North American and Pacific tectonic plates (Wallace, 1990). Near Los Angeles, the San Andreas Fault system makes a large left bend which results in compressional uplift along the right-lateral fault. The uplift of rocks moving through this bend

has created spectacular topographic relief, including the San Gabriel and San Bernardino Mountains which can been seen looming more than 10,000 feet above sea level on a low pollution day. These dynamic landforms are the product of motion along the numerous active and hazardous faults comprising the plate boundary system (Dolan et al., 1995). Over the past 150 years the Los Angeles metropolitan region has expanded to more than 15 million people, filling the valleys between the Pacific Ocean and the mountain fronts and crossing many active faults during suburban expansion (Fig. 2.1).

California is one of the few places in the world where building development is regulated based upon earthquake hazard. Following significant surface rupture and damage in the 1971 San Fernando earthquake (U.S. Geological Survey, 1971; Proctor et al., 1972), the state passed the 1972 Alquist-Priolo (AP) Act (Hart and Bryant, 1997; California Geological Survey, 2001). The AP Act was a response to the realization that surface ruptures often occur during large earthquakes (Wells and Coppersmith, 1994) and that these multi-meter breaks in the landscape can be severe, resulting in structural failure of overlying buildings. The purpose of the Act is to eliminate the loss of homes and associated casualties from surface rupture by not building directly over active faults. Because geomorphology and geology provide long-lasting evidence of prehistoric earthquakes and the location of active fault traces, the AP Act designates the mapped surface traces of these faults as "Special Study Zones" and mandates that developers use consultants to cite houses more than fifty feet away from fault traces within these zones. Real estate agents are also required to

disclose information about the location of homes within the regulatory areas to potential buyers. In 1994, following Reitherman and Leeds' 1991 evaluation of the AP Act, the name "Special Study Zones" was replaced by "Earthquake Fault Zones," a more accurate reflection of the earthquake hazard.

An earthquake is the release of energy when a fault slips in response to tectonic stress overcoming the frictional strength of fault zone materials (Reid 1910). This energy release takes the form of seismic waves. Moderate to large earthquakes along faults located near population centers can shake the Earth's surface with Peak Ground Accelerations (PGA) that approach or exceed gravity (Allen et al., 2008). Buildings are primarily constructed to withstand the downward acceleration of gravity and not strong horizontal ground accelerations which can shear structural supports and cause failure. Building failure is the primary cause of fatalities for non-tsunami-generating earthquakes (Bilham, 2009). Secondary reasons for fatalities include fires, as happened following the 1906 San Francisco Earthquake (Lawson, 1908), and a lack of access to basic medical treatment, food, and shelter which can lead to delayed earthquake deaths (Mulvey et al., 2008; Kolbe et al., 2010). The likelihood of building failure increases with ground motion (holding engineering constant). Therefore the areas of greatest primary hazard are where ground motions are the strongest.

The primary way that geoscientists characterize earthquake shaking hazard is through probabilistic seismic hazard analyses (Petersen et al., 2008; Fig. 2.3A). This is a deterministic process that evaluates the earthquake potential for all nearby faults and calculates the peak shaking levels that might be expected at a

particular location given a probability level and time span (e.g., a 10% chance of occurrence in the next 50 years). These types of analyses (Field et al., 2008) consider empirical and physical models of earthquake processes, occurrence, and the attenuation of seismic waves (Gutenberg and Richter, 1944; Wells and Coppersmith, 1994; Hanks and Bakun, 2002; and Trifuniac, 1976). Additionally, much of the data which goes into seismic hazard models comes from geologic investigations of earthquake recurrence rate (Dolan et al., 2000; Akciz et al., 2010; Scharer et al., 2010), slip rate (Behr et al., 2010; Toké et al., 2011), fault segmentation (Machette et al., 1991), and the distribution of slip in past earthquakes (Arrowsmith et al., 1998; Zielke et al., 2010).

The attenuation of seismic energy depends mostly on the distance from the earthquake source, but also on local surface materials and topography (Trifuniac, 1976). The areas that experience the greatest shaking are often those closest to the fault that ruptured. Thus, while the AP Act presents regulations that are designed to address the hazard of surface rupture, these zones are also spatially associated with the greatest risk of severe ground shaking.

Regulated environmental hazards, such as toxic release facilities, are associated with discriminatory practices that lead politically-weak groups to be disproportionately exposed to the hazards (e.g., Boone and Modarres 1999; Pulido, 2000; Wilson et al., 2008). Those who lack political and economic power are also the most socially vulnerable populations to environmental disasters (Cutter, 1996; Bolin with Stanford, 1998; Cutter et al., 2003). Therefore, because earthquake fault zones are regulated as a hazard there is reason to suspect that

discriminatory practices might push the socially vulnerable to live near these regulated zones of hazard. To test this hypothesis we developed a 20 factor social vulnerability index (Table 2.2) for the Los Angeles metropolitan area using census block group data, and spatially analyzed the distributional relationships among social vulnerability, seismic hazard, and the AP fault zones (Fig. 2.3). To our surprise, the analyses show that privileged (low social vulnerability) populations live closest to the seismic hazard (Fig. 2.4A). To explain this result we use aerial photographs to assess the urban morphology of AP zones. We identified and mapped a number of parks within the AP regulatory zones (Fig. 2.5). We show that parcel values nearest to these fault zone parks are the highest within their respective neighborhoods (Fig. 2.6). Additionally, we use a normalized difference vegetation index to assess the greenness of AP zones relative to the entire urban area (Fig. 2.4B and Figs. 2.7-2.8). This analysis shows that the amenities of open space, greener neighborhoods, and parks outweigh the apparent hazard of seismicity in the lifestyle choices made by privileged southern Californians. The AP Act, designed to identify and regulate earthquake hazards, unintentionally generated urban environmental amenities.

A SOCIAL VUNLNERABILITY INDEX FOR LOS ANGELES

A population's vulnerability to an environmental hazard is only partially due to direct exposure. With enough resources people can prepare for the risks posed by a hazard which may allow them to cope with the effects of an associated disaster. Therefore, we define social vulnerability as a measure of a group's

relative ability to prepare for, cope with, and adapt to the effects of an environmental stressor such as a devastating earthquake. This definition is aligned with Cutter's (1996) "hazard of place model" and other conceptual models that account for people's resilience to a hazard in addition to the physical effects of the hazard (Turner et al., 2003; Cutter et al., 2003; Wood et al., 2009). The impact of relative social vulnerability on the outcome of seismic disasters is well illustrated by comparing casualty rates from the 2010 Haiti earthquake and other recent large earthquakes (Table 2.1). In Haiti, a third world country without significant resources for earthquake mitigation, approximately 7% of the population exposed to extreme ground shaking lost their lives. This is in stark contrast to other recent large earthquakes in Japan, Chile, and New Zealand where casualty rates were less than 0.5% of the population exposed to similarly strong ground shaking.

In our analyses, we follow the approach of Cutter et al. (2003) to quantify the spatial distribution of social vulnerability in Los Angeles. In their 2003 paper, the authors drew from literature about social indicators for quality of life and used county level data from the 1990 United States Census to develop a national social vulnerability index. Their census-based calculation was organized around metrics accounting for six major components that influence social vulnerability: 1) ***access to resources*** to prepare for and cope with a disaster (e.g., financial, food, education, and technology), 2) ***access to political power and representation*** to help distribute resources among the population, 3) ***social capital,*** which can help with coping after a disaster (e.g., social networks, connections, and integration of beliefs), 4) ***building stock*** (e.g., quality and age), 5) ***density of the built***

environment, and the 6) ***physical limitations of individuals*** (e.g., disabilities and frailty from age). Because there are many census-based metrics that can be used to account for these components of the social condition, they used multicollineartity tests and principal component analysis to identify 11 census metrics that accounted for most of the variability among more than 250 metrics that were initially considered. They used an additive model for each of their 11 metrics to calculate a social vulnerability index score for each county in the United States.

To develop a social vulnerability index specifically for the Los Angeles metropolitan area and the hazard of earthquakes we grouped the 11 metrics used by Cutter et al. (2003) into 7 categories representing social condition and vulnerability (Table 2.2): personal wealth, age and dependency, density of the built environment, housing stock and tenancy, under-represented groups, local economy, and infrastructure dependence . For each of these categories we used 2-3 census metrics to form a twenty factor relative social vulnerability index for Los Angeles (hereafter called LA-SoVI: Fig. 2.4A and Tables 2.2-2.3). The LA-SoVI was created at the census block group level, which provides an appropriate scale for comparison with geospatial representations of earthquake hazard (Fig. 2.2).

Calculating the LA-SoVI for each census block group (US Census Bureau, 2000) is a multistep process. For each of the twenty factors, we normalized their values by calculating each census block group's deviation from the city-wide mean. Using that deviation from the mean, we calculated five classes of natural breaks for each factor. Because we used the deviation from the mean, natural

breaks are both negative and positive. The natural break class whose range straddles the city-wide mean was assigned a value of 0. For each natural break above the mean (more vulnerable) or below the mean (less vulnerable) the factor value increases or decreases by 1. This method produced factor values ranging from -2 to 2 or -1 to 3 depending on the skew of each factor's histogram. Several of these histograms are skewed positively (more vulnerable) because poor people vastly outnumber wealthy. Next, we averaged the factor values within each of the seven categories of social condition (Table 2.2 and Fig. 2.3B-H), producing seven index scores (Table 2.3). The values for these seven indices were then averaged, producing a raw LA-SoVI score. Because some categories of the social condition are anti-correlated (i.e., retirement communities may be wealthy), the range of these census block group averages is -1.26 to 1.43, rather than the full range of natural break values for individual factors (-2 to 3). Finally, we performed an additional natural breaks transformation so that the final LA-SoVI values are integers ranging from -2 to 2 (Fig. 2.4).

It is important to remember that the LA-SoVI is a normalized index for this metropolitan area and says nothing about the relative vulnerability of a census block group in Los Angeles compared with one in another city such as Seattle. However, this type of analysis could be extended for larger regions as was done for county level data in Cutter et al. (2003). For the purposes of this paper, we focus on social vulnerability rather than economic vulnerability due to the cost of reconstruction or other commonly considered metrics by literature related to earthquake risk and loss (e.g., Rashed and Weeks, 2003).

DEFINING EARTHQUAKE HAZARDS

The most spatially comprehensive effort to disseminate earthquake hazards information has been through probabilistic seismic hazard maps (Petersen et al., 2008; Field et al., 2009). These mapping efforts have been partially motivated by needs to establish safe building codes and set appropriate rates for earthquake insurance. These maps are constructed by expert opinion and collaborative compilation of seismic, geodetic, and geologic data into spatially explicit models by government and academic scientists (Marzocchi and Zechar, 2011). In addition to helping set regulations, these models have led to synthesis that has helped drive new data gathering efforts to improve and refine the understanding of earthquake hazards and science.

To differentially evaluate which regions are more at risk from earthquake shaking hazard, we used probabilistic ground motion maps. The 2008 national probabilistic seismic hazard mapping (Petersen et al., 2008) captures most of what is known about potential earthquake sources and attenuation of ground motions (e.g., Trifuniac 1976). However, these maps are works in progress which undergo periodic review and revision. Earthquake scientists still do not know the rates of motion or earthquake histories for some faults. In these cases inferences are made for seismic source characterization. Additionally, while we know how ground motions attenuate away from earthquake sources, we do not have many records of ground motions nearby faults in large earthquakes and current models do not do a good job of accounting for local amplification of ground motions (e.g., Petersen,

2008). That being said, this data set is the best available way to capture the spatial variability of risk due to extreme ground motion in earthquakes.

In addition to extreme ground shaking, earthquakes can cause fault surface ruptures that can physically tear a structure apart. This hazard is best captured by the boundaries of the AP Act itself which is defined by the risk of surface rupture (California Geological Survey, 2001). There are other environmental hazards related to earthquakes including triggered landslides, dam failures, flooding, loss of lifelines, and fire (California Geological Survey, 2008). However, these hazards are strongly coupled to seismic shaking and fault rupture, which are the two physical hazards we consider in this analysis.

METHODOLOGY

This study relies heavily upon GIS analyses. We spatially characterize earthquake hazard using shape files of probabilistic seismic hazard and AP earthquake fault zones. AP maps were obtained from the California Geological Survey (2001) and probabilistic seismic hazard maps were obtained from the US Geological Survey's Interactive Hazards Maps (U.S. Geological Survey, 2008). This data set originates as a 0.05 degree grid for the conterminous 48 US States. However, it is delivered as a polygon shape file based on contours of equal ground motion. We selected the highest probability of exceedance (10% probability in the next 50 years) and the hazard metric of peak ground acceleration for the analyses. Because all of Los Angeles has significant risk of seismic ground shaking (Fig. 2.3A), we trimmed the data set to areas with a

greater than 10% probability of exceeding peak ground accelerations of more than 60% of gravity (or 5.88 m/s^2). This level of ground motion correlates with Modified Mercalli Intensities (MMI) greater than VIII (Wald et al, 1999). The MMI scale is an empirical scale that describes the damage and felt effects experienced from ground shaking in an earthquake (Wood and Neumann, 1931). Modified Mercalli Intensities greater than VIII are characterized by violent shaking and heavy infrastructure damage. Therefore, peak ground accelerations greater than 60% of gravity is the appropriate level to characterize the regions of greatest shaking hazard.

We used buffering analyses to identify census block groups that intersect the areas of extreme ground shaking hazard and the AP Act regulatory zones. Then we compared the social vulnerability of those block groups to the greater Los Angeles region. Additionally, because not all active faults are designated as AP zones we also performed LA-SoVI analyses for census block groups with portions of their boundaries within 1 km of non-AP faults. Finally, to compare the hazard of earthquakes to that of toxic release inventory (TRI) sites we assessed the LA-SoVI of census blocks groups within one kilometer of TRI sites. For each analysis, LA-SoVI values were converted to the census block group scale (Fig. 2.4A) and then census block group values were averaged for each spatial unit of analysis (Table 2.3). To provide context to these tabulated results, we also tabulated index values for the most and least socially vulnerable census block groups.

Social vulnerability and areas of greatest earthquake hazard are anti-correlated and AP regulatory zones have among the lowest LA-SoVI index values within the urban area. To explain this result we assessed the urban morphology of AP zones, including the location of urban amenities such as parks and greenspace (Fig. 2.4B and Fig. 2.5). To approximate relative greenness over the entire metropolitan area we constructed a normalized difference vegetation index (NDVI: Tucker, 1979) using spring 2000 Landsat scenes; matching the Census year and allowing us to estimate census block group greenness during the growing season. A Landsat-derived NDVI is the quotient of the difference between band 4 (near infrared) and band 3 (visible red) and the sum of band 4 and band 3, yielding values between -1 and positive 1. Because green plants reflect near infrared radiation strongly and absorb wavelengths corresponding to visible red, positive NDVI values indicate an abundance of green plants and negative values are associated with other land cover types. NDVI values for census block groups within the Los Angeles metropolitan area are generally negative because they are urban, but we interpret less negative values to indicate areas with relatively more greenspace. Areas with high social vulnerability have the most negative NDVI values (Fig. 2.7) and areas associated with active faults are the greenest (Table 2.3). We used air photos to assess the urban morphology within AP fault zones which led us to identify at least five areas of formal park space that are directly tied to fault zone regulation and tectonic geomorphology (Figs. 2.5-2.6). For two of these parks we assessed the spatial relationship between AP fault zones, parks, and parcel values.

DISTRIBUTION OF SOCIAL VULNERABILITY AND EARTHQUAKE HAZARD

Social vulnerability in the Los Angeles metropolitan region (LA-SoVI: Fig. 2.4A) is greatest between downtown Los Angeles and the Newport-Inglewood fault zone to the south and west of the city. This area is known as south-central Los Angeles and includes hundreds of census block groups with LA-SoVI values of 2. East Los Angeles and Long Beach, CA also have very large concentrations of the socially vulnerable. Additional areas with significant numbers of socially vulnerable block groups include the cities of Ontario, Pomona, San Bernardino, Santa Ana, Van Nuys, and West Covina (Fig. 2.4A). These areas have LA-SoVI values approaching 2, whereas the mean LA-SoVI for the metropolitan region is -0.11 (Table 2.3).

Earthquake shaking hazard is concentrated along the largest faults with the greatest slip rates (the San Andreas, San Jacinto, Raymond, Elsinore, and Sierra Madre Faults: Figs. 2.1 and 2.4A). These faults are located along the edges of the urban area and near areas of significant topographic relief. With the exception of the San Jacinto, the areas with the greatest risk for extreme ground shaking are not spatially linked with the census block groups that have high social vulnerability. The areas of high shaking hazard have a mean LA-SoVI of -0.28 (Table 2.3).

Census block groups that cross AP regulatory zones have among the most negative LA-SoVI values (Table 2.3 and Fig. 2.4A) in the metropolitan area indicating that AP zones are areas of low social vulnerability where people have

good access to resources and representation (Fig. 2.3). Of the nearly two dozen mapped faults with significant earthquake potential (Fig. 2.1) only two faults (the Newport-Inglewood and San Jacinto) intersect areas of high social vulnerability and are designated as AP earthquake fault zones. These two cases present an uncommon situation where the faults cut through basins and are not associated with mountain fronts. As a result, these areas were developed early in the region's history, prior to enactment of the AP regulation, and they cut through a diverse range of neighborhoods. Where these faults are associated with neighborhoods of high social vulnerability, they are also associated with industrial zones related to airports, railways, and other associated industrial facilities.

Census block groups along active faults that are not regulated by the AP Act (Fig. 2.1) have slightly more negative mean LA-SoVI values than those near AP zones (Table 2.3). Most of these unregulated faults were already developed prior to the AP Act (Fig. 2.5A). These unregulated areas include the Hollywood Fault and Santa Monica Fault, which are extensions of the Raymond Fault, which is regulated by the AP Act and has one of the highest slip rates in the metropolitan area. Additionally, geologic investigations have shown evidence for activity along the Hollywood and Santa Monica faults (Dolan et al., 1995 and Dolan and Rockwell, 2000). Thus, it is curious why these particular areas are not included as AP earthquake fault zones. Regardless of the reason that these areas are not zoned, the reason that their social vulnerability index values are lower is that they have greater personal wealth, a better local economy, and a lower proportion of

underrepresented groups (Table 2.3). Perhaps, the wealthy people living along these faults have the political power to avoid regulation.

EARTHQUAKE REGULATION, TRI SITES AND GREENSPACE

Many environmental justice analyses, including several within Los Angeles, have shown a geographic link between toxic release inventory facilities (TRI sites), minorities, and the poor (Modarres, 1998; Boone and Modarres, 1999; Pulido 2000). Comparing the locations of TRI sites (Fig. 2.4B) and areas of high LA-SoVI (Fig. 2.4A), we see the same result (Table 2.3). The average LA-SoVI value of census blocks located within one kilometer of a TRI site is 0.38 indicating a significant association between social vulnerability and this environmental hazard. The TRI average is nearly a full LA-SoVI index point higher than the mean value for census block groups that cross AP fault zones (-0.55) and nearly half an index value more than the entire metropolitan region (Table 2.3).

TRI facilities are generally associated with industrial zones and thus are areas of relatively little greenspace (Fig. 2.4B). The average NDVI of census block groups located within one kilometer of TRI sites is quite negative (-0.199: Table 2.3). This value is half a standard deviation more negative than the Los Angeles mean (-0.169) and one standard deviation more negative than the NDVI for block groups in areas of probable extreme ground motion (-0.140). While areas with high risk for extreme ground shaking have relatively high amounts of greenspace, census block groups that cross AP zones have the least negative

NDVI value for any of the units of analysis considered. In contrast, block groups with highest social vulnerability are associated with the most negative NDVI values, half a standard deviation more negative than block groups associated with TRI sites (Table 2.3).

Social vulnerability, as described by the LA-SoVI, is strongly linked to NDVI, our proxy for urban greenspace (Fig. 2.7). This is well illustrated using a step-wise analysis of census block group values with block group distance from AP zones (Fig. 2.8). In this analysis we plot values for LA-SoVI, NDVI, and mean elevation above sea level for all block groups crossing AP zones, all that are 1 block group from AP zones, 2 block groups from AP zones, and continuing on until all block groups within the urban area have been considered. In this analysis, no block groups are counted more than once. The plots of mean LA-SoVI and NDVI with distance from AP zones are nearly mirror images of each other (Fig. 2.8). The lowest social vulnerability and greenest block groups are those that cross AP zones. Mean social vulnerability index values increase with census block group distance from AP zones. Within the first 3 block groups from AP zones index values are negative, indicating above average social status. Over these same census block group distances, NDVI values are greater than the citywide average (-0.169: Table 2.3), indicating above average amounts of greenspace. However, for the next 11 block groups away from AP zones LA-SoVI index values are positive, indicating higher social vulnerability, and correspondingly NDVI values drop below the citywide average. Finally, at the farthest block groups from AP zones (15-18, displayed as an average at point 15

on Fig. 2.8), LA-SoVI values are again negative and NDVI values mirror this. The positive changes in greenspace and social status farthest from AP fault zones is because many of these block groups are located near the coast.

THE AP REGULATION AND PARK SPACE

NDVI comparisons show that AP regulatory zones are among the greenest areas of the metropolitan area. This may be partially due to AP fault zones being located along mountain fronts where precipitation and runoff are greater (Fig. 2.1) and because fault zones are often hydrologic barriers associated with vegetation lineaments. However, comparing the NDVI values of AP fault zones to other, unregulated, active faults (Fig. 2.1) we see that values are significantly greater in AP zones (Table 2.3), indicating that they are greener than unregulated faults.

One of the primary differences between unregulated faults and AP fault zones is the density of the built environment (Table 2.3). Housing density in census block groups along AP zones is the lowest of all the spatial units considered. This is not surprising if we consider the setback regulations associated with the AP Act (Hart and Bryant, 1997). The regulation states that homes can be built within AP zones, but they must be set back at least 50 feet from any identified surface traces of active faults, as determined by engineering geology consultants. Because the surface expressions of faults are rarely singular fault planes, this regulation precludes a significant amount of land within AP zones from being developed for homes. To investigate this further we used aerial photography to assess the urban morphology of AP zones.

Visual inspection of aerial photography along AP zones led us to identify five areas where setback regulations and tectonic geomorphology have played a role in the creation of urban park space (Fig. 2.5). All of the sites where AP regulations resulted in fault zone parks were constructed after 1970, when earthquake engineering codes and regulations began to take effect (Fig. 2.5A). Fault zone parks consist of open greenspace with water features (Fig. 2.6A), greenspace with landscaping (Figs. 2.6B), named parks with amenities such as the Pacific Ocean views from Hilltop Park along the Newport-Inglewood fault (Fig. 2.5C), community recreation facilities like those in a neighborhood in Huntington Beach, CA (Fig. 2.5D), or a golf course along the Chino Fault (Fig. 2.5B).

The impact of fault zone parks on neighborhood greenspace values is obvious. Parks and open space can also be seen as valuable amenities for their health benefits (Bedimo-Rung et al., 2005) especially in the Los Angeles region where urban park space is relatively limited (Wolch et al., 2005 and Sister et al., 2009). To gain a first order understanding of how fault zone park space is perceived by surrounding neighborhoods we used the County of San Bernardino Assessor's Office 2010 GIS databases to assess parcel value in two communities with AP zone park space. Along the San Andreas Fault near Highland, CA suburban expansion crossed the AP zone after 1992 (Fig. 2.6A). Because of setback regulations, a narrow strip of park space extending for more than a kilometer in length along the San Andreas Fault is bordered by residential neighborhoods. The fault zone park is landscaped, irrigated, has a walking path, and a reservoir with a fountain. The space is also associated with a community

recreation center which includes a pool. When normalized for area, parcels located nearest to the AP fault zone park space are the most valuable in this neighborhood. Many of these parcels are greater than 1.5 standard deviations more valuable than the neighborhood mean. This same relationship is observed at the AP fault zone park along the San Jacinto fault (Fig. 2.6B).

Higher property values near earthquake fault zone parks suggest these zones are perceived as neighborhood amenities. Even in Long Beach, where many industrial facilities are located, a fault zone park can positively impact the social condition of the neighborhood (Fig 2.5C). Here a step-over along the right-lateral Newport-Inglewood fault has resulted in tectonic uplift forming a small hill which is covered by a residential development and a municipal park named Hilltop Park. Aerial photography suggests that the homes here are larger than average for the surrounding neighborhood and are associated with more greenspace. The La-SoVI of the census block group associated with this fault step over is -2 (the lowest social vulnerability index value: Fig. 2.4A). Amazingly, this small pocket of social wellbeing is situated directly between TRI sites and industrial complexes associated with Long Beach International Airport and some of the most socially vulnerable census block groups in the entire metropolitan region. This example demonstrates that parks, greenspace, and topographic relief associated with AP fault zone regulation and tectonic geomorphology can create enough of a perceived amenity to outweigh the perceived disamenities of TRI sites, industrial complexes, and nearby low income neighborhoods.

It is remarkable that earthquake fault zone regulation can help to create park space, but the potential for the AP Act to continue to add park space within the parks poor Los Angeles region is limited. Much of the city was developed prior to the AP enactment (Fig. 2.5A) and preexisting homes were grandfathered, allowing most homes to remain where they are, even if built directly over fault traces. However, it will be interesting to observe the reconstruction response of these older AP neighborhoods in the instance of an earthquake rupture along a fault such as the Raymond Fault, which was almost completely urbanized prior to the AP act (Figs. 2.1 and 2.5A).

CONTEXTUALIZING THIS STUDY: PERCEPTIONS AND RISK

The result that earthquake hazard regulation has not stigmatized nearby neighborhoods is not completely new. Palm (1981) showed that the AP Act did not significantly affect home prices and she used surveys to show that homebuyers within AP zones in the San Francisco area were generally uneducated about the potential of earthquake hazard, despite the homebuyer disclosure clause within the AP Act. They also showed that buyers' strongest concern was current home value and the potential for appreciation of value. Her results demonstrated that earthquake hazards rarely factor into homebuyers' reasoning. Palm concluded that the negligible impact of this consumer protection legislation was due to poor disclosure protocol. As well, people quickly forget the repercussions of past hazardous events, termed "hazards amnesia." Indeed, the original name of what is now called the AP "Earthquake Fault Zoning" Act was

the AP "Geological Hazards Zones" Act (Hart and Bryant, 1997) a much less descriptive title. In addition to the non-informative title, Palm showed that many real estate agents did not understand the AP Act, mortgage lenders did not take into consideration the implied risk of an AP zone, and disclosure procedure had very little impact on home buyer's perception of risk associated with these faults.

In 1994, the AP Act was given a more precise and descriptive title of "AP Earthquake Fault Zoning". This title leaves little room to hide what the zoning law implies about earthquake hazard. However, despite the name change our investigation of social vulnerability relative to AP zones confirms that earthquake fault zone regulation continues to have no negative impact on the social condition of neighborhoods surrounding active faults. It seems unlikely that the 1990 Seismic Hazard Mapping Act (California Geological Survey, 2008), recent probabilistic seismic hazards analyses, or news reports explaining imminent seismic risk (Chong and Becerra, 2005; Field et al., 2008; and Becerra, 2008) will change people's perceptions about neighborhoods with greater earthquake shaking hazard. Indeed, we find that census block groups within zones of significant shaking hazard are less socially vulnerable than the overall metropolitan region (Table 2.3 and Fig. 2.4A). This suggests that perceived risk of earthquake hazard is outweighed by the perceived amenities of living in areas with greater greenspace, further from the central city, and away from TRI sites.

While this analysis shows that the socially vulnerable are unlikely to live within zones of greatest primary earthquake hazard, this spatial relationship is unlikely to protect such groups from loss in the event of a large earthquake. The

largest earthquakes will radiate significant seismic energy across the Los Angeles basin (Fig. 2.3A). The socially vulnerable live in dense urban areas with older housing. Many of these homes were built prior to the development of rigorous earthquake construction codes. Additionally the socially vulnerable are more dependent on social services, which will certainly be interrupted in future large earthquakes. Thus, the socially vulnerable are at greatest risk of experiencing building and infrastructure failure, which are the primary sources of earthquake deaths and injury, and they will face difficulty meeting basic needs during the recovery process, as social services are interrupted following future earthquakes (Bolin with Stanford, 1998). Moreover, there is a strong spatial link between the socially vulnerable and industrial TRI facilities (Table 2.3 and Fig. 2.4). Failure of these toxic releasing facilities during future earthquakes would directly impact socially vulnerable populations in potentially very dangerous ways.

CONCLUSIONS

Building upon established methods for examining social vulnerability using census data, we developed a spatially-explicit normalized social vulnerability index at the Census block group scale for metropolitan Los Angeles. Comparing the spatial distributions of vulnerability, seismic hazard, Alquist-Priolo Act fault zone regulation, and the amenities of greenspace and parks has revealed several important relationships. Foremost among these is the observation that people with access to financial and political resources, those with low social

vulnerability, strive to live in neighborhoods with parks, even in the face of forewarned risk from natural hazards.

This research was motivated by the idea that regulation of earthquake hazards through the Alquist-Priolo Act may have stigmatized neighborhoods nearest to these fault zones. If these areas became stigmatized, we would expect these zones to be avoided by privileged groups and occupied by socially vulnerable populations. Our analyses lead us to reject this hypothesis. Instead, we find that the AP regulation has led developers to construct additional park space adjacent to active faults. Parks and greenspace are seen as environmental amenities and neighborhoods along AP earthquake fault zones have among the lowest social vulnerability index values within Los Angeles. Apparently, wealthy populations choose to occupy areas near faults because of their situation away from the central city and TRI sites, and because these neighborhoods enjoy greater park access and vegetation cover. One of the most important observations from this study is that in Los Angeles the distribution of social vulnerability is more strongly tied to a lack of the amenity of parks and greenspace than to environmental hazards.

These findings corroborate existing studies on the distributional justice of environmental amenities and disamenities in Los Angeles, where ethnic and racial minorities live in neighborhoods with less open space and closer to a greater proportion of toxic facilities than white residents. The unexpected relationship between social status and earthquake hazard highlights the importance of understanding how privilege manifests itself in complex metropolitan

environments. An unintended consequence of the AP Act was to create environmental amenities enjoyed primarily by privileged residents. The effort to mitigate earthquake hazards thus, in surprising ways, may help reinforce existing environmental injustices related to the distribution of park space and TRI sites that are anti-correlated with greenspace.

ACKNOWLEDGEMENTS

We thank Jerry Treiman and the California Department of Conservation for helpful communication about the Alquist-Priolo Act and participants from Arizona State University's fall 2009 workshop about the environmental justice of cities for many important discussions which helped improve this research. The National Science Foundation Graduate Education and Research Traineeship (IGERT) in Urban Ecology grant DGE 0504248 supported N. Toké as he developed this research.

REFERENCES CITED

Akciz, S.O., Grant-Ludwig, L., Arrowsmith, J R., and Zielke, O., 2010, Century-long average time intervals between earthquake ruptures of the San Andreas fault in the Carrizo Plain, California: Geology, v. 38, no. 9, p. 787-790, doi:10.1130/G30995.1.

Allen, T.I., Wald, D.J., Hotovex, A.J., Lin, K., Earle, P.S., and Marano, K.D., 2008, An Atlas of ShakeMaps for Selected Global Earthquakes: US Geological Survey Open-File Report 2008-1236, 34 p., http://pubs.usgs.gov/of/2008/1236/.

Arrowsmith, J R., Rhodes, D.D., and Pollard, D.D., 1998, Morphologic dating of scarps formed by repeated slip events along the San Andreas Fault, Carrizo Plain, California: Journal of Geophysical Research, v. 103, no. B5, p. 10,141-10,160.

Bedimo-Rung, A.L., Mowen, A.J., and Cohen, D.A., 2005, The significance of parks to physical activity and public health, A conceptual model: American Journal of Preventive Medicine, v. 28, no. 2, p. 15-168.

Becerra, H., 2008, Likelier here: the next Big One; Fault-laced Southern California has a greater chance of a huge quake by 2038 than the North, researchers say: Los Angeles Times, April 15th.

Behr, W.M., Rood, D.H., Fletcher, K.E., Guzman, N., Finkel, R., Hanks, T.C., Hudnut, K.W., Kendrick, K.J., Platt, J.P., Sharp, W.D., Weldon, R.J., and Yule, J.D., 2010, Uncertainties in slip-rate estimates for the Mission Creek strand of the southern San Andreas fault at Biskra Palms Oasis: GSA Bulletin, v. 122, no. 9-10, p.1360-1377, doi: 10.1130/B30020.1.

Bilham, R., 2009, The seismic future of cities: Bulletin of Earthquake Engineering, v. 7, p. 839-887, doi: 10.1007/s10518-00909147-0.

Bolin, B. with Stanford, L., 1998. The Northridge Earthquake Vulnerability and disaster: New York, Routledge, 272 p.

Bolin B., Grineski, S. and Collins, T., 2005, The Geography of Despair: Environmental Racism and the Making of South Phoenix, Arizona USA: Research in Human Ecology, v. 12, no.2, p. 157-168.

Boone, C.G. and Modarres, A., 1999, Creating a Toxic Neighborhood in Los Angeles County: A Historical Examination of Environmental Inequity: Urban Affairs Review, v. 35, p. 163-187.

Boone, C.G., 2008, Environmental Justice as a Process and New Avenues for Research: Environmental Justice, v. 1, no.3, p. 149-154.

Boone, C.G., Buckley, G.L., Grove, J.M., and Sister, C., 2009, Parks and People: An Environmental Justice Inquiry in Baltimore, Maryland: Annals of the Association of American Geographers, v. 99, no. 4, p. 1-21.

Brulle, R.J. and Pellow, D.N., 2006, Environmental Justice: Human Health and Environmental Inequities: Annual Reviews of Public Health, v. 27, p. 103-124.

California Geological Survey, 2001, GIS Files of Official Alquist-Priolo Earthquake Fault zones (CD 2001-05 – Southern Region) and Fault Rupture Zones in California: Special Publication 42.

California Geological Survey, 2008, Guidelines for Evaluating and Mitigating Seismic Hazards in California: California Geological Survey, Special Publication 117a, 98 p. http://www.consrv.ca.gov/cgs/shzp/webdocs/sp117.pdf.

Chong, J. and Becerra, H., 2005, California Earthquake could be the Next Katrina: Los Angeles Times, September 10th.

Cannon, S.H, Gartner, J.E., Wilson, R.C., Bowers, J.C., and Laber, J.L., 2007, Storm rainfall conditions for floods and debris flows from recently burned areas in southwestern Colorado and California: Geomorphology, v. 96, p. 250-269.

Cutter, S.L., 1996, Vulnerability to environmental hazards: Progress in Human Geography, v. 20, p. 529-539.

Cutter, S. L., Boruff, B. J., and Shirley, W. L., 2003, Social vulnerability to environmental hazards: Social Science Quarterly, v. 84, no.2, p. 242-61.

Cutts, B.B., Darby, K.J., Boone, C.G., and Brewis, A., 2009, City Structure, obesity, and environmental justice: An integrated analysis of physical and social barriers to walkable streets and park access: Social Science and Medicine, v. 69, p. 1314-1322.

Dolan, J.F., Sieh, K., Rockwell, T.K., Yeats, R.S., Suppe, J., Huftile, G.J., and Gath, E.M., 1995, Prospects for Larger or More Frequent Earthquakes in the Los Angeles Metropolitan Region: Science, v. 267, p. 199-205.

Dolan, J.F., Sieh, K., and Rockwell, T.K., 2000, Late Quaternary activity and seismic potential of the Santa Monica fault system, Los Angeles, California: GSA Bulletin, v. 112, p. 1559-1581.

Field, E.H., Dawson, T.E., Felzer, K.R., Frankel, A.D., Gupta, V., Jordan, T.H., Parsons, T., Petersen, M.D., Stein, R.S., Weldon II, R.J., and Wills, C.J., 2008, Uniform California Earthquake Rupture Forecast, Version 2 (UCERF 2): US Geological Survey Open-File Report 2007-1437, 104 p., http://pubs.usgs.gov/of/2007/1437/.

Hart, E.W. and Bryant, W.A., 1997, FAULT RUPTURE HAZARDS IN CALIFORNIA Alquist-Priolo Earthquake Fault Zoning Act with Index to Earthquake Fault Zone Maps: Department of Conservation, Division of Mines and Geology, Special Publication 42.

Harvey, D., The Environment of Justice, in A. Merrifield and E. Swyngedouw, editors, 1997, The Urbanization of Injustice: New York, NYU Press, p. 65-99.

Jackson, J., 2006, Fatal attraction: living with earthquakes, the growth of villages into megacities, and earthquake vulnerability in the modern world: Philosophical transactions of the Royal Society A, v. 364, p. 1911-1925, doi: 10.1098/rsta/2006/1805.

Kolbe A., Hutson, R., Shannon, H., Trzcinski, E., Miles, B., Levitz, N., Puccio, M., James, L., Noel, J.R., and Muggah, R., 2010, Mortality, crime and access to basic needs before and after the Haiti earthquake: a random survey of Port-au-Prince households: Medicine, Conflict, and Survival, v. 26, no. 4, p. 281-297.

Lawson, A.C., 1908, The California Earthquake of April 18, 1906: Report of the State Earthquake Investigation Commission: Washington D.C., Carnegie Institution of Washington.

Machette, M.N., Personius, S.F., Nelson, A.R., Schwartz, D. P., and Lund, W.R., 1991, The Wasatch fault zone, Utah – segmentation and history of Holocene earthquakes: Journal of Structural Geology, v. 13, no.2, p. 137-149.

Modarres, A, 1998, Putting Los Angeles in its place: Cities, v. 15, p. 135-147, doi: 10.1016/S0264-2751(98)00013-4.

Mulvey, J.M., Awan, S.U., Qadri, A.A., and Maqsood, M.A., 2008, Profile of injuries arising from the 2005 Kashmir Earthquake: The first 72 h: Injury, v. 39, no. 5, p. 554-560.

U.S. National Library of Medicine, 2009, EPA's Toxic Release Inventory from TOXMAP: Environmental Health e-Maps. Last accessed January 2011, http://toxmap.nlm.nih.gov/toxmap/main/index.jsp.

Palm, R.I., 1981, Public Response to Earthquake Fault Information: Annals of the Association of American Geographers, v. 71, no. 3, p. 389-399.

Petersen, M.D., Frankel, A.D., Harmsen, S.C., Mueller, C.S., Haller, K.M., Wheeler, R.L., Wesson, R.L., Zeng, Y., Boyd, O.S., Perkins, D.M., Luco, N., Field, E.H., Wills, C.J., and Rukstales, K.S., 2008, Documentation for the 2008 Update of the United States Seismic Hazard Maps: United States Geological Survey Open File Report: 2008-1128, 60 p., http://pubs.usgs.gov/of/2008/1128/

Proctor, R.J., Crook Jr., R., Mckeown, M.H., and Moresco, R.L., 1972, Relation of Known Faults to Surface Ruptures, 1971 San Fernando Earthquake, Southern California: GSA Bulletin, v. 83, no. 6, p. 1601-1618.

Pulido, L., 2000, Rethinking Environmental Racism: White Privilege and Urban Development in Southern California: Annals of the Association of American Geographers, v. 90, no.1, p. 12-40.

Rashed, T. and Weeks, J., 2003, Assessing vulnerability to earthquake hazards through spatial multicriteria analysis of urban areas: International Journal of Geographical Information Science, v. 17, no. 6, p. 549-576, doi: 10.1080/1365881031000114071.

Reid, H.F., 1910, The Mechanics of the Earthquake, The California Earthquake of April 18, 1906: Report of the State Investigation Commission, v.2: Washington, D.C., Carnegie Institution of Washington.

Reitherman R.K. and Leeds, D.J., 1991, A Study of the Effectiveness of the Alquist-Priolo Program: California Division of Mines and Geology Open File Report 90-18, 131p.

San Bernardino County Assessor's Office, 2010, Parcel Basemap Data, County of San Bernardino GIS, Last Accessed January, 2011: http://gis.sbcounty.gov/customscript/RequestFTPAccount.aspx.

Scharer, K.M., Biasi, G.P., Weldon II, R.J., and Fumal, T.E., 2010, Quasi-periodic recurrence of large earthquakes on the southern San Andreas fault: Geology, v. 38, no. 6, p. 555-558, doi: 10.1130/G30746.1.

Sister, C., Wolch, J., and Wilson, J., 2009, Got Green? Addressing environmental justice in park provision: GeoJournal, v/ 75, no. 3, p. 229-248, doi: 10.1007/s10708-009-9303-8.

Schlosberg, D., 2007, Defining Environmental Justice: New York: Oxford.

Toké, N.A., Arrowsmith, J R., Rymer, M.J., Landgraf, A., Haddad, D.E., Busch, M., Coyan, J., and Hannah, A., 2011, Late Holocene slip rate of the San Andreas fault and its accommodation by creep and moderate magnitude earthquakes at Parkfield, California: Geology, v. 39, no. 3, p. 243-246, doi: 10.1130/G31498.1.

Trifunac, M.D., 1976, Preliminary Analysis of the Peaks of Strong Earthquake Ground Motion – Dependence of Peaks on Earthquake Magnitude, Epicentral Distance, and Recording Site conditions: Bulletin of the Seismological Society of America, v. 66, no. 1, p. 189-219.

Tucker, C.J., 1979, Red and photographic infrared linear combinations for monitoring vegetation: Remote Sensing of the Environment, v. 8, p. 127-150.

Turner II, B.L., Kasperson, R.E., Matson, P.A., McCarthy, J., Corell, R.W., Christensen, L., Eckley, N., Kasperson, J.X., Luers, A., Martello, M.L., Polsky, C., Pusipher, A., and Schiller, A., 2003, A framework for vulnerability analysis in sustainability science: Proceedings of the National Academy of Sciences, v. 100, no. 14, p. 8074-8079.

United Church of Christ Commission for Racial Justice, 1987, Toxic wastes and race in the United States: A national report on the racial and socio-economic characteristics of communities with hazardous waste sites: New York: Public Data Access, Inquiries to the Commission.

U.S. Census Bureau, 2000, American FactFinder, Last Accessed February 2011, http://factfinder.census.gov.

U.S. Geological Survey, 1971, Surface Faulting: The San Fernando California, Earthquake February 9, 1971: U.S. Geological Survey Professional Paper 733, p. 55-76.

U.S. Geological Survey, 2006, Quaternary fault and fold database for the United States, Last accessed October 2010: http//earthquakes.usgs.gov/hazards/qfaults/.

U.S. Geological Survey, 2008, Earthquake Hazards Program Interactive Hazard Maps, Last Accessed April, 2011: http://earthquake.usgs.gov/hazards/apps/gis/.

Wald, D.J., Quitoriano, V., Heaton, T.H., and Kanamori, H., 1999, Relationships between Peak Ground Acceleration, Peak Ground Velocity, and Modified Mercalli Intensity in California: Earthquake Spectra, v.15, p. 557-564, doi:10.1193/1.1586058

Wallace, R.E., editor, 1990, The San Andreas Fault System, California: United States Geological Survey Professional Paper 1515, 283 p.

Wells, D. L., and Coppersmith, K. J., 1994, New empirical relationships among magnitude, rupture length, rupture width, rupture area, and surface displacement: Bulletin of the Seismological Society of America, v. 84, no. 4, p. 974–1002.

Westerling, A.L., Cayan, D.R., Brown, T.J., Hall, B.L., and Riddle, L.G., 2004, Climate, Santa Ana Winds and Autumn Wildfires in Southern California: EOS, v. 85, no. 31.

Wilson, S., Hutson, M., and Mujahid, M., 2008, How Planning and Zoning Contribute to Inequitable Development, Neighborhood Health and Environmental Justice: Environmental Justice, v. 1, no. 4, p. 211-216.

Wolch, J., Wilson, J.P., and Fehrenbach, J., 2005, Parks and Park Funding in Los Angeles: An Equity Mapping Analysis: Urban Geography, v. 26, no. 1, p. 4-35.

Wood, H.O. and Neumann, F., 1931, Modified Mercalli Intensity Scale of 1931: Bulletin of the Seismological Society of America, v. 21, no. 4, p. 277-283.

Wood, N.J., Burton, C.G., and Cutter, S.L., 2010, Community variations in social vulnerability to Cascadia-related tsunamis in the Pacific Northwest: Natural Hazards, v. 52, no. 2, p. 369-389, doi: 10.1007/s11069-009-9376-1.

Zielke, O., Arrowsmith, J R., Grant-Ludwig, L., and Akciz, S.O., 2010, Slip in the 1857 and Earlier Earthquakes along the Carrizo Plain, San Andreas Fault: Science, v. 327, no. 1119-1122, doi: 10.1126/science.1182781.

TABLE 2.1. RECENT LARGE EARTHQUAKES:
CASUALTY RATES AND GDP

Earthquake and Magnitude[1]	Population Exposed to MMI > VIII[2]	Casualties (approx.)[3]	Casualty Rate[4]	2010 Per Capita GDP[5]
1.12.2010 Haiti Earthquake Magnitude 7.0	3.1 million	222,500	7%	$1,200
2.27.2010 Chilean Earthquake Magnitude 8.8	3.6 million	600	0.02%	$15,400
2.21.2011 Christchurch, NZ Magnitude 6.1	0.3 million	300	0.1%	$27,700
3.11.2011 Japan Earthquake Magnitude 9.0	5.8 million	28,000	0.5%[6]	$34,000

1 – Data obtained from the US Geological Survey's 2011 and 2010 significant earthquake websites. http://earthquake.usgs.gov/earthquakes/eqinthenews/2010/
2 – Data from USGS PAGER impact reports http://earthquake.usgs.gov/earthquakes/pager/
3 – Numbers were obtained from US Geological Survey earthquake pages.
4 – Percent of the population exposed to Modified Mercalli Intensities greater than VIII that died.
5 – Gross domestic product numbers were obtained from the CIA world factbook website: https://www.cia.gov/library/publications/the-world-factbook/index.html
6 – The majority of the Japan Earthquake casualties were due to tsunami.

TABLE 2.2. THE 20 CENSUS BLOCK GROUP FACTORS CONSIDERED IN THE LOS ANGELES SOCIAL VULNERABILITY INDEX (LA-SoVI)

Categories of Social Condition	Factors (census metrics) of the social vulnerability index (LA-SoVI)	
Personal Wealth	Percent of households' income above $75K/year (access to resources and political power)	Factor sign = NEGATIVE[1]
	Per Capita Income in 1999 (access to resources and political power)	Factor sign = NEGATIVE
	Percent of people below poverty level (lack of access to resources and political power)	Factor sign = POSITIVE
Age and Dependency	Percent of population below 18 or above 65 (physical limitations of individuals)	Factor sign = POSITIVE
	Percent single parent households (access to resources and social capital)	Factor sign = POSITIVE
	Percent single person households over age 65 (lower social capital and physical limitations of individuals)	Factor sign = POSITIVE
Density of the Built Environment	Housing Units per square mile	Factor sign = POSITIVE
	Average Household Size	Factor sign = POSITIVE
Housing Stock and Tenancy	Percent of housing built before 1970 (earthquake regulation began during the 1970s)	Factor sign = POSITIVE
	Percent of housing units that are vacant (economic condition and social capital)	Factor sign = POSITIVE
	Percent of housing units that are renter occupied (access to resources and social capital)	Factor sign = POSITIVE
Under-represented groups	Percent minorities (non-whites) (political power and representation)	Factor sign = POSITIVE
	Percent female (political power and representation)	Factor sign = POSITIVE
	Percent recent immigrants (political power and representation and social capital)	Factor sign = POSITIVE
Local Economy	Percent of the population that is working (access to resources and economic condition)	Factor sign = NEGATIVE
	Percent of population with a disability (physical limitations)	Factor sign = POSITIVE
	Percent of the population with Social Security Income (access to resources and physical limitations)	Factor sign = POSITIVE
Infrastructure dependence	Percent of workers with a long commute (access to resources, social capital)	Factor Sign = POSITIVE
	Percent of households with public assistance (access to resources)	Factor Sign = POSITIVE
	Population per square mile (social capital and density of the built environment)	Factor sign = POSITIVE

1- Factors are negative if higher values indicate a better social condition and therefore lower social vulnerability

TABLE 2.3.

MEAN BLOCK GROUP SOCIAL VULNERABILITY, GREENSPACE, AND THE SEVEN INDEX CATEGORIES

MAKING UP THE LA-SoVI FOR DIFFERENT UNITS OF SPATIAL ANALYSIS

Spatial Unit (CBG count[1])	LA-SoVI[2]	Green space (NDVI)[3]	Personal Wealth	Age and Dependence	Housing and Tenancy	Density of Built Env.	Under-represented groups	Local Economy	Infra-structure dependence
Los Angeles Metro (9433)	-0.11[4] 1.3 (std. dev.)	-0.169 0.08	0.30 1.0	0.0038 0.6	-0.030 0.8	-0.31 0.7	0.045 0.7	-0.080 0.7	0.017 0.7
High Shaking Hazard Areas[5] (1901)	-0.28 1.3	-0.140 0.07	0.31 0.9	0.074 0.6	-0.17 0.8	-0.53 0.6	-0.070 0.6	-0.027 0.7	-0.22 0.6
AP Act zones (443)	-0.55 1.3	-0.138 0.08	-0.02 1.0	-0.014 0.6	-0.34 0.8	-0.65 0.5	-0.11 0.7	-0.094 0.8	-0.26 0.6
< 1km of non-AP active faults[6] (1333)	-0.67 1.2	-0.150 0.09	-0.16 1.0	-0.18 0.6	-0.058 0.7	-0.58 0.6	-0.24 0.6	-0.26 0.7	-0.26 0.6
< 1km of TRI site (1866)	0.38 1.2	-0.199 0.06	0.69 0.8	0.13 0.5	0.066 0.7	-0.076 0.7	0.25 0.6	0.082 0.7	0.059 0.7
Very High Vulnerability (1423)	2	-0.225 0.05	1.6 0.3	0.68 0.4	0.86 0.5	0.59 0.6	0.84 0.4	0.52 0.5	1.0 0.6
Very Low Vulnerability (1923)	-2	-0.115 0.08	-0.97 0.5	-0.55 0.4	-0.82 0.7	-0.88 0.3	-0.68 0.4	-0.80 0.5	-0.50 0.4

1 - Census block groups in spatial unit of analysis
2 - Los Angeles relative social vulnerability index – see text for description.
3 - Normalized difference vegetation index, calculated using Landsat scenes from spring 2000. NDVI = (NIR-Red)/(Red+NIR)
4 - LA-SoVI is calculated using natural breaks, despite being a normalized index, the average of all CBGs within the region is slightly less than zero.
5 - CBGs with a > 10% chance of exceeding peak ground accelerations > 60 % gravity in the next 50 years according to probabilistic seismic hazards analysis
6 - CBGs within 1km of an active fault that is not zoned as an AP earthquake fault zone (Figure 2.1).

Figure 2.1. The Los Angeles (LA) metropolitan region (including the counties of Los Angeles, Orange, Ventura, San Bernardino, and Riverside) is located between the Pacific Ocean and a group of tectonically active mountain ranges in southern California, USA. Census block groups (U.S. Census Bureau, 2000) of the LA region cross numerous active faults (U.S. Geological Survey, 2006) associated with the San Andreas plate boundary. The most active faults are the San Andreas and San Jacinto. Census block groups that cross Alquist-Priolo (AP) Act earthquake zones (California Geological Survey, 2001) are associated with the following faults: CF = Chino Fault, CFZ = Cucamonga Fault Zone, EF = Elsinore Fault, MCF = Malibu Coast Fault, NIF = Newport-Inglewood Fault, RF = Raymond Fault, San Andreas Fault, San Jacinto Fault, SMF = Sierra Madre Fault, SRF = Santa Rosa Fault, and the WF = Whittier Fault. Other faults that are considered active by the earthquake science community, but not zoned by the AP act because evidence of Holocene surface rupture has not been discovered include the following: BF = Bailey Fault, HF = Hollywood fault, ORF = Oak Ridge Fault, PVF = Palos Verdes Fault, SJF = San Jose Fault, SGF =San Gabriel Fault, SMF = Santa Monica Fault, and the VF = Verdugo Fault. Several AP zones along the San Andreas, San Jacinto, and Newport Inglewood faults are associated with constructed parks and open space (yellow boxes and Figs. 2.5-2.6).

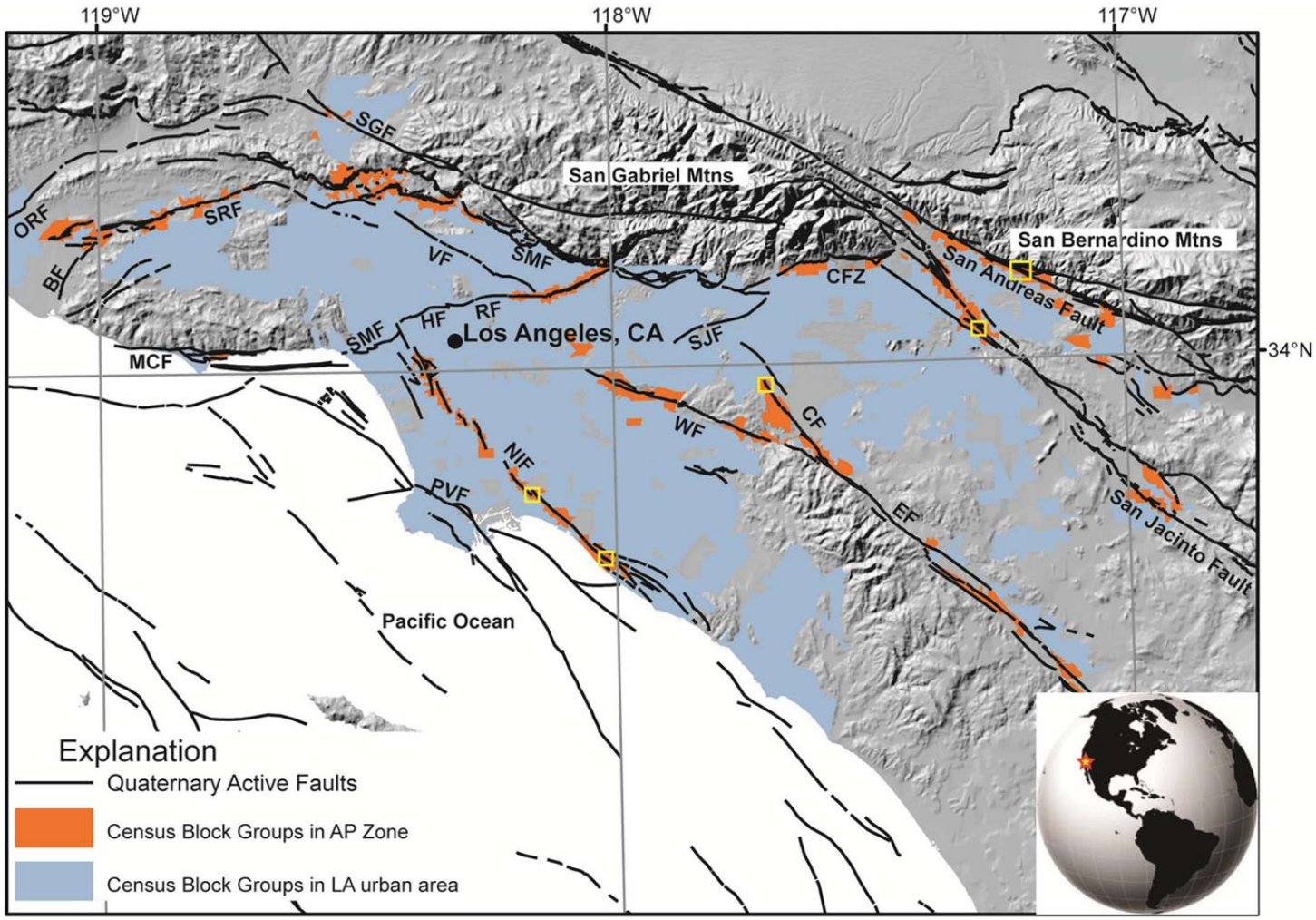
119°W
118°W
117°W
34°N
SGF
ORF
SRF
BF
VF
SMF
San Gabriel Mtns
San Bernardino Mtns
CFZ
San Andreas Fault
HF
RF
Los Angeles, CA
SJF
SMF
MCF
WF
CF
NIF
PVF
EF
San Jacinto Fault
Pacific Ocean
Explanation
Quaternary Active Faults
Census Block Groups in AP Zone
Census Block Groups in LA urban area

Figure 2.2. U.S. Census block group size is variable (U.S. Census Bureau, 2000). However, in the Los Angeles metropolitan region and along active faults such as the San Andreas and San Jacinto faults the size of census block groups is comparable to the width of Alquist-Priolo (AP) earthquake fault zones. Also note that AP zones span widths that are greater than the distribution of surface fault traces within a given fault zone. Houses may be built within AP zones, but must be set back from fault traces (California Geological Survey, 2001).

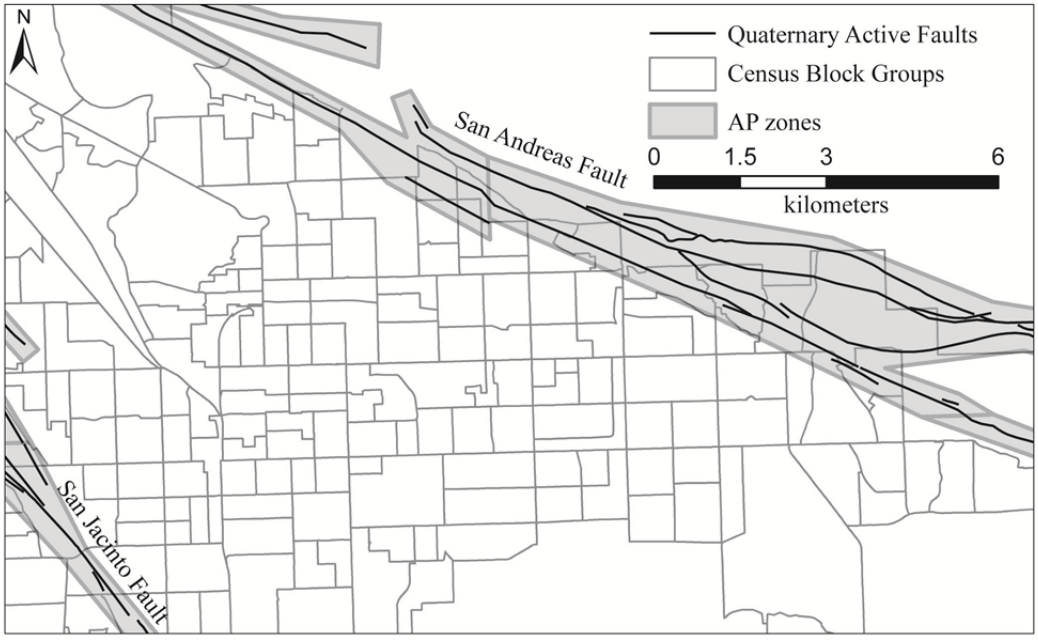

Figure 2.3. Earthquake hazard and social indicator maps for the seven components of the LA-SoVI (Fig. 2.4A and Tables 2.2-2.3). A) Earthquake hazards for Los Angeles. Ground shaking hazard (US Geological Survey, 2008) is shown with contours of peak ground acceleration (PGA), expressed in percent of gravity (%G), with a 10% probability of occurrence in the next 50 years. Surface rupture hazard is depicted by the location of Alquist-Priolo (AP) Act earthquake fault zones (black polygons) and non-AP zone active faults (grey lines). For each of the seven social indicator maps contributing to up the social vulnerability calculation (LA-SoVI) AP zones and areas with the extreme ground shaking hazard are shown (PGA > 60% of gravity = areas of grey shading). The seven indicator categories include: B) Condition of the local economy and workforce, C) Proportion of underrepresented groups, D) Housing age and tenancy, E) Age or residents, dependency on others and social safety nets, F) Personal wealth and poverty, G) Infrastructure dependence, H) Density of the built environment. The values shown here are qualitative descriptors. Neutral values indicate census block groups with values within 0.5 standard deviations from the mean for all of Los Angeles (Table 2.3). Each additional category corresponds to another standard deviation from the mean. For additional descriptions about these indicators see Table 2.2 and for expanded figures for each panel see Appendix A.

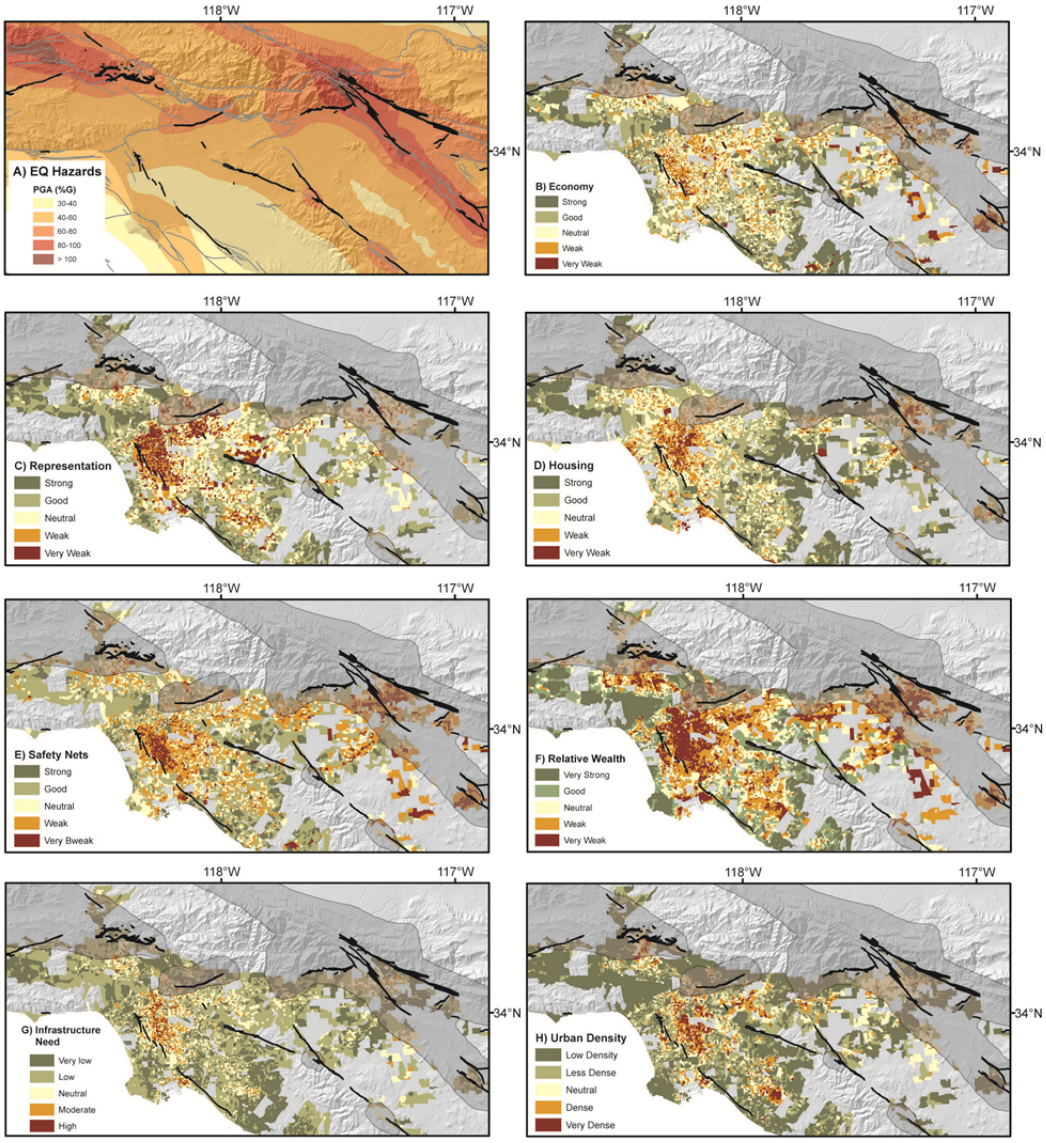
118°W
117°W
34°N
A) EQ Hazards
PGA (%G)
30-40
40-60
60-80
80-100
> 100
B) Economy
Strong
Good
Neutral
Weak
Very Weak
C) Representation
Strong
Good
Neutral
Weak
Very Weak
D) Housing
Strong
Good
Neutral
Weak
Very Weak
E) Safety Nets
Strong
Good
Neutral
Weak
Very Bweak
F) Relative Wealth
Very Strong
Good
Neutral
Weak
Very Weak
G) Infrastructure Need
Very low
Low
Neutral
Moderate
High
H) Urban Density
Low Density
Less Dense
Neutral
Dense
Very Dense

Figure 2.4. A) Relative social vulnerability index (LA-SoVI) and earthquake hazard in Los Angeles, California. The social vulnerability index is a combination of seven indices describing the social condition at the census block group scale (Tables 2.2-2.3 and Fig. 2.3). Negative LA-SoVI values represent census block groups with low social vulnerability and positive values are those with high vulnerability. Socially vulnerability is spatially anti-correlated with Alquist-Priolo earthquake fault zones. The cities of downtown Los Angeles (LA), Long Beach (LB), Van Nuys (VN), Pomona (P), Ontario (O), and San Bernardino (SB) are marked for reference. B) The location and relative annual emissions from toxic release inventory facilities (TRI: U.S. National Library of Medicine, 2009) monitored by the U.S. Environmental Protection Agency and a Landsat-based normalized difference vegetation index (NDVI: e.g., Tucker, 1979) representing relative greenness for the urban area. The NDVI was converted to census block group scale by averaging the overlapping 30 m Landsat pixels. It is expressed here as standard deviations above and below the NDVI mean for the entire urban area.

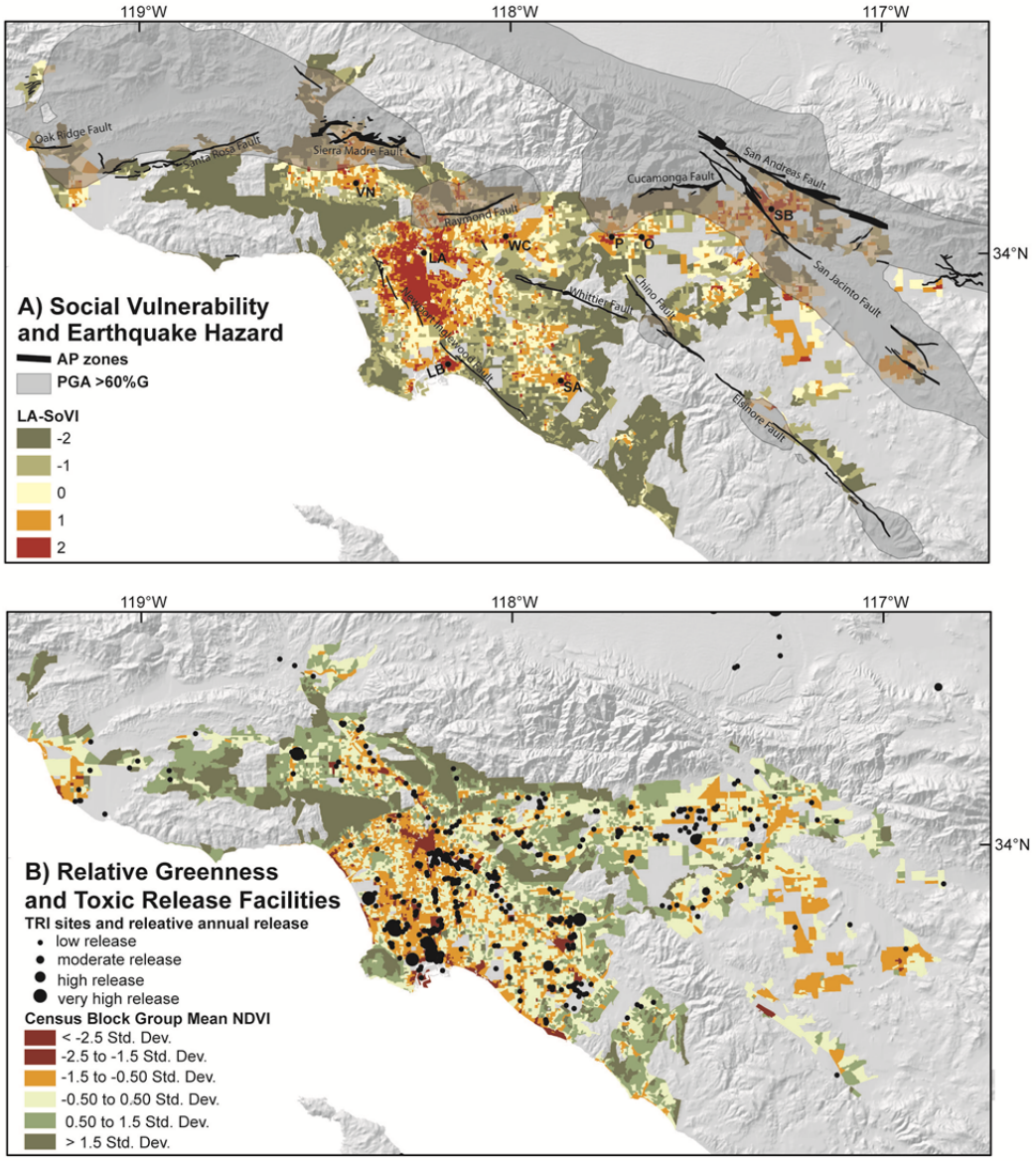
119°W
118°W
117°W
34°N
Oak Ridge Fault
Santa Rosa Fault
Sierra Madre Fault
VN
Raymond Fault
WC
LA
Cucamonga Fault
San Andreas Fault
SB
P
O
San Jacinto Fault
Whittier Fault
Chino Fault
Newport-Inglewood Fault
LB
SA
Elsinore Fault
A) Social Vulnerability
and Earthquake Hazard
AP zones
PGA >60%G
LA-SoVI
-2
-1
0
1
2

119°W
118°W
117°W
34°N
B) Relative Greenness
and Toxic Release Facilities
TRI sites and releative annual release
low release
moderate release
high release
very high release
Census Block Group Mean NDVI
< -2.5 Std. Dev.
-2.5 to -1.5 Std. Dev.
-1.5 to -0.50 Std. Dev.
-0.50 to 0.50 Std. Dev.
0.50 to 1.5 Std. Dev.
> 1.5 Std. Dev.

Figure 2.5. A) The percentage of homes built before 1970 (a decade in which significant earthquake hazards regulations and building codes were adopted) and the location of AP earthquake fault zones. Many census block groups were completely developed prior to the 1972 AP act that regulates building near areas susceptible to fault surface rupture. Where development occurred after the AP's enactment some developers chose to build parks within the fault zone where regulations stipulated they could not construct buildings for occupancy. The locations of 5 such parks are shown here with labeling corresponding to their figure number. B) Along the Chino Fault AP zone a golf course was aligned with the AP zone thereby avoiding having to cite homes within this zone (33°58'03.29" N, 117°42'08.73" W). C) Along the Newport-Inglewood Fault AP zone in Long Beach, CA a left step in the right lateral fault has resulted in uplift of the land surface, forming a hill. Here the hill is covered by view homes and a park called "Hilltop Park" (33°47'57.53" N, 118°09'56.00" W). Juxtaposed against this relatively nice development is an industrial zone (right side of image). It should be noted that other tectonically-produced hills associated with step overs on the Newport-Inglewood fault have been developed for oil and gas extraction. D) In Newport, CA the same AP fault zone was utilized for construction of a linear park following the surface trace of the fault (33°41'02.03" N, 118°00'34.59" W). This Park also contains a community center and pool.

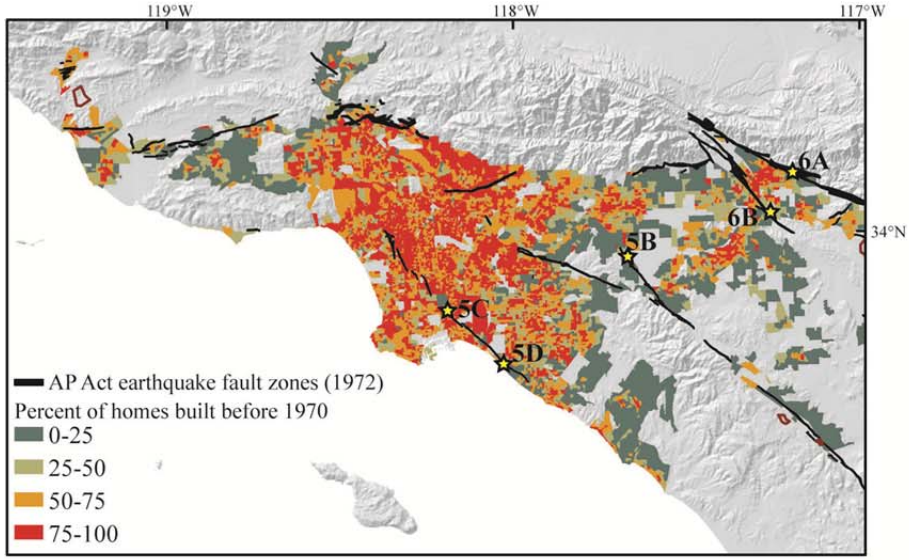

A) Age of housing and fault zone parks

B) Golf course along the Chino Fault

C) Hilltop Development on Newport-Inglewood Fault

D) Park space along the Newport-Inglewood Fault

Figure 2.6. The effects of AP park space on home site parcel value. A) Along the San Andreas Fault AP zone a significant amount of park space was set aside during the development process in Highland, CA (34°07'37.49" N, 117°10'07.46" W). Area-normalized parcel data shows that homes near this fault zone park and within the AP zone itself are the highest valued within the region. This formal park space includes water features, walkways, and irrigated landscaping. Homes nearest to the park are visually impressive with swimming pools and manicured lawns (white box and inset). Along the San Jacinto Fault AP zone (34°03'14.12" N, 117°17'01.56" W) the same relationship between fault zone park space and parcel value is observed. C) Urban development crossed the San Andreas Fault AP earthquake fault zone (yellow lines) after 1995. Aerial photos from 2007 show how homes were built within the AP zone but are set back from the fault trace (red lines) allowing room for park space. D) In addition to formal park space along the San Jacinto Fault AP zone, home lots near the park are also visually greener than surrounding developments. See Fig. 2.5 for mapped locations.

A) Park space and parcel values along the San Andreas Fault AP zone.

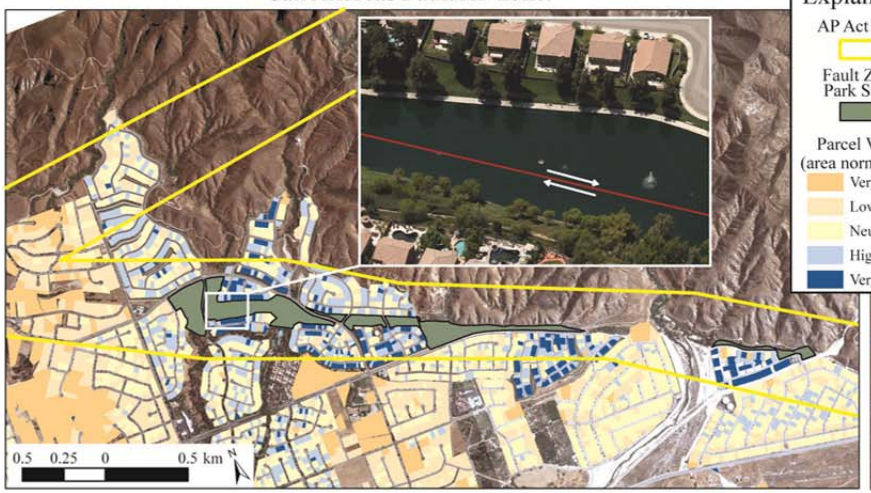

B) Park space and parcel values along the San Jacinto Fault AP zone.

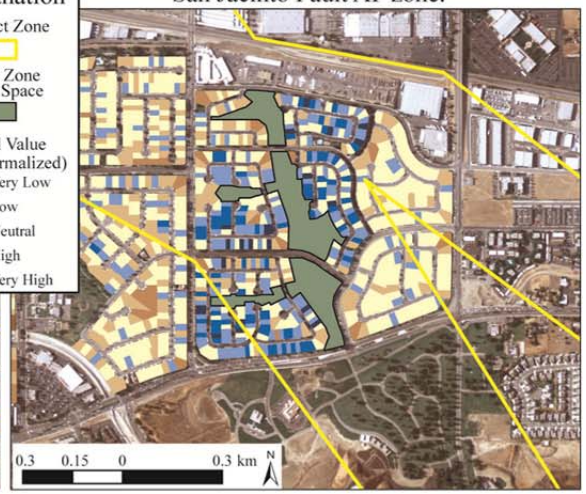

C) Development along the San Andreas Fault AP zone between 1995 and 2007

D) Park space along the San Jacinto Fault AP zone.

Figure 2.7. Average social vulnerability within census block groups binned by NDVI values. Census block groups were binned into groups based upon their relative NDVI values. The mean LA-SoVI values were calculated within these binning ranges and are plotted on the y-axis. Areas with higher than NDVI values (greener) have relatively low vulnerability and areas with more negative NDVI values (less green) have greater LA-SoVI values (more vulnerable).

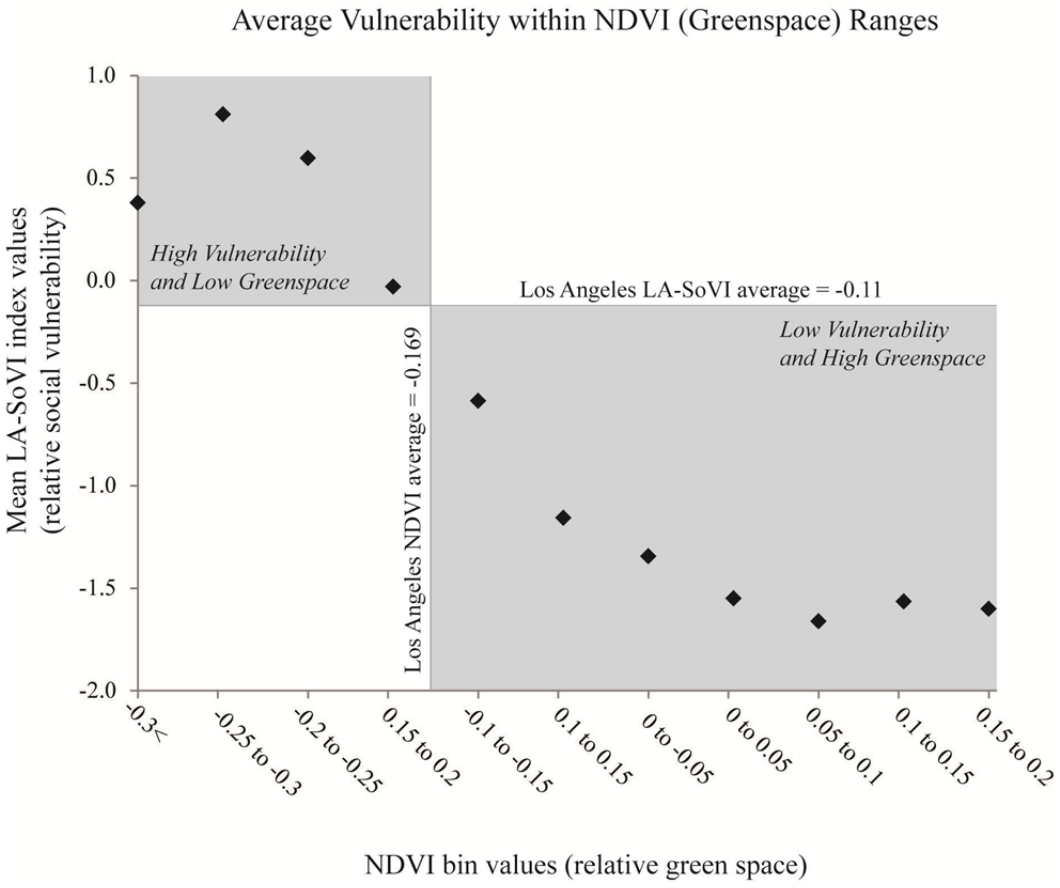

Figure 2.8. Graphs showing A)mean social vulnerability and B) mean greenspace with census block group distance away from Alquist-Priolo (AP) Act earthquake fault zones. Point zero on the x-axes corresponds to all census block groups that contain at least some land regulated as an AP fault zone. The corresponding LA-SoVI and NDVI values represent the average of all of those census block groups. Each additional number on the x-axis represents all of the census block groups that are 1, 2, 3… and up to 15 block groups from an AP zone. Note that position 15 actually includes the very few groups that are 16-18 block groups away from the fault. Some of these far from the fault zone block groups are also located near the coast. Finally, it should be noted that census block groups that are not contiguously linked to an AP zone are not included in this analysis. Average LA-SoVI and NDVI values (grey lines) are plotted in panels A and B. The LA-SoVI standard deviation is 1.3 and the average NDVI standard deviation is 0.08 (Table 2.3). See Fig. 2.4 for related mapping analyses.

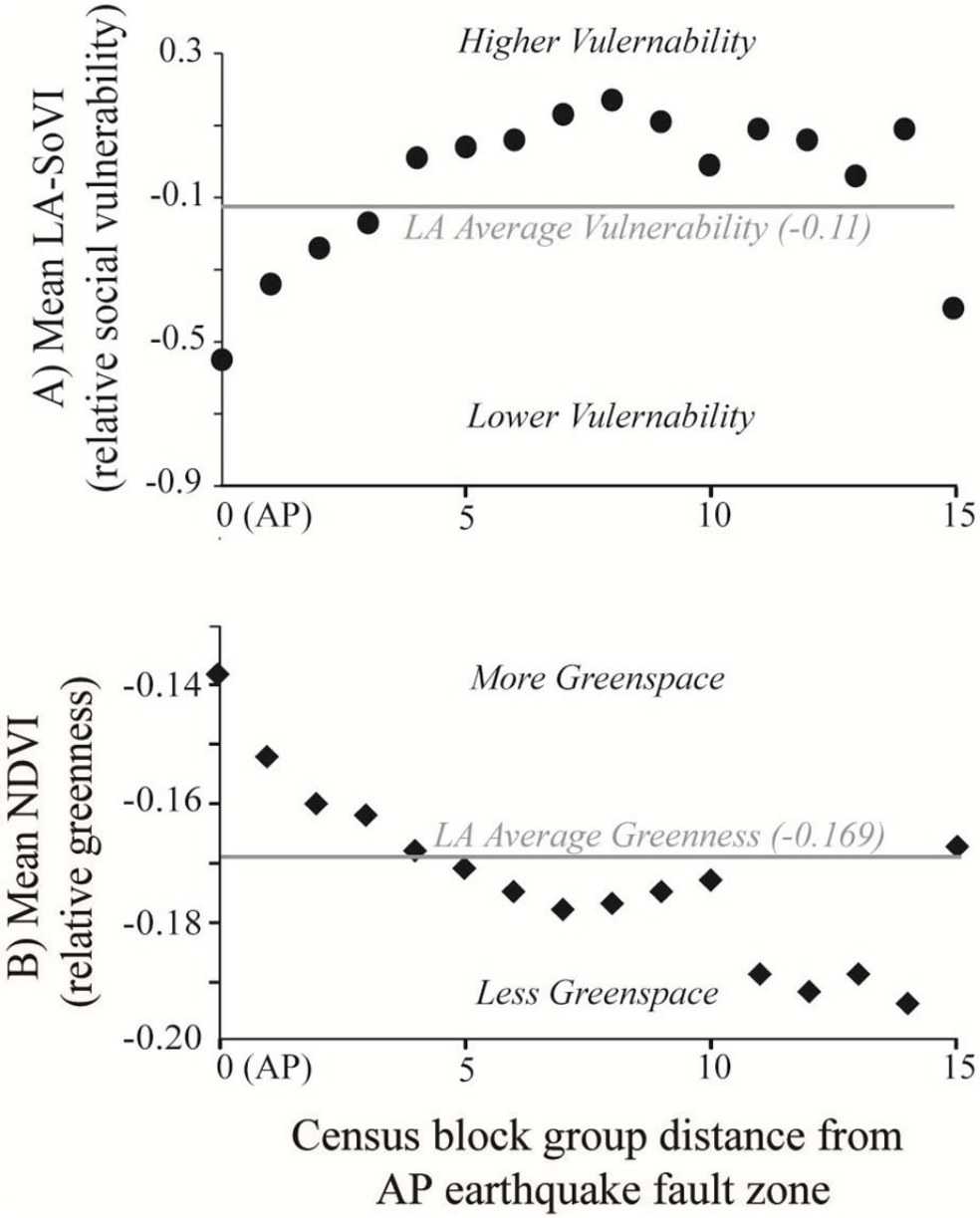
A) Mean LA-SoVI
(relative social vulnerability)
0.3
-0.1
-0.5
-0.9
Higher Vulernability
LA Average Vulnerability (-0.11)
Lower Vulernability
0 (AP)
5
10
15
B) Mean NDVI
(relative greenness)
-0.14
-0.16
-0.18
-0.20
More Greenspace
LA Average Greenness (-0.169)
Less Greenspace
0 (AP)
5
10
15
Census block group distance from
AP earthquake fault zone

CHAPTER 3

LATE HOLOCENE SLIP RATE OF THE SAN ANDREAS FAULT AND ITS ACCOMODATION BY CREEP AND MODERATE-MAGNITUDE EARTHQUAKES AT PARKFIELD, CALIFORNIA

ABSTRACT

Investigation of a right-laterally offset channel at the Miller's Field paleoseismic site yields a late Holocene slip rate of 26.2 +6.4/- 4.3 mm/yr (1 σ) for the main trace of the San Andreas Fault (SAF) at Parkfield. This is the first well documented geologic slip rate between the Carrizo and creeping sections of the SAF. This rate is lower than Holocene measurements on the Carrizo and rates implied by far field geodetic measurements (~35 mm/yr). However, it is consistent with historical slip rates measured to the northwest along the creeping section of the SAF (<30 mm/yr). The paleoseismic exposures at the Miller's Field reveal a pervasive *clay fault strand* deformation fabric extending into the uppermost stratigraphy that is oriented clockwise oblique-to-the-SAF strike. This fabric is consistent with aseismic creep and observations of surface slip from the 2004 M6 Parkfield earthquake. Together, this deformation fabric and slip rate suggest that the historically observed SAF slip behavior along the Parkfield section has persisted for at least a millennium and that significant slip is accommodated by structures in a zone beyond the main SAF trace.

INTRODUCTION

The Parkfield section of the San Andreas Fault (SAF) marks a transition in historically observed slip behavior. To the southeast of Parkfield, the SAF last slipped the M_w 7.9 1857 Fort Tejón earthquake, a ~350 km rupture with mean slip of 5-6 m (Fig. 3.1; e.g., Zielke et al., 2010). Geomorphic evidence for multi-meter slip from the 1857 rupture extends just northwest of CA Highway 46 (e.g., Lienkaemper, 2001). Along the Parkfield section, the SAF creeps aseismically; increasing from ~3 mm/yr near Highway 46 to >25 mm/yr northwest of Middle Mountain (e.g., Lienkaemper and Prescott, 1989; Titus et al., 2006). Additionally, Parkfield has slipped in at least six moderate magnitude earthquakes since 1857 including the 2004 M6 Parkfield earthquake (e.g., Lienkaemper et al., 2006).

Several studies have constructed historical slip budgets since 1857 for the central SAF (e.g., Toké and Arrowsmith, 2006) by balancing creep rates and slip from moderate magnitude earthquakes relative to a ~34 mm/yr slip rate. To the southeast of the Parkfield section, this yields a slip deficit of ~5 m. The deficit decreases along the Parkfield section and is nonexistent on creeping section to the northwest. These slip budget analyses presume a slip rate that is derived from either geologic investigations in the Carrizo Plain (e.g., 33.9 ± 2.9 mm/yr: Sieh and Jahns, 1984) or geodetic measurements spanning wide apertures of the SAF (e.g., 35.9 ± 0.5 mm/yr: Meade and Hager, 2005). However, far-field GPS studies cannot resolve how slip is distributed among the multiple sub-parallel geologic structures comprising the SAF zone such as the southwest fracture zone near Parkfield (SWFZ; Fig. 3.1 and Appendix B). Additionally, there is debate about

whether the current configuration of fault slip behavior along the central SAF is a temporary condition resulting from fault system interactions, that can result in mode switching (Ben Zion et al., 1999), or if the slip behavior is fundamentally controlled by lithology and intrinsic frictional properties of fault zone materials (Moore and Rymer, 2007). Near-surface geologic investigations can help resolve the distribution SAF slip by using offset landforms to estimate slip rates for the main SAF and other sub-parallel structures. Additionally, geology can address the debate about what controls the configuration of slip behavior across fault systems by looking for paleoseismic evidence for a change in the mode of slip release (creep versus rupture).

We present geomorphic and paleoseismic interpretations from the Miller's Field site (Figs. 3.2-3.3) to estimate the late Holocene slip rate of the SAF at Parkfield. This is the only well-documented geologic slip rate in >150 km between the Carrizo (Sieh and Jahns, 1984) and creeping (Perkins et al., 1989) sections of the SAF. We use probability density function analyses (Fig. 3.4) to explore the uncertainty in displacement and age of channel offset and show that the late Holocene slip rate on the SAF at Parkfield is likely lower than Holocene rates from the Carrizo section and far field geodetic estimates. Paleoseismic exposures reveal an absence of evidence for large surface ruptures in the late Holocene and document a pervasive, oblique-to-the-SAF, clay fault strand fabric (Fig. 3.3 and Appendices D-F) that we postulate is produced by creep and moderate magnitude earthquakes. These millennial-scale records of fault slip are consistent with historical slip behavior at Parkfield and imply that additional slip

may be partitioned among structures adjacent to the SAF. This result supports the hypothesis that intrinsic differences in fault zone materials lead to long-lived, segmented configurations of slip behavior.

SITE DESCRIPTION AND CHANNEL OFFSET

The Miller's Field paleoseismic site is a deformed late Holocene terrace of Little Cholame Creek. The site geomorphology and fault trace geometry is well illustrated by the 2004 earthquake fractures (Fig. 3.2). A right-step in the surface trace of the right-lateral SAF forms a sag pond. Southeast of the sag, a left bend in the fault trace has produced a 1-3 m high, southwest-facing, pressure ridge. At the sag pond, an incisional channel is right-laterally offset by 18.5-23.0 m (Fig. 3.2). The age of the channel is constrained to be younger than the terrace into which it has incised and older than the first sandy sag pond fill. Its position along the SAF is likely influenced by the funneling of water between the sag and pressure ridge and provides an opportunity to measure a SAF slip rate.

PALEOSEISMIC INVESTIGATIONS

We opened six paleoseismic trenches in two field seasons at the Miller's Field; two fault-perpendicular trenches across the pressure ridge (PT04, PT07), three fault-perpendicular trenches across the sag pond (MST04, MST07, and MST07c) and a fault parallel trench across the upstream side of the offset channel (MST07p). For each trench (except the collapsed MST07c) we logged the stratigraphy, structures, and charcoal sample locations at 1:20 scale. Charcoal

samples were used for radiocarbon analysis (Appendix C). Discussions herein focus on MST07 (Fig. 3.3). Complete logs of the 2004 (Toké et al., 2006) and 2007 trenches can be found in the supplementary materials (Appendices D-E).

Terrace and Sag Pond Stratigraphy – Age of Offset

Trench MST07 (Fig. 3.3) reveals a sequence of faulted overbank terrace deposits overlain by sag fill consisting of reworked terrace sediment. Some units are bounded by thin charcoal-rich horizons which we utilized for radiocarbon analyses. We hypothesize these charcoal-rich horizons formed by charcoal settling out during the waning stages of paleofloods of Little Cholame Creek. Several units have undergone significant pedogenic alteration, exhibiting thick, clayey, organic-rich, buried soil horizons (e.g., units MSE-104 and MSE-108). These pedogenically altered deposits were tilted and down-faulted across fault zone 1 (FZ1). MSE-108 represents the soil column that was forming during the development of the sag pond fault scarp. Therefore MSE 108 underlies the sag pond stratigraphy, but also thickens across the fault scarp where soil development was contemporaneous with sag filling.

The age of the offset channel's incision is constrained by the age of the terrace into which it incises and the age of the sag pond stratigraphy which records its erosion of the uplifted side of the fault scarp. The onlapping sag units (MSE109-MSE 119) alternate between dark, clayey, organic-rich horizons and units of lighter, sandy material. Initially, sag fill (MSE-109 and MSE-110) consisted of the reworked sediments of soil horizon MSE-108. Unit MSE-109 is

clayey silt which is differentiated from MSE-108 by a thin discontinuous charcoal-rich horizon with a 2σ calibrated radiocarbon age of 890-1040 A.D. (charcoal stringer: Fig. 3.3). This horizon represents the age of the Little Cholame Creek terrace and a maximum age for the offset channel's incision (Fig. 3.4). Once the channel incised through the o-horizon of the soil column it eroded the underlying stratigraphy and deposited sandy material within the sag. The presence of the first sandy deposit (MSE-111) indicates that the channel had incised significantly into the terrace. The 2σ radiocarbon age from MSE-111 (1410-1450 A.D.) represents the minimum age of channel incision.

Indicators of Creep and Moderate Magnitude Earthquakes

The sequence of sag pond stratigraphy is down-warped and offset across fault zones 2-3 and buttressed against fault zone 4 (Fig. 3.3). Fault zones are delineated by multiple, sub-vertical, thin bands of clay-rich material (clay fault strands) that separate displaced units and extend into the uppermost stratigraphy. In addition to apparent vertical displacement across these faults, changes in unit thicknesses are consistent with right-lateral slip. The trench walls of both PT07 and MST 07 failed repeatedly along these structures, exposing the three dimensional orientation of these clay fault strands (345±15°; Fig. 3.3D). This is a clockwise-oblique orientation relative to the local SAF strike (313°) and corresponds to the orientation of the opening mode surface fractures that grew as post-seismic after slip from the 2004 Parkfield earthquake (e.g., Fig. 3.2; Toké et al., 2006).

We postulate that the obliquely-oriented clay fault strands which pervade these trenches form through repeated cycles of moderate magnitude earthquakes and creep: In a single moderate magnitude earthquake, a set of overlapping left-stepping clockwise-oblique opening mode fractures with centimeter-scale right-lateral offset is formed. These open fractures later fill with fine sediment derived from overland flow and dust and heal by soil shrink-swell. Over many moderate magnitude earthquake cycles, numerous healed fracture sets form. Because the fault also creeps, each fracture set is intermittently active, allowing the clay fault strands to accommodate significant offset and extend to the surface.

SLIP RATE ANALYSIS

Following recent efforts to standardize slip rate reporting with probability density functions (PDFs), we used the software of Zechar and Frankel (2009) to present the range of offset measurements and ages that can be used to estimate a slip rate at this site. The broad downstream shape of the channel's thalweg yields a right-lateral offset of 18.5-23.0 m (Fig. 3.2). The age of the channel's incision is bracketed using the MST07 stratigraphy, providing an offset age of 890-1450 A.D. (Fig. 3.3 and Appendix C). The uncertainty in displacement and age can be approximated using Gaussian (normal) or conservative "Box-Car" (uniform) PDFs.

If we presume that the downstream thalweg of the offset channel has widened through time and the processes controlling widening act equally on each bank, a Gaussian PDF is the most appropriate for representing the displacement.

For the age of channel incision, we know the channel pre-dates the deposition of MSE-111 and post-dates the deposition of MSE-109. Because we have no additional constraints, we deem a uniform PDF to be most representative. Thus, the preferred PDF combination (Fig. 3.4) is produced by a Gaussian displacement PDF combined with a Box-Car age of offset PDF. This yields a 1 σ slip rate of 26.2 +6.4/-4.3 mm/yr and a 2 σ rate of 24.8 +12.2/-6.6 mm/yr. The full range of displacement and age of offset PDFs are presented in Appendix G.

DISCUSSION

The error bounds on the slip rate measured herein overlap with the 33.9 ± 2.9 mm/yr Holocene slip rate measured in the Carrizo Plain (Sieh and Jahns, 1984), but the PDFs (Fig. 3.4) suggests that the slip rate at Parkfield is less than 30 mm/yr for main trace of the SAF. This finding is similar to the result of Sims (1987) who estimated a rate of 26.3 +3.9/-3.3 mm/yr at the Water Tank site (Fig. 3.1). Near the Miller's Field, the SAF creeps at ~10 mm/yr (e.g., Lienkaemper and Prescott, 1989). With the addition of slip from moderate magnitude ruptures since 1857 (6 earthquakes, each with ~40cm of slip) we estimate that main SAF trace has a historical slip rate of ~25 mm/yr. This is comparable to the millennial-scale rate measured here. Moreover, all of the structures within these trenches are consistent with deformation from creep and moderate magnitude earthquakes.

This result implies that the historically-observed slip mechanisms of creep and moderate magnitude earthquakes have persisted for at least a millennium along the Parkfield section and that significant slip may be accommodated by

structures in the wider SAF zone. Along the creeping section of the fault Titus et al., (2006) demonstrated that 200 m alignment arrays record ~25 mm/yr of slip, while 1 km aperture GPS stations yield a slip rate of 28.2 ± 0.5 mm/yr. Thus, at least 10% of the surface slip is distributed diffusely off the SAF trace. At Parkfield there is also the SWFZ (Fig. 3.1), which is linked to the SAF at depth (Simpson et al., 2006) and slipped in both the 1966 (~8 cm: Lienkaemper and Prescott, 1989) and 2004 (~7 cm: Lienkaemper 2006) earthquakes. These offsets yield a maximum SWFZ slip rate of 4 mm/yr since 1966. The White Canyon Fault Zone (WCFZ; Fig. 3.1) is another nearby lineament that may accommodate distributed SAF slip. Farther afield, Platt and Becker (2010) present geodetic modeling, without imposing pre-existing faults, across the Pacific/North American plate boundary to infer that ~9 mm/yr of slip may be accommodated along structures West of the SAF such as the San Gregorio-Hosgri and Rinconada Faults (Fig. 3.1A). However, this is at odds with the WGCEP report (e.g., Wills et al., 2008), which states that the combined slip rate from the Rinconada and San Gregorio-Hosgri Faults is 3.5 ± 2 mm/yr. To better determine the seismic hazard posed by these faults and the distribution of plate boundary slip, future studies should target slip rate investigations along faults other than the main SAF, including its structurally-linked neighbors, the SWFZ and WCFZ.

Obliquely-oriented clay fault strand fabrics may be useful for distinguishing surface slip due to moderate magnitude earthquakes and creep from deformation produced by large magnitude earthquakes with multi-meter surface displacement. Despite locating our trenches along topographic inflections, where

one would anticipate the production of fissures and colluvial wedges, no good evidence for large surface ruptures was observable (including 1857). Because slip from a single rupture can vary by a factor of 2-3 within several hundred meters (e.g., Ambraseys and Tchalenko, 1969) and the Miller's Field site only spans ~200m along the SAF, it is possible that evidence for larger ruptures may be preserved elsewhere. However, the paleoseismic evidence at this site suggests that the historical modes of slip release at Parkfield (creep and moderate magnitude earthquakes) have persisted for the last few millennia and thus supports the hypothesis that the configuration of SAF slip behavior is controlled by fault zone material properties, intrinsic to each section of the fault.

ACKNOWLEDGMENTS

We thank J. Tinsley, D. Ponti, and three anonymous reviewers for help improving this manuscript. We thank J. Zechar for slip rate PDF discussion and T. Fumal for visiting the site. The 2007 campaign was supported by NEHRP Grant 07HQGR0094 and the Southern California Earthquake Center: Contribution #1452. SCEC is funded by NSF Cooperative Agreement EAR-0106924 and USGS Cooperative Agreement 02HQAG0008. Our 2004 work was funded by NSF Grant EAR00310357. NSF IGERT in Urban Ecology Grant DGE 0504248 also supported N. Toké. A. Landgraf's availability was courtesy of German Academic Exchange Service Grant DAAD-D/07/42739. Measurement of offset was enhanced by B4 LiDAR DEMs which were processed at and are available from http://www.opentopography.org.

REFERENCES CITED

Ambraseys, N.N. and J.S. Tchalenko, 1969, The Dasht-e Bayāz (Iran) Earthquake of August, 31, 1968: A Field Report: Bulletin of the Seismological Society of America, v. 59, no.5, p. 1751-1792.

Ben-Zion, Y., Dahmen, K., Lyakhovsky, V., Ertas, D., Agnon, A., 1999, Self-Driven Mode Switching of Earthquake Activity on a Fault System: Earth and Planetary Science Letters, v. 172, p. 11-21.

Lienkaemper, J. J., Baker B., and McFarland F. S., 2006, Surface slip associated with the 2004 Parkfield California, earthquake measured on alignment arrays: Bulletin of the Seismological Society of America, v. 96, no. 4B, p. S239–S249, doi: 10.1785/0120050806

Lienkaemper, J.J., 2001, 1857 slip on the San Andreas fault southeast of Cholame, California: Bulletin of the Seismological Society of America, v. 91, no. 6, p.1659-1672, doi: 10.1785/0120000043

Lienkaemper, J.J. and Prescott W.H., 1989, Historic Surface Slip along the San Andreas Fault near Parkfield California: Journal of Geophysical Research, v. 94, p. 17647-17670.

Meade, B.J. and Hager B.H., 2005, Block models of crustal motion in southern California constrained by GPS measurements: Journal of Geophysical Research, v. 110, B03403, doi:10.1029/2004JB003209

Moore, D.E. and Rymer, M.J., 2007, Talc-bearing serpentinite and the creeping section of the San Andreas Fault: Nature, v. 448, p. 795-797, doi:10.1038/448756a

Perkins, J.A., J.D. Sims, and S.S. Sturgess, 1989, Late Holocene Movement Along the San Andreas Fault at Melendy Ranch: Implications for the Distribution of Fault Slip in Central California: Journal of Geophysical Research, v. 94, no. B8, p. 10,217-10,230, doi: 10.1029/JB094iB08p10217

Platt, J.P. and Becker T.W., 2010, Where is the true transform boundary in California?: Geochemistry, Geophysics, and Geosystems doi:10.1029/2010GC003060

Sieh, K.E. and Jahns R.H., 1984, Holocene activity of the San Andreas fault at Wallace Creek, California: Geological Society of America Bulletin v. 95, p. 883-896.

Simpson, R.W., Barall, M, Langbein, J., Murray, J.R., and Rymer, M.J., 2006, San Andreas Fault Geometry in the Parkfield, California, Region: Bulleting of

the Seismological Society of America, v. 96, no 4B, p. S28-37, doi: 10.1785/0120050824.

Sims, J. D., 1987, Late Holocene slip rate along the San Andreas Fault near Cholame, California: Geological Society of America, Cordilleran Section, Abstracts with Programs v. 83, p. 451.

Titus, S.J., C. DeMets, and B. Tikoff, 2006, Thirty-five-year creep rates for the creeping segment of the San Andreas fault and the effects of the 2004 Parkfield earthquake: constraints from alignment arrays, continuous GPS, and creepmeters: Bulletin of the Seismological Society of America, v. 96, no. 4B, p. S250-S268 doi: 10.1785/0120050811.

Toké, N.A. and Arrowsmith J R., 2006, Reassessment of a Slip Budget along the Parkfield segment of the San Andreas Fault: Bulletin of the Seismological Society of America v. 96, no. 4B, p. S339–S348, doi: 10.1785/0120050829.

Toké, N.A., Arrowsmith J R., Young J.J., and Crosby C.J., 2006, Paleoseismic and Postseismic Observations of Surface Slip along the Parkfield Segment of the San Andreas Fault: Bulletin of the Seismological Society of America, v. 96, no. 4B, p. S221–S238, doi: 10.1785/0120050809.

Wills, C.J., Weldon, R.J., II, and Bryant, W.A. 2008, California fault parameters for the National Seismic Hazard Maps and Working Group on California Earthquake Probabilities, Appendix A in The Uniform California Earthquake Rupture Forecast, version 2 (UCERF 2):U.S. Geological Survey Open-File Report 2007-1437A, and California Geological Survey Special Report 203A, 48 p. http://pubs.usgs.gov/of/2007/1437/a/.

Zechar, J.D. and Frankel, K.L., 2009, Incorporation and reporting uncertainties in fault slip rates: Journal of Geophysical Research – Solid Earth, v. 114, B12407, doi:10.1029/1009JB006325.

Zielke, O., Arrowsmith, J R., Grant-Ludwig, L., and Akciz, S.O., 2010, Slip in the 1857 and Earlier Earthquakes along the Carrizo Plain, San Andreas Fault: Science, v. 327, no. 1119-1122. DOI: 10.1126/science.1182781.

Figure 3.1. A) The Parkfield section of the San Andreas Fault (SAF) is located at the southeast end of the central California creeping section (bold grey line) between areas of the SAF that ruptured in 1906 and 1857 (bold black lines). Thin grey lines represent other major faults in California, note the Hosgri (HF) and Rinconada (RF) faults west of the SAF. B) The Miller's Field paleoseismic site (Fig 3.2) is ~1 km south of the town of Parkfield. The 2004 and 1966 Parkfield earthquakes ruptured both the main SAF and the Southwest Fracture Zone (SWFZ; see Appendix B). In addition to the SWFZ, the White Canyon Fault Zone is a prominent geomorphic lineament. The only other geologic slip rate study between the creeping section and the Carrizo Plain was Sims, (1987) Water Tank site.

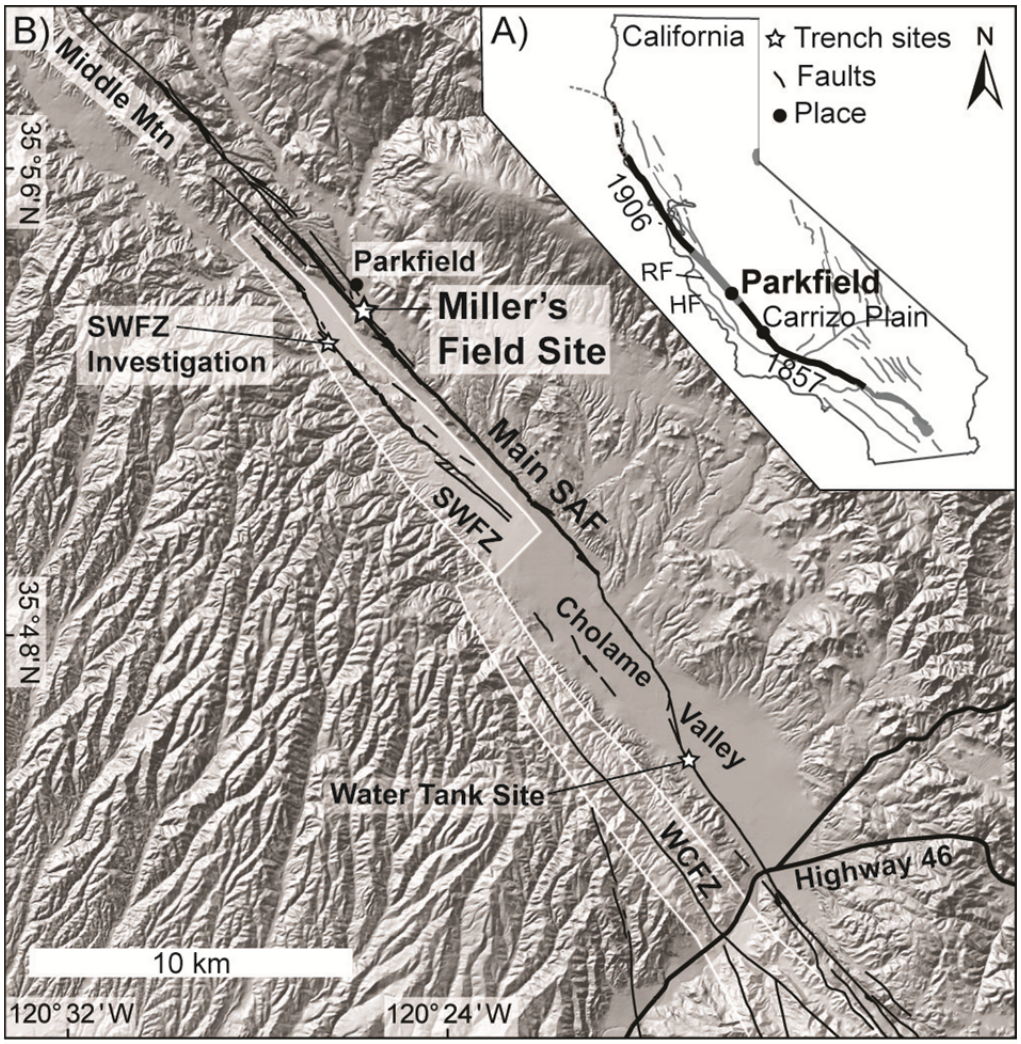
B)
Middle Mtn
35°56'N
Parkfield
Miller's
Field Site
SWFZ
Investigation
Main SAF
SWFZ
Cholame
Valley
35°48'N
Water Tank Site
WCFZ
Highway 46
10 km
120°32'W
120°24'W
A)
California
Trench sites
Faults
Place
N
1906
RF
HF
Parkfield
Carrizo Plain
1857

Figure 3.2. (A) The Miller's Field paleoseismic site. Trench footprints are labeled by site and year (e.g., MST07 = Miller Sag Trench 2007; Fig. 3.3). Fractures from the 2004 rupture delineate the surface trace of the SAF including the sag pond step-over and pressure ridge scarp. An incised channel is right-laterally offset at the southeast end of the sag (view is expanded in panel B; black box). The offset was measured (panel C) by extracting fault-normal profiles across the displaced channel thalweg (x-z on panels B and C) using a 0.5 m B4 LiDAR-derived digital elevation model. Additional paleoseismic trench logs are provided in Appendix D and E.

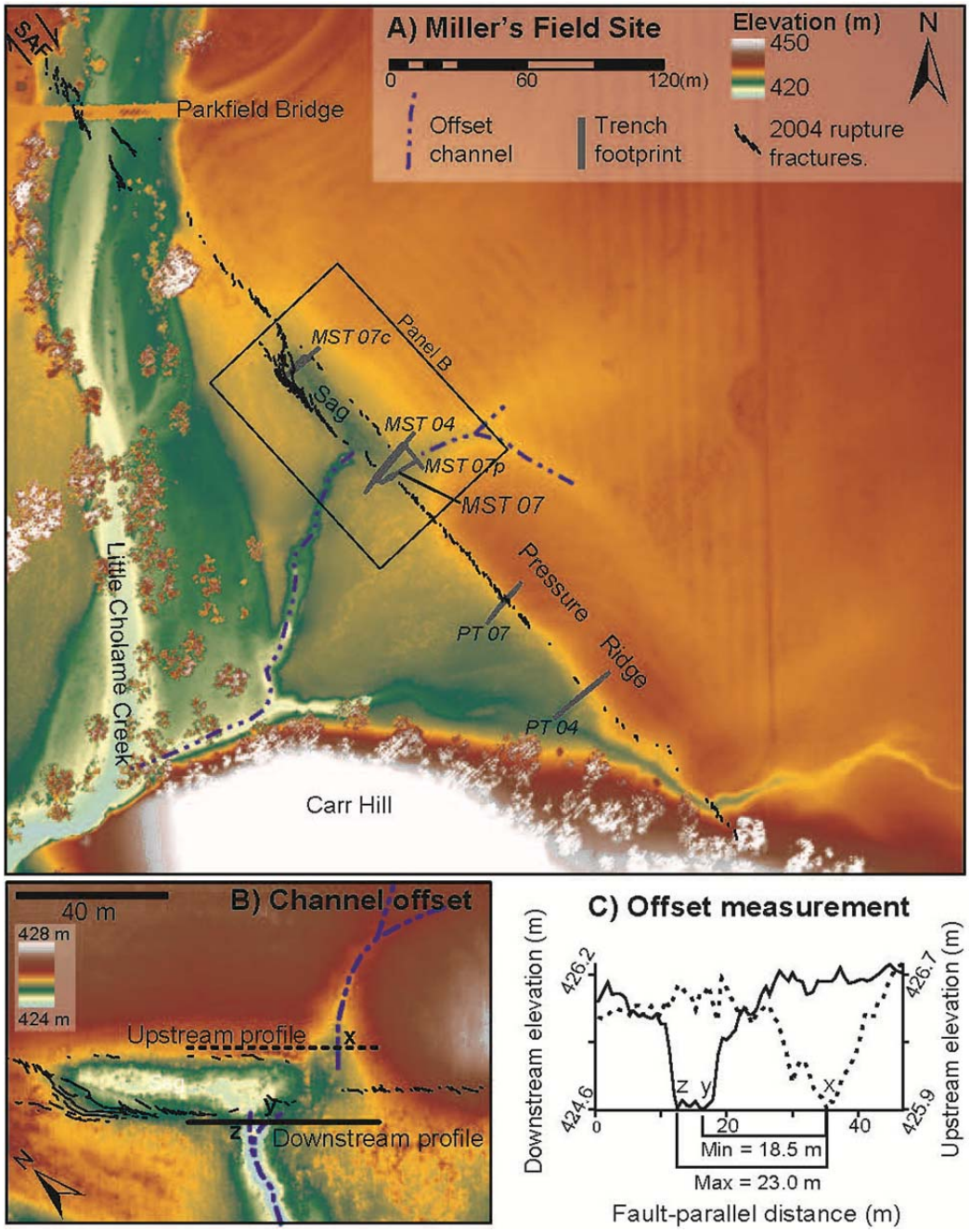
A) Miller's Field Site
Elevation (m)
450
420
N
0
60
120(m)
Offset channel
Trench footprint
2004 rupture fractures.
SAF
Parkfield Bridge
Panel B
MST 07c
Sag
MST 04
MST 07p
MST 07
Pressure Ridge
PT 07
PT 04
Little Cholame Creek
Carr Hill
B) Channel offset
40 m
428 m
424 m
Upstream profile
Downstream profile
x
y
z
N
C) Offset measurement
Downstream elevation (m)
Upstream elevation (m)
426.2
424.6
426.7
425.9
0
20
40
Min = 18.5 m
Max = 23.0 m
Fault-parallel distance (m)

Figure 3.3. (A) The MST07se trench log. Deformation is concentrated along four fault zones (FZ1-FZ4). Each zone is composed of multiple clay fault strands that accommodate offset and extend into the uppermost stratigraphy (Appendix F). Individual fault strands are oriented obliquely to the strike of the SAF (panel D). Across FZ1, MSE-108 is down warped and offset. MSE-108 represents the pre-sag terrace surface and uppermost soil horizon. Thus it underlies the sag fill sequence and the sag fill deposits are partially derived from it. The units on the hanging wall of FZ1 have been pedogenically altered to a dark clayey material due to enhanced fluid flow and vegetation growth along the scarp (panel B). Unit MSE-109 is the first onlapping sag fill. The first sandy deposit, MSE-111 was deposited once the offset channel (Fig. 3.2) incised through the o-horizon of the terrace soil column. Radiocarbon ages (Appendix C) of the charcoal deposited between MSE-108 and MSE-109 and charcoal pieces within MSE-111 bracket the oldest and youngest ages of channel incision (Fig. 3.4).

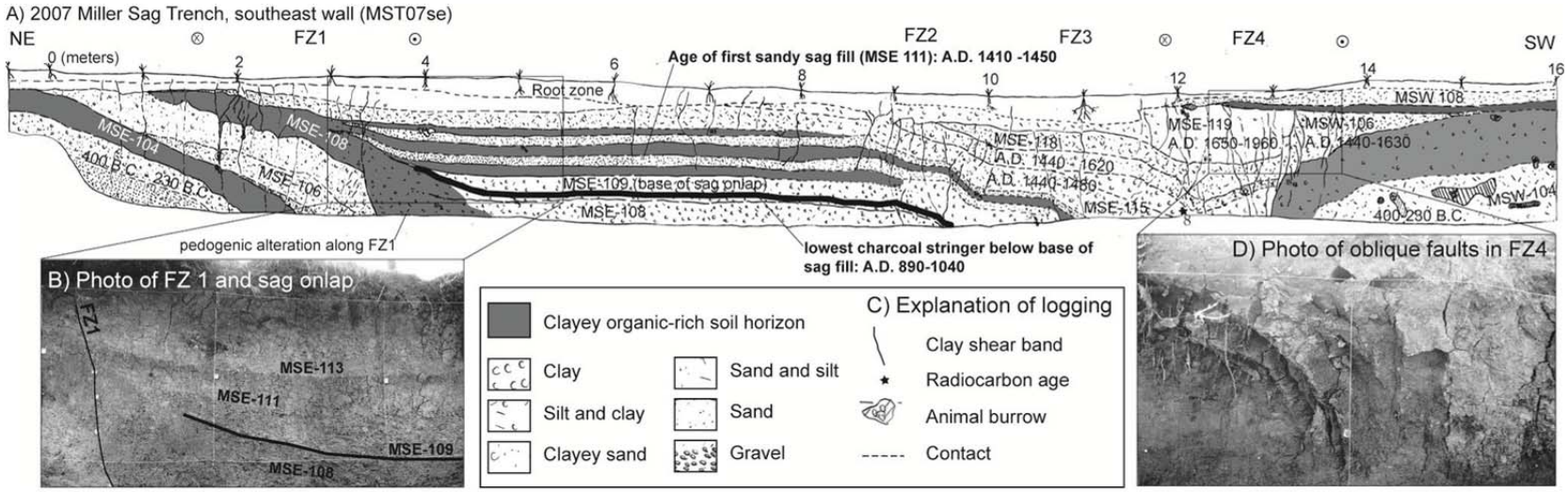
A) 2007 Miller Sag Trench, southeast wall (MST07se)
NE
FZ1
FZ2
FZ3
FZ4
SW
0 (meters)
Root zone
Age of first sandy sag fill (MSE 111): A.D. 1410 -1450
MSE-104
400 B.C. - 230 B.C.
MSE-108
MSE-106
MSE-109 (base of sag onlap)
MSE-108
MSE-118
A.D. 1440 - 1620
A.D. 1440-1480
MSE-115
MSE-119
A.D. 1650-1960
MSW-106
A.D. 1440-1630
MSW 108
MSW-104
400-290 B.C.
pedogenic alteration along FZ1
lowest charcoal stringer below base of sag fill: A.D. 890-1040
B) Photo of FZ 1 and sag onlap
FZ1
MSE-113
MSE-111
MSE-109
MSE-108
C) Explanation of logging
Clayey organic-rich soil horizon
Clay
Silt and clay
Clayey sand
Sand and silt
Sand
Gravel
Clay shear band
Radiocarbon age
Animal burrow
Contact
D) Photo of oblique faults in FZ4

Figure 3.4. Probability density functions (PDFs) for displacement, age, and slip rate. Gaussian PDFs bracket the estimated channel displacement (A; Fig. 3.2). Box-Car PDFs bracket the age of channel incision (B; Fig. 3.3 and Appendix C). Slip rate PDFs derived by combining Gaussian displacement PDFs and Box-Car age PDFs (C). This is the preferred PDF combination; additional permutations are explained in Appendix G.

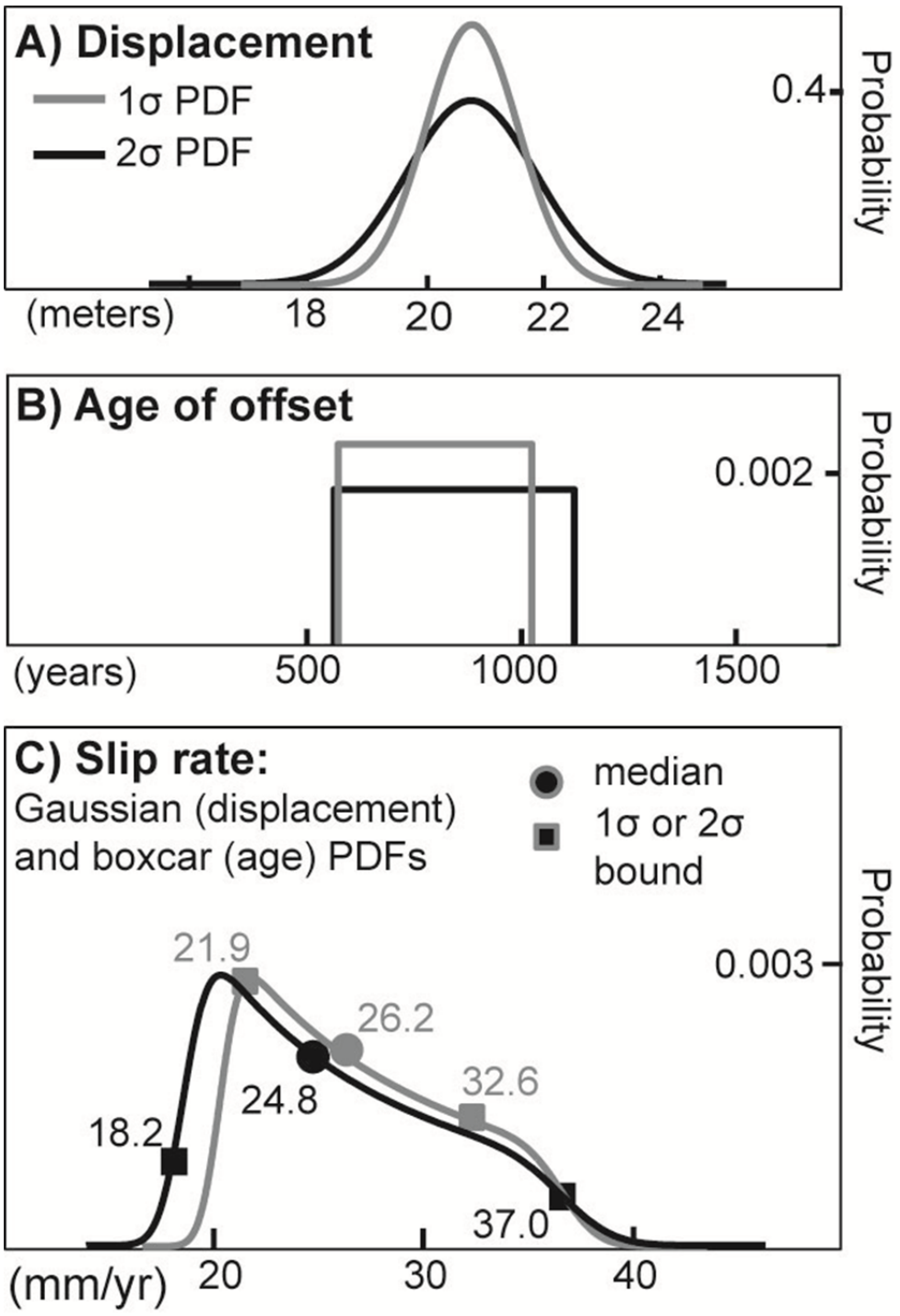
A) Displacement
1σ PDF
2σ PDF
0.4
Probability
(meters)
18
20
22
24
B) Age of offset
0.002
Probability
(years)
500
1000
1500
C) Slip rate:
Gaussian (displacement)
and boxcar (age) PDFs
median
1σ or 2σ
bound
0.003
Probability
21.9
26.2
32.6
24.8
18.2
37.0
(mm/yr)
20
30
40

CHAPTER 4

REFINING SEGMENTATION ALONG THE CENTRAL SAN ANDREAS FAULT USING FAULT SCARP ARRAY GEOMETRY AND MORPHOLOGY FROM HIGH RESOLUTION DIGITAL ELEVATION MODELS

ABSTRACT

Fault segmentation has been chiefly defined through mapping changes in fault geometry, such as bends and step-overs, with the goal of providing structural models that can help predict fault rupture dynamics. Additionally, observations of along-strike variations in historical ruptures are used to define fault segments and test structural models. Tests show that large geometric changes do arrest earthquakes. However, over the same reach of fault individual ruptures can extend for hundreds of kilometers and other times only rupture in small patches. Because residual fault scarps represent the composite record of many earthquakes, we utilized 0.5 m LiDAR digital elevation models along 122 km of the central San Andreas Fault (SAF) to characterize fault trace geometry and define fault segmentation using the geomorphic signature of past earthquakes.

From variations in the complexity of fault scarp array geometries and scarp morphology we infer seven segments along the central SAF, ranging from 14-28 kilometers in length. Only one of these segment boundaries corresponds to existing Working Group on California Earthquake Probabilities' definitions of segmentation: between the Carrizo and Cholame sections of the SAF. Geometric fault array complexity indicates that the Cholame and Parkfield sections are

segmented at shorter length scales which correspond to the wavelength of interaction between the main SAF and secondary active structures. Segments of high scarp array complexity exist where these structures converge and interact. The wavelength of interaction is on the same order of magnitude as depth of the seismogenic crust. Finally, fault scarps are steeper to the northwest where the SAF has experienced historical creep and moderate magnitude earthquakes.

INTRODUCTION

Paleoseismology is the science of determining the age, slip, and extent of prehistoric earthquakes. This is done by interpreting the geomorphic record of tectonically-influenced landforms and associated records of deformation within sediments that cross faults (e.g., McCalpin, 1996). More holistically, earthquake geology uses paleoseismology from many sites along multiple faults in conjunction with records of tectonic deformation revealed by landforms ranging from fault scarps to mountain ranges (tectonic geomorphology: e.g., Burbank and Anderson, 2005) to study the mechanics of earthquakes, faulting, and fault interactions within plate boundaries and fault systems. Combined with geophysical observations, these areas of research allow us to study faults and earthquakes over timescales relevant to society, forming the field of active tectonics (e.g., Keller and Pinter, 2002).

One of the primary goals of these areas of research is to understand what controls the extent of earthquake ruptures along long plate boundary faults such as the San Andreas (Figure 4.1). At the forefront of geologic explanations has been

the idea of fault segmentation (e.g., Schwartz and Coppersmith, 1984; King and Nabelek, 1985; Wesnousky, 1988; Machette et al., 1989; Knuepfer, 1989; Weldon et al., 2004; Wesnousky, 2006), which is the hypothesis that variations in fault zone structure, geometry, and composition place fundamental constraints on the dynamics of earthquake ruptures and fault slip behavior over many earthquake cycles. Segmentation is an attractive hypothesis because it provides a predictive model for integrating paleoseismic results (e.g., Schwartz and Coppersmith, 1984; Machette et al., 1989; Weldon et al., 2004) and because geometrical discontinuities along faults do arrest earthquake ruptures (e.g. Wesnousky, 2006), and may also be associated with rupture nucleation (e.g., King and Nabelek, 1985; Duan and Oglesby, 2005, Duan and Oglesby, 2006). Unfortunately, earthquakes are not purely characteristic. Paleoseismic and historical data indicate that ruptures of vastly different sizes occur along the same fault segments (e.g., Weldon et al., 2005; Ackciz et al., 2010). Thus, there may be hierarchies of segmentation (e.g., Moore and Byerlee, 1990) which, from a predictive standpoint, one would hope may be related to rupture variations and therefore would be recorded within the geomorphology of fault zones.

Fault scarps are topographic discontinuities on the earth's surface due to displacement from slip along a fault. Slip may be generated from earthquakes, aseismic fault creep, or both. Regardless of the source of the topographic discontinuity, the persistence of a fault scarp depends on the rate of tectonic displacement, the rate of diffusive hillslope processes (which act to smooth scarp discontinuities: e.g., Nash, 1984; Hanks et al., 1984; Arrowsmith et al., 1998;

Hanks, 2000), the occurrence of landslides, and the deposition of sediments which may obscure a scarp. Along the central San Andreas Fault (SAF; Fig. 4.1 and panel A of Figs. 4.2-4.4; e.g., Wallace 1990) where slip rates are high (e.g., Meade and Hagar 2005; Sieh and Jahns, 1984) and the climate is dry, even subsidiary faults retain a geomorphic signature of tectonic displacement over thousands of years (e.g., Lawson, 1908; Wallace, 1973; Sieh, 1978; Arrowsmith et al., 1998; Arrowsmith and Zielke, 2009). These residual fault scarps (Stewart and Hancock, 1990) provide a record of tectonic deformation that spans many earthquake cycles. Because these scarps are a direct product of many ruptures which have occurred along the SAF, analyses of their geometry and morphology may help elucidate information about fault zone segmentation, the rates and style of deformation along this reach of the San Andreas Fault, and about the dynamics of earthquake ruptures.

In 2005 high resolution digital elevation data became available along the San Andreas and San Jacinto faults through the technology of airborne laser swath mapping (ALSM) also referred to as light distance and ranging (LiDAR). The LiDAR collected along these faults is called the B4 project (e.g., Bevis et al., 2005 and Toth et al., 2007). The name B4 was given in reference to the well-known long period of seismic quiescence along these faults and subsequent likelihood of experiencing a large surface rupturing earthquake in the near future (e.g., Field et al., 2008). By imaging the fault prior to the next large earthquake the B4 project lays the groundwork for future documentation of precise changes in the landscape following major surface rupture(s) with a repeat laser scan. Now,

prior to the next surface rupturing earthquake, the B4 data present an excellent opportunity to quantify the state of tectonic landforms and fault scarps across a 1.5 km width of the fault zone.

This data has already proven extremely useful for refining our knowledge of the last great earthquake along the central and southern SAF (Zielke et al., 2010) that occurred in 1857, at the dawn of the historical earthquake record in California. Zielke et al., (2010) used the B4 data to document numerous, but previously-unobserved, low relief channels that were offset about five meters by the 1857 earthquake. These small incisional channels are challenging to discern in the field and were largely unrecognized in seminal field investigations (Wallace, 1968 and Sieh, 1978). Those early studies concluded that the smallest offsets in 1857 were closer to ten meters. Thus, our fundamental knowledge of the 1857 rupture dynamics was changed using this new data.

Extending analyses beyond channel offsets, Arrowsmith and Zielke (2009) showed that user-inferred B4 LiDAR fault zone mapping compares well with traditional methods of field-based strip mapping of faults (e.g., Vedder and Wallace, 1970). Moving toward automated mapping, Hilley et al., (2010) developed a geomorphic search algorithm to map the locations and orientations of fault scarp scarps along multiple sections of the SAF. By incorporating prior knowledge about the fault trend, they were able to produce a fault trace map that closely resembles pre-existing fault strip maps (e.g., Vedder and Wallace, 1970). Their method of automated mapping does a good job of identifying the areas over which fault scarp morphology influences the landscape and it provides assessment

of scarp morphologic ages. However, as of yet, these automated methods do not produce precisely-located infinitesimal fault trace lines. Delong et al. (2010) integrated field mapping, user inferred remote mapping, and automated Fourier transform analyses of LiDAR-based digital elevation models (DEM) along the creeping section of the SAF. This integrative approach proved helpful for refining preexisting field mapping and provided an important assessment of the relative active of subsidiary fault splays along this portion of the SAF. Clearly, LiDAR is a powerful tool for the study of earthquake geology.

The resolution of the B4 dataset permits the production of DEMs with pixel sizes as small as 0.25 to 0.5 meters and centimeter-scale vertical accuracy (Arrowsmith and Zielke, 2009). With this data we can identify geomorphic offsets with more than 1 meter of strike-slip displacement and measure horizontal displacements that are greater than 2 meters with confidence. While these are horizontal limitations that could hinder future investigations of large earthquakes with less than 2 meters of slip (e.g., Wells and Coppersmith, 1994), the ability to resolve centimeter-scale vertical offsets provides the potential for detailed mapping of fault scarps (e.g., Oskin et al., 2007; Arrowsmith and Zielke, 2009; Delong et al., 2010) . This has proven to be true even in regions with significant tree canopy (e.g., Haugerud et al., 2003; Sherrod et al., 2004) or urban land cover (e.g., Kondo et al., 2008).

In this paper, I present preliminary results from mapping the most prominent fault scarps along 122 kilometers of the central SAF from the Bidart Fan paleoseismic site in the Carrizo Plain to the northwest terminus of the B4 data

set in the southeastern portion of the creeping section of the fault (Fig. 4.1). Using this mapping, I measured fault scarp array geometries and extracted scarp slopes using the B4 DEM products. These analyses allowed me to characterize fault trace complexity along the central SAF. This region of the SAF corresponds to an enigmatic shift in fault slip release behavior as well as several other variations including slip rate, lithology, elevation, and precipitation (described in the next section). Analyses show that this part of the fault can be grouped into seven segments corresponding to fault scarp array geometrical complexity. Also, scarp geometrical complexity is related to rock type, rock age, and the broader-scale fault zone structure. Finally, scarp morphology, as expressed by slope, is linked to the appearance of aseismic fault creep to the northwest.

First, I provide an overview characterizing the central SAF and existing Working Group on California Earthquake Probabilities (WGCEP: e.g., Field et al., 2008) ideas about its segmentation (Figs. 4.1 and panel A of 4.2-4.4). Next, I describe my fault scarp mapping methodology (Fig. 4.5) and corresponding methods for extracting fault scarp array complexity measurements from LiDAR DEMs (Fig. 4.6). Then I present the results of this extraction both quantitatively (Figs. 4.2-4.4 and Table 4.1) and qualitatively with mapping examples from areas of the fault with varying scarp morphologies (Figs. 4.5-4.11). Finally, I discuss the general conclusion that existing fault sections can be divided into smaller fault segments based upon scarp array complexity (Fig. 4.12 and Table 4.1) and explore the implications of this result.

CHARACTERIZING THE CENTRAL SAF

From southeast to northwest, the central SAF has been characterized by WGCEP to consist of four fault sections: the Carrizo, Cholame, Parkfield and creeping sections (Field et al., 2008). These sections are defined based upon expert scientific opinions (Marzocchi and Zechar, 2011) and considering the following geophysical and geologic observations of fault behavior along the central SAF.

The central SAF, especially along the Carrizo Plain (Moore and Byerlee, 1991), is straighter and surrounded by fewer sub-parallel faults than the southern SAF (Fig. 4.1). Thus, it accommodates a greater portion of the plate boundary slip (e.g., Meade and Hager, 2005). Yet, the central SAF presents an enigmatic contrast in fault slip behavior (e.g., Allen, 1968) from steady right-lateral aseismic creep of ~30 mm/yr in the northwest (e.g., Titus, 2006; Titus et al., 2011) to the locked Carrizo section in the southeast which last slipped in the 1857 Fort Tejón Earthquake (e.g., Sieh, 1978; Zielke et al., 2010). This change in slip behavior is accommodated across the transitional Parkfield section of the SAF (Toké and Arrowsmith, 2006) where the aseismic slip-rate decreases to zero across 40 km of the fault (Figs. 4.2-4.4 panel B; e.g., Murray et al., 2006, Lienkaemper et al., 2006; Lisowski and Prescott, 1981) and a series of historical ~M6 earthquakes have occurred (e.g., Rymer et al., 2006; Lienkaemper and Prescott, 1989).

Between the Carrizo Plain and Parkfield lies a section referred to as Cholame. The Cholame section was differentiated from the Carrizo by paleoseismic studies which inferred significantly greater 1857 slip release in the

Carrizo (6-10 meters: Sieh, 1978; Grant and Sieh, 1993) than in Cholame (3-5 meters: Sieh, 1978; Arrowsmith et al., 1997; Young et al., 2002) and related geophysical analyses, such as Hilley et al., (2001), that used these geomorphic data to infer contrasts in fault strength and deep fault geometry across these sections of the SAF. Continued analyses of geomorphic offsets revealed that some in Cholame were larger (4-6 meters: Lienkaemper, 1989 and Lienkaemper, 2001) and complete re-evaluation of the 1857 reach using high resolution B4 LiDAR showed that many subdued incisional channels were previously-unrecognized and offset about 5 meters throughout the Carrizo Plain (Zielke et al., 2010). Thus slip in the last earthquake, 1857, was likely uniform over these two sections of the SAF. These new results are important for both future paleoseismic interpretations and our geophysical understanding of the SAF.

Recent paleoseismology along the Parkfield section (Toké et al., 2011) demonstrated an absence of evidence for large surface rupturing earthquakes for at least 1000 years, indicating that large ruptures on the locked portion of the fault have not broken through this transitional section recently. Additionally, slip rate analyses suggest that the main SAF trace may accommodate several millimeters per year less slip in Parkfield (26.2 +6.4/- 4.3 mm/yr; Toké et al., 2011) than 100 km southeast in the Carrizo (~33.9 ± 2.9 mm/yr; e.g., Sieh and Jahns, 1984). Given that far field geodetic measurements match the slip rates estimated along the Carrizo (35.9 ± 0.5 mm/yr over a ~100 km width; e.g., Meade and Hager, 2005; Schmalzle et al., 2006) it is likely that the difference in slip rate at Parkfield

is accommodated as distributed strain along additional seismogenic structures (Toké et al., 2011: See white lines in Figs 4.2-4.4 and 4.12).

In addition to changes in slip release behavior and slip rate, there are lithological differences between the northwest and southeast ends of the central SAF. In the northwest, near the San Andreas Fault Observatory at Depth (SAFOD; e.g., Bradbury et al., 2007; Zoback, et al., 2010) the fault juxtaposes Tertiary-Quaternary sandstones, mudstones (QPc on panel A of Figs. 4.2-4.4), and Salinian Granite on the west against marine sandstones, conglomerates, and the Franciscan Assemblage, (Tsm, Tsh, and KJF) which includes talc-bearing serpentinite, on the east side of the fault (e.g., Thayer, 2006; Bradbury, 2007). Whereas in the southeast, the SAF cuts through Salinian granite overlain by marine sandstone and conglomerate on both sides of the fault (e.g., Dibble, 1973). The Franciscan's appearance within the fault zone northwest of Parkfield and the existence of low friction, talc-bearing, serpentinite within fault gouge has been used to explain why the SAF creeps in central California (e.g., Moore and Rymer, 2007), but it is not the only hypothesis proposed (e.g., Schleicher et al., 2010).

The surficial position of the SAF within the landscape also varies significantly over the ~120 kilometers from the Carrizo Plain to the creeping section of the fault (panel A of Figs. 4.2-4.4). In the Carrizo Plain, the SAF trace lies perpendicular to active alluvial fans and associated Quaternary alluvial deposits emanating from the Temblor Mountain range on the northeast side of the plain. Moving into the Cholame section, the fault is situated within older fluvial and marine sedimentary rocks that have been uplifted. The main SAF sits within a

narrow and elevated valley that has small drainage basins entering it. Portions of the narrow valley are closed drainage systems, but several drainages flow parallel to the fault before exiting the valley. Moving from the Cholame to Parkfield section of the San Andreas the right-lateral fault makes a ~1 km right step to the northwest. A right step in a right-lateral transform fault results in extension within the zone of step over (e.g., Sylvester, 1988). This step over has produced the ~15 kilometer long Cholame Valley. Northwest of the step over, the little Cholame Creek runs parallel to the fault on the northeast side of the valley. In several locations, stream bank erosion has cut through the fault scarp. In Parkfield, there is a prominent secondary trace of the SAF to the southwest (Southwest Fracture Zone: Fig 4.1 and Appendix B) which has slipped in historical ~M6 Parkfield earthquakes (e.g., Rymer et al., 2006). Near the hamlet of Parkfield, CA the SAF transitions from cutting through low and flat lying alluvial and fluvial terraces and cuts through a ridge known as Middle Mountain. The SAFOD drilling observatory is located on the northwest side of this ridge, while the fault tends to cut through the sedimentary rocks and landslides just to the northeast of the ridge crest. Finally, the geomorphology of the southeastern creeping section of the fault is similar to the Cholame section where the fault sits within a narrow and elevated fault-parallel valley.

To further characterize the fault's situation in the landscape an elevation profile was extracted from a 30 meter Shuttle Radar Topography Mission (SRTM) DEM and plotted in panel B of Figs. 4.2-4.4. This profile shows that the surface expression of the SAF varies from a low of ~400 meters above sea level

in the Cholame Valley step over to highs of ~800 meters in the Creeping and Cholame sections of the fault. While the elevations are similar in the Cholame and Creeping sections of the fault the wavelength of topographic change on Middle Mountain and to the northwest is much shorter and has higher amplitude, whereas the Cholame section can be characterized as a broader topographic high.

Tracking with topography and latitude are changes in mean annual precipitation (PRISM Climate Group, 2006). The driest area of the central SAF is the Carrizo Plain (~22 cm/yr of annual precipitation) and the wettest is the Creeping section with nearly three times the annual rainfall (panel B, Figures 4.2-4.4). Over the ~120 kilometers between these sections of the fault mean annual precipitation increases gradually to the northwest with locally lower values experienced in areas of lower elevation.

SCARP MAPPING METHODOLOGY

Mapping fault scarps remotely is a subjective, iterative, and highly interpretive process. For this study, I constructed a geographic information system (GIS) and mapped fault scarps along both what I interpreted to be the main SAF trace as well other secondary, but prominent fault scarps that I could clearly identify using the iterative method described below. For the quantitative portion of this fault scarp array analysis I only analyzed the scarps which were classified as part of the main SAF trace. Secondary fault traces were identified as having significant separation (usually greater than 400 meters) from the main SAF and a contiguous alignment of their own set of fault scarps. All of the mapped

secondary fault traces were observed over the Carrizo and Cholame sections of the fault (Figs. 4.5-4.8). There exist prominent secondary traces to the northwest of the Cholame section (e.g. Fig. 4.1), however they have wider separation from the main SAF and are not part of the B4 data set (white lines, panel A., Figs. 4.2-4.4). The reason that quantitative analysis of the secondary traces was not conducted is because the mapping does not include all secondary fault traces. Comprehensive strip mapping by Vedder and Wallace, (1970) was shown to result in more mapped fault traces than similar LiDAR mapping done by Arrowsmith and Zielke (2009) in the Cholame section. Therefore, here I only use the locations of secondary traces to inform interpretations about the variations in the complexity of the main fault trace.

To identify and map the locations of fault scarps I used B4 LiDAR-derived digital hillshade models and the combined imaging tool of a 35% transparent aspect map with an underlying slope map (e.g., Fig. 4.5). The DEMs required to produce these products were processed by www.opentopography.org. 0.5 meter DEMs were constructed from LiDAR point clouds using an inverse distance weighted algorithm (IDW) with a search radius of 1.5 meters. Over most of the central SAF the vegetation consists primarily of only grasses and small shrubs so DEMS were constructed using the entire point cloud. However, from the northern Parkfield section and into the Creeping section there is significant tree cover. Over this stretch, DEMs were constructed using z-minimum point returns. This is a crude way of removing vegetation, but it is necessary to have an

un-obscured view of the fault and unfortunately the B4 data point could was not formally classified as canopy and ground returns.

Hillshade, aspect, and slope maps each provide their own clues as to the location of the surface traces of faults and their scarps. Digital hillshade models provide a simulated view of the landscape with a specified sun angle to model shadows and provide realism to the imagery. Thus, the hillshade is a valuable qualitative tool for identifying tectonic geomorphic features resulting from strike slip motion such as channels that are offset, linear ridges, sag ponds, etc. (e.g., Figs. 4.5-4.11). Aspect maps can be useful for identifying the precise location of fault traces because faults often lay within linear valleys, along hillside benches, or narrow troughs. Where they do, it can be presumed that sharp linear changes in aspect which are sub-parallel to the regional trend of the SAF represent the precise surface expression of that fault. The formation of a fault scarp produces semi-linear topographic breaks with steep slopes. Therefore, slope maps are ideal for identifying the precise location of fault scarps. I placed the locations of fault trace lines along the base of the steepest portion of each fault scarp's slope, above the subdued topography of the scarp-derived colluvium.

A caveat to this fault scarp mapping is that the digital polyline GIS that I produced could more precisely be referred to as a map of fault breaks rather than only fault scarps. This is because not all fault trace features are topographic scarps from vertical displacements (e.g., linear troughs). That being said, the main point of this analysis was to characterize the continuity and complexity of these fault breaks including their separation, orientation, and lengths. However most of these

fault breaks do include portions which would accurately be described as scarps and, I use each break's mean slope to characterize its relative morphology which is why I refer to the analysis as fault scarp array geometric complexity throughout this paper. Finally, while the exact results of this mapping are a product of my own mapping style, that style is internally consistent, and the relative differences exposed between the sections of the central SAF should be considered robust.

EXTRACTING SCARP GEOMETRY AND MORPHOLOGY METRICS

Six metrics are presented visually herein (Figs. 4.2-4.4) to describe variations in the geometry and morphology of the mapped fault scarps along the central SAF: local SAF trend (Fig. 4.2C), the difference between local SAF trend and individual fault scarp orientation (Fig. 4.2D), scarp step over width (Fig 4.3C), SAF trace gaps (Fig. 4.3D), the ratio of total scarp length per kilometer of the SAF (Fig 4.4C), and mean scarp slope (Fig 4.4D). The extraction methods are described below. Following visual inspection of the spatial distribution of these metrics a summary table was produced (Table 4.1). This table divides the central SAF into seven segments based upon differences in scarp array complexity.

The local SAF trend (Fig. 4.2C) was estimated and assigned to the starting position of each mapped fault scarp. It was calculated across a distance of twenty fault scarps (between the endpoint of the 10^{th} scarp to the northwest and starting point of the 10^{th} scarp to the southeast) and the value was assigned to the middle scarp within this 20 scarp array (Fig. 4.6A).

The orientation of individual scarps was calculated as the trend between the starting and ending vertex for that line. This orientation was subtracted from the local SAF trend to calculate the difference between the local trend and each individual scarp. This difference was assigned to the starting coordinate of each scarp and plotted in Fig. 4.2D.

Scarp step over width (Fig 4.3C) was measured normal to the local SAF trend from the end point of one scarp and the starting point of the next scarp. This was calculated by finding the length of the hypotenuse and the angle between the local SAF trend and the hypotenuse's trend (shown in Fig 4.6 A) and then solving the simple trigonometric function: *Step Hypotenuse * Sin* (Θ_{SAF} - Θ_{Step}) = *Step over width.*

SAF trace gaps are simply areas along the trend of the SAF where no fault scarps are found across the width of the main SAF. Where these exist, the length of the gap was assigned to the position of the ending point of the previous scarp and plotted on Fig. 4.3D.

The ratio of scarp length per kilometer of the SAF was calculated by binning the length of scarps which exist over each one kilometer increment of the 122 kilometers of the SAF that was mapped. The metric was plotted at the midpoint of each bin (Fig 4.4C).

I measured mean scarp slope using ArcGIS focal statistics over the slope map pixels that cross the individual mapped fault scarps. The slope of each scarp is plotted at the SAF distance corresponding to the starting vertex for each scarp line (Fig. 4.4D). This analysis is somewhat simplified because, as stated earlier,

not all lengths of these polylines can be precisely defined as a scarp. For instance, mapped sections of fault traces that lie within linear troughs will measure the slope of that trough rather than the slope of a scarp. Additionally, the measurement provides only the maximum fault scarp slope, without information about the landscape's broader morphology.

RESULTS

Six hundred and sixteen individual fault scarp traces were identified along the 122 kilometers that were mapped (Table 4.1). This is an average of five individual traces per kilometer of fault. The average length of each fault scarp is 241 meters indicating that there is 1.2 kilometers of fault scarp length for each kilometer of the SAF, a 20% overlap. Much of this overlap is due to en echelon patterns of fault scarps that are common to strike slip faults (e.g., Figs. 4.5-4.11: e.g., Sylvester, 1988; Aydin and Schultz, 1990). On average the step over width between fault scarps is 74 meters. The average trend of the SAF is 323 degrees. Two hundred and thirty two of the mapped fault scarps cut through Quaternary alluvial cover. These scarps have lower slopes than the scarps which cut through older and more consolidated rocks (Table 4.1). Additionally, scarps within alluvium display shorter scarp lengths, shorter scarp step over widths, and less difference between individual scarp trends and the trend of the main SAF. That is to say, scarp geometrical arrays cutting though active surfaces are simpler.

Fourteen kilometers of the Carrizo Plain section of the SAF were mapped (Fig. 4.2-4.5 and Table 4.1) revealing 60 scarps along the main SAF and a

prominent secondary trace that displays evidence of Quaternary slip (Fig. 4.5). Over this section of the fault there are 4.3 scarps per kilometer with an average length of 258 meters. This indicates 1.1 kilometers of fault scarp length per kilometer of the SAF (10% overlap: Fig. 4.4C). The average scarp step over width is very small (16 meters Fig 4.3C and Table 4.1) resulting from very little difference between the orientation of individual scarps and the local SAF trend (4 degrees; Fig. 4.2D). Additionally, the mean trend of the SAF across the Carrizo is 321 degrees with a standard deviation of only 1 degree.

Collectively the fault scarps along the main SAF in the Carrizo plain display the simplest geometry of those observed along the entire the central SAF. Moving northwest, the end of the mapped segment of fault array simplicity roughly coincides with the beginning of the Cholame section of the SAF (e.g., Field et al., 2008). However, the amount of fault scarp geometrical complexity along the Cholame section of the SAF is not uniform. In both the southeast and northwest portions of the Cholame section the array of SAF fault scarps display a high level of complexity and between these two areas is an array of geometrical simplicity (Table 4.1 and Figs. 4.2-4.4).

Just northwest of the Carrizo Plain there is a ~28 kilometer segment of the SAF with 5.7 fault scarps per kilometer. These scarps are oriented more obliquely to the SAF trend as the scarps along the Carrizo. Additionally, they have greater slopes and six times the scarp step over width. The ratio of fault scarp length per kilometer of SAF is nearly 1.6 (59% overlap). An example of this landscape, the scarp mapping, and a cross section interpreting this complex reach of the SAF are

provided in Fig 4.6. Additional examples of mapping interpretations within this segment are provided in Arrowsmith and Zielke, (2009).

Northwest of that complex segment are 14 kilometers where the array of fault scarps displays much less geometric complexity. Over this segment of the fault there is less than one kilometer of fault scarp length per every kilometer of SAF. This may be partially due to the presence of a road that parallels the fault and obscures mapping interpretation (Fig 4.7). Despite the presence of gaps in the array of fault scarps (Fig. 4.3D) this reach of the fault has smaller step over widths and is straighter than the segment to the southeast.

In the northwest portion of the Cholame section there are many paired and parallel fault scarps (Fig 4.8). Thus, this 14 kilometer segment of the fault has large step over widths and nearly 2 kilometers of fault scarp length per kilometer along the SAF. Individual fault scarp lengths over this segment are the longest observed on the central SAF (averaging 311 meters). However, on average, these scarps are oriented nearly 8 degrees from the SAF trend.

The southern end of the Cholame Valley step over (Fig. 4.9) is commonly considered the boundary between the Cholame and Parkfield sections of the fault (e.g., Field et al., 2008). However, the complexity of the array of fault scarps across this step over suggests that they dynamics of fault slip over is different than to the southeast and northwest and thus, it is considered a separate segment. The step over is approximately 1kilometer in width and 15 kilometers in length. Across the step over there is a significant gap in the mapped surface trace of the fault. However, the arrangement of channels across this step over suggests that

fault slip does have an observable impact on the land surface (Fig. 4.9). As a result of the step over, the SAF trend is highly variable (Fig. 4.2C), step over widths are large, and scarp lengths are short (Table 4.1).

Northwest of the Cholame Valley step over, the fault displays a relatively simple geometric array of fault scarps for 14 kilometers (Table 4.1). Here the number of scarps per kilometer of the SAF is similar to the Carrizo Plain and fault scarp length is nearly the central SAF average. Additionally, there is little variation in the SAF trend and there is little difference between scarp orientations and the local fault trend (Fig. 4.10). Despite this section of the fault being situated primarily within Quaternary alluvium and across flat lying fluvial terraces, the average scarp slopes are among the highest observed across the central SAF.

The portion of the central SAF with the greatest average fault scarp slopes is the reach of the fault from Middle Mountain into the Creeping section (Table 4.1 and Fig 4.4D). This stretch of the SAF also displays a large number of gaps in the fault scarp trace (Fig 4.3D), large step over widths (Fig 4.3C), and significant variations in scarp and SAF trend (Fig 4.2C-D). According to the WGCEP the boundary between the Parkfield and creeping sections occurs over this 21 kilometers of the SAF. However, fault scarp arrays show no evidence for this boundary.

DISCUSSION AND IMPLICATIONS

Scarp Slope and Fault Activity

Along the central SAF the steepest fault scarps are not generally found within unconsolidated alluvium. This is an expected result because these conditions are typically transport limited. Whereas scarps within more consolidated lithology may be production limited and therefore their morphology would evolve over a longer time span (e.g., Hanks et al., 1984). However, some of the steepest fault scarps revealed in this analysis are located where the SAF cuts through fluvial terrace sediments along the Parkfield section (Table 4.1). Indeed, average fault scarp slope increases across the central SAF to the northwest (Fig. 4.4D). This increase in scarp slope occurs despite the fact that precipitation, vegetation, and elevation also increase to the northwest. All of these factors influence diffusivity (e.g., Hanks, 2000). Apparently, the rate of fault scarp refreshment from aseismic fault creep and surface slip from moderate magnitude earthquakes is great enough for these scarps to be steeper than those observed where large earthquakes are the dominant mode of slip release, but have not occurred since 1857. This result is noteworthy because it supports the postulation that no other slip release mechanisms (other than aseismic creep and moderate magnitude earthquakes) are necessary to explain the record of deformation expressed in the tectonic geomorphology and paleoseismology along the Parkfield section of the SAF (Toké et al., 2011).

Paleoseismic Implications

It is well known that the Carrizo Plain is one of the straightest sections of the SAF (e.g., Moore and Byerlee, 1990) and contains exemplar tectonic geomorphology. This portion of the fault has provided fruitful investigations of earthquake geology (e.g., Akciz et al., 2010, Zielke et al., 2010; Liu-Zeng, 2006; Grant and Sieh, 1994; Grant and Sieh, 1993, Sieh and Jahns, 1984; and Sieh, 1978), presumably because of its favorable geomorphic context and geometric simplicity. However, it is important to note that this mapping analysis shows evidence for Holocene activity along secondary traces in the Carrizo Plain (e.g., Fig. 4.5C which shows an active trace near the Bidart Fan site). Future studies of earthquake geology within the Carrizo might strive to characterize the relationship between these structures and the main SAF in recent paleoearthquakes. If these structures are only activated during some Carrizo ruptures, then their deformation records could be simpler to interpret and they may provide additional constraints on the timing of paleoearthquakes.

Analyses of fault scarp complexity to the northwest of the Carrizo Plain indicates that constructing complete slip rate or paleoseismic records from a single site may be challenging over two of the three segments along the Cholame section of the fault. This is because the width of the active fault zone in the two complex segments is wide. However, an alternative view is that more distributed deformation along potential sites, like those identified in Fig. 4.6, could make paleoseismic interpretation easier because there may be multiple lines of evidence

for past earthquakes at the same latitude along the fault. This could increase the confidence of interpretation and perhaps of radiocarbon ages.

Previous paleoseismic analyses along the Cholame section of the SAF have been at the LY4 site (panel A on Figs. 4.2-4.4: Young et al., 2002 and Stone et al., 2002) which is located within one of the more complex segments of the central SAF (e.g., Figs. 4.2-4.4). Because of its position within this zone of complexity it is not surprising that Young et al. (2002) noted only ~3 meters of slip from the 1857 earthquake across a single trace of the SAF when larger offsets were observed to the northwest and southeast. Additional slip in 1857 may have been distributed among the array of structures over this section of the fault (e.g., Fig. 4.6), or perhaps slip release was lower. These mapping results indicate the importance of considering the many subsidiary faults across the Cholame section of the SAF and elsewhere in future paleoseismic studies.

Geometrical Complexity and Fault Segmentation

Regardless of the relative role that subsidiary faults play in releasing plate boundary slip, the analyses in this study indicate that the interaction of subsidiary faults with the main SAF plays a large role in controlling the complexity of the primary fault zone, as expressed by fault scarp array geometry (Fig. 4.12). From the partially-mapped Carrizo Plain to the creeping section, the SAF can be grouped into seven segments based upon changing characteristics of fault scarp array geometry. These segments vary in length from 14 to 28 kilometers (Table 4.1). While some metrics corresponding to fault scarp complexity are related to

changes in lithology (e.g., scarp slope), a first order observation about the location of the boundaries between these segments is that they correspond to the positions where active subsidiary faults splay into or away from the main SAF. It is not a new result that fault interaction is an important factor in the geometry of strike-slip faults (e.g., Aydin and Shultz, 1990). However, the observations of significant fault interaction as expressed by fault scarps, which are a product of displacements due to past earthquakes, indicate that these structures are important to consider for understanding the earthquake geology and rupture hazard of the central SAF.

The wavelength of interaction between secondary faults and the central SAF is on the order of 14-28 kilometers. This along-strike segmentation length is a good approximation of the seismogenic depth of the crust in central California (e.g., Hill et al., 1990). The length scale of fault trace segmentation in strike-slip earthquake ruptures has been shown to reach a maximum of ~18 kilometers (Klinger, 2010). Klinger also demonstrated that this is in close correlation to seismic source inversions which indicate that large strike slip earthquakes slip in patches with a maximum along-strike length of ~25 kilometers. Thus, the segmentation mapping presented here and the wavelength of subsidiary fault interaction along the central SAF supports the inference that the length-scale of segmentation along strike-slip faults scales with the thickness of the seismogenic crust.

CONCLUSIONS AND RECOMMENDATIONS

The central SAF can be divided into at least seven segments based upon the complexity of fault scarp array geometry. This measure of segmentation is a shorter length scale than the fault sections considered by the Working Group on California Earthquake Probabilities and should be considered in future integrations of paleoseismic data. Fault segmentation along major strike slip faults such as the SAF is controlled by the wavelength of interaction with nearby secondary structures and this wavelength appears to scale with the depth of the seismogenic crust. To explore this further, the entire SAF should be similarly mapped and correlations between seismogenic depths and segmentation can be more rigorously tested.

These types of remote LiDAR-based fault scarp reconnaissance and complexity analyses should be useful for paleoseismic siting (Appendix H), interpretations of paleoseismic results, and for considering revisions to fault zone regulations (e.g., Hart and Bryant, 1997; Chapter 2). Ideally, they should not be done without the accompaniment of field analyses. However as demonstrated here, first order relationships about the role of fault interactions and the relative rates of geomorphic and tectonic processes can be deduced over a large region in much less time than is required for a similarly comprehensive field analysis (if this is at all possible).

Future analyses should include characterizing the array complexity and morphology of the nearby subsidiary faults by expanding mapping to include previous fault scarp interpretations (e.g., Vedder and Wallace, 1970; Stone et al.,

2002; and Arrowsmith and Zielke, 2009). Scarp morphology metrics should be improved to consider scarp curvature which may help elucidate the nature of fault interactions with the main SAF and relative rates of activity. Such analyses will require additional mapping of these more subdued and discontinuous features with multiple iterations and the aide of existing mapping such as Vedder and Wallace, (1970).

ACKNOWLEDGEMENTS

I thank D. Haddad for motivational discussions about characterizing scarp morphology using LiDAR data. This research would not have been possible without the southern San Andreas Fault and San Jacinto B4 ALSM survey which was collected by Ohio State University, the US Geological Survey, NCALM, and UNAVCO (www.earthsciences.osu.edu/b4). Digital elevation models derived from the B4 point cloud were processed by the OpenTopography Facility (www.opentopography.org) with support from the National Science Foundation under NSF Award Numbers 0930731 & 0930643.

REFERENCES CITED

Akciz, S.O., Grant-Ludwig, L., Arrowsmith, J R., and Zielke, O., 2010, Century-long average time intervals between earthquake ruptures of the San Andreas fault in the Carrizo Plain, California: Geology, v. 38, no. 9, p. 787-790, doi:10.1130/G30995.1.

Allen, C. R., 1968, The tectonic environments of seismically active and inactive areas along the San Andreas fault system, in Proc. of the Conference on Geologic Problems of San Andreas Fault System, W. R. Dickinson and A. Grantz (editors): Stanford University Publications, Vol. 11, Palo Alto, California, 70–82.

Arrowsmith J R., McNally, K., and Davis, J., 1997, Potential for earthquake rupture and M 7 earthquakes along the Parkfield, Cholame, and Carrizo segments of the San Andreas Fault: Seismological Research Letters, v. 68, p. 902-916.

Arrowsmith, J R., Rhodes, D.D., and Pollard, D.D., 1998, Morphologic dating of scarps formed by repeated slip events along the San Andreas Fault, Carrizo Plain, California: Journal of Geophysical Research, v. 103, no. B5, p. 10,141-10,160.

Arrowsmith, J R., Zielke, O., 2009, Tectonic geomorphology of the San Andreas Fault zone from high resolution topography: An example from the Cholame segment: Geomorphology, v. 113, p. 70-81.

Aydin, A. and Schultz, R.A., 1990, Effect of mechanical interaction on the development of strike-slip faults with echelon patterns, Journal of Structural Geology, v. 12, no. 1, p. 123-129.

Bevis, M., Hudnut, K., Sanchez, R., Toth, C., Grejner-Brzezinska, D., Kendrick, E., Caccamise, D., Raleigh, D., Zhou, H., Shan, S., Shindle, W., Yong, A., Harvey, J., Borsa, A., Ayoub, F., Elliot, B., Shrestha, R., Carter, B., Sartori, M., Phillips, D., Coloma, F., Stark, K., 2005, The B4Project: scanning the San Andreas and San Jacinto fault zones: Eos Transactions AGU, v. 86, no. 52, Fall Meeting Supplemental, Abstract H34B-01.

Bradbury, K.K,, Barton, D.C., Solum, J.G., Draper, S.D., and Evans, J.P., 2007, Mineralogic and textural analyses of drill cuttings from the San Andreas Fault Observatory at Depth (SAFOD) boreholes: Initial interpretations of fault zone composition and constraints on geologic models: Geosphere, v. 3, p. 299-318, doi: 10.1130/GES00076.1.

Burbank, D.W., and Anderson, R.S., 2001, Tectonic Geomorphology: Malden MA, Blackwell Publishing, 274 p.

Crosby, C.J., 2004, Digital database of faulting accompanying the 1966 Parkfield, California earthquake: U.S. Geological Survey Open-File Report 2004-1437.

DeLong, S.B., Hilley, G.E., Rymer, M.J., and Prentice C., 2010, Fault zone structure from topography: Signatures of en echelon fault slip at Mustang Ridge on the San Andreas Fault, Monterey County, California: Tectonics, v. 29, 16 p., doi:10.1029/2010TC002673.

Dibblee, T. W., 1973, Regional geologic map of the San Andreas and related faults in Carrizo Plain, Temblor, Caliente, and La Panza ranges and vicinity, California, United States Geological Survey Miscellaneous Geologic Investigations Map I-757.

Field, E.H., Dawson, T.E., Felzer, K.R., Frankel, A.D., Gupta, V., Jordan, T.H., Parsons, T., Petersen, M.D., Stein, R.S., Weldon II, R.J., and Wills, C.J., 2008, Uniform California Earthquake Rupture Forecast, Version 2 (UCERF 2): US Geological Survey Open-File Report 2007-1437, 104 p., http://pubs.usgs.gov/of/2007/1437/.

Grant, L.B. and Sieh, K., 1993, Stratigraphic Evidence for Seven Meters of Dextral Slip on the San Andreas Fault During the 1857 Earthquake in the Carrizo Plain: Bulletin of the Seismological Society of America, v. 83, no. 3, p. 619-635.

Grant, L.B. and Sieh, K., 1994, Paleoseismic evidence of clustered earthquakes on the San Andreas fault in the Carrizo Plain, California: Journal of Geophysical Research, v. 99, no. B4, p. 6819-6841.

Hanks, T.C., Bucknam, R.C., Lajoie, K.R., and Wallace, R.E., 1984, Modification of wave-curt and fault-controlled landforms: Journal of Geophysical Research, v. 89, p. 5771-5790, doi: 10.1029/JB089iB07p05771.

Hanks, T.C., 2000, The Age of Scarplike Landforms from Diffusion-Equation Analysis, in Quaternary geology: methods and applications, Noller, J.S., Sowers, J.M., and Lettis W.R. (editors): American Geophysical Union, Washington D.C., 581 p.

Hart, E.W. and Bryant, W.A., 1997, FAULT RUPTURE HAZARDS IN CALIFORNIA Alquist-Priolo Earthquake Fault Zoning Act with Index to Earthquake Fault Zone Maps: Department of Conservation, Division of Mines and Geology, Special Publication 42.

Haugerud, R.A., Harding, D.J., Johnson, S.Y., Harless, J.L.,Weaver, C.S., Sherrod, B.L., 2003, High-resolution Lidar topography of the Puget

Lowland, Washington—a bonanza for earth science: GSA Today, Geological Society of America, v. 13, no. 6, p. 4–10.

Hill, D. P., J. P. Eaton, and L. M. Jones, 1990, Seismicity, 1980–1986, in The San Andreas Fault System, California, R. E. Wallace (Editor), U.S. Geological Survey Professional Paper 1515, p. 115–151.

Hilley, G.E., Arrowsmith, JR., and Stone, E., 2001, Inferring Segment Strength Contrasts and Boundaries along Low-Friction Faults Using Surface Offset Data, with an Example from the Cholame-Carrizo Segment Boundary along the San Andreas Fault, Southern California: Bulletin of the Seismological Society of America, v. 91, no. 3, p. 427-440.

Hilley, G.E., DeLong, S., Prentice, C., Blisniuk, K., and Arrowsmith, JR., 2010, Morphologic dating of fault scarps using airborne laser swath mapping (ALSM) data: Geophysical Research Letters, v. 37, L04301, doi: 10.1029/2009GL042044.

Keller, E.A. and Pinter, N., 2002, Active Tectonics: Earthquakes Uplift, and Landscape (second edition): Upper Saddle River, NJ, Prentice Hall, 362 p.

King G.C. and Nabelek, J., 1985, The role of fault bends in faults in the initiation and termination of earthquake rupture: Science, v. 228, p. 984-987, doi:10.1126/science.228.4702.984.

Klinger, Y., 2010, Relation between continental strike-slip earthquake segmentation and thickness of the crust: Journal of Geophysical Research, v. 115, B07306, doi: 10.1029/2009JB006550.

Knuepfer, P.L.K., 1989, Implication of the characteristic of end-points of historical surface ruptures for the nature of fault segmentation, U.S. Geological Survery Open File Report 89-315, 193-228.

Kondo, H., Toda, S., Okumura, K., Takada, K., and Chiba, T., 2008, A fault scarp in an urban area identified by LiDAR survey: A Case study on the Itoigawa-Shizuoka Tectonic Line, central Japan: Geomorphology, v. 101, p. 731-739.

Lawson, A.C., 1908, The California Earthquake of April 18, 1906: Report of the State Earthquake Investigation Commission. Carnegie Institution of Washington, pub. 87, Washington D.C.

Lienkaemper, J.J. and Prescott W.H., 1989, Historic Surface Slip along the San Andreas Fault near Parkfield California: Journal of Geophysical Research, v. 94, p. 17647-17670.

Lienkaemper, J.J., and Strum, T.A., 1989, Reconstruction of a Channel Offset in 1857(?) by the San Andreas Fault near Cholame, California: Bulletin of the Seismological Society of America, v. 79, no. 3, p. 901-909.

Lienkaemper J.L., 2001, 1857 Slip on the San Andreas Fault Southeast of Cholame, California: Bulletin of the Seismological Society of America, v. 91, no. 6, p. 1659-1672.

Lienkaemper, J. J., Baker B., and McFarland F. S., 2006, Surface slip associated with the 2004 Parkfield California, earthquake measured on alignment arrays: Bulletin of the Seismological Society of America, v. 96, no. 4B, p. S239–S249, doi: 10.1785/0120050806

Lisowski, M. and Prescott, W.H., 1981, Short-Range Distance Measurements Along the San Andreas Fault System in Central California, 1975 to 1979: Bulletin of the Seismological Society of America, v. 71, no. 5, p. 1607-1624.

Liu-Zeng, J., Klinger, Y., Sieh, K., Rubin C., and Seitz, G., 2006, Serial ruptures of the San Andreas fault, Carrizo Plain, California, revealed by three-dimensional excavations: Journal of Geophysical Research, v. 111, B02306, 33 p., doi:10.1029/2004JB003601.

Ludington S., Moring, B.C., Miller, R.J., Flynn, K.S., Sonte, P.A., Bedford, D.R., 2005, Preliminary integrated databases for the United States (GIS shape files of Geology): U.S. Geological Survey Open-File Report 2005-1305.

Machette, M.N., Personius, S.F., Nelson, A.R., Schwartz, D. P., and Lund, W.R., 1991, The Wasatch fault zone, Utah – segmentation and history of Holocene earthquakes: Journal of Structural Geology, v. 13, no.2, p. 137-149.

Marzocchi, W. and Zechar, J.D., 2011, Earthquake Forecasting and Earthquake Prediction: Different Approaches for Obtaining the Best Model: Seismological Research Letters, v. 82, no. 3, p. 442-448.

McCalpin, J. (editor), 1996, Paleoseismology: San Diego, CA, Academic Press, 588 p.

Meade, B.J. and Hager B.H., 2005, Block models of crustal motion in southern California constrained by GPS measurements: Journal of Geophysical Research, v. 110, B03403, doi:10.1029/2004JB003209

Moore, D.E. and Byerlee, J.D., 1991, Comparative geometry of the San Andreas fault, California, and laboratory fault zones: Geological Society of America Bulletin, v. 103, p. 762-774.

Moore, D.E. and Rymer, M.J., 2007, Talc-bearing serpentinite and the creeping section of the San Andreas Fault: Nature, v. 448, p. 795-797, doi:10.1038/448756a.

Murray, J., and Langbein, J., 2006, Slip on the San Andreas fault at Parkfield over two earthquake cycles and the implications for seismic hazard: Bulletin of the Seismological Society of America, v. 96, no 4b, S283-S303.

Nash, D.B., 1984, Morphologic dating of fluvial terrace scarps and fault scarps near West Yellowstone, Montana, Geological Society of America Bulletin, v. 95, p. 1413-1424.

Oskin, M.E., Le K., and Strane, M.D., 2007, Quantifying fault-zone activity in arid environments with high-resolution topography: Geophysical Research Letters, v. 34, L23S05, doi:10.1029/2007GL031295.

PRISM Climate Group, 2006, United States Average Annual Precipitation, 1971-2000 raster digital data: Corvallis, Oregon, PRISM Climate Group at Oregon State University.

Rymer, M.J., Tinsley, J.C., Treiman, J.A., Arrowsmith, J R., Clahan, K.B., Rosinski, A.M., Bryant, W.A., Snyder, A., Fuis, G.S., Toké, N.A., and Bawden G. W., 2006, Surface Fault Slip Associated with the 2004 Parkfield, California Earthquake: Bulletin of the Seismological Society of America, v. 96, no. 4b, S11-S27.

Schleicher, A.M., van der Pluijm, B.A., and Warr, L.N., 2010, Nanocoatings of clay and creep of the San Andreas fault at Parkfield, California: Geology, v. 38, no. 7, p. 667-670, doi: 10.1130/G31091.1.

Schmalzle, G., Dixon,T., Malservisi, R., and Govers, R., 2006, Strain accumulation across the Carrizo segment of the San Andrea Fault, California: Impact of laterally varying crustal properties: Journal of Geophysical Research, v. 111, B05403, doi: 10.1029/2005JB003843.

Schwartz, D.P. and Coppersmith, K.J., 1984, Fault behavior and characteristic earthquakes: Examples from the Wasatch and San Andreas fault zones: Journal of Geophysical Research, v. 89, p. 5681-5698.

Sherrod, B.L., Brocher, T.M., Weaver, C.S., Bucknam, R.C., Blakely, R.J., Kelsey, H.M., Nelson, A. R., and Haugerud, R., 2004, Holocene fault scarps near Tacoma, Washington, USA: Geology, v. 34, no. 1, p. 9-12.

Sieh, K.E., 1978, Slip along the San Andreas Fault Associated with the Great 1857 Earthquake: Bulletin of the Seismological Society of America, v. 68, no. 5, p. 1421-1448.

Sieh, K.E. and Jahns R.H., 1984, Holocene activity of the San Andreas fault at Wallace Creek, California: Geological Society of America Bulletin v. 95, p. 883-896.

Sims, J. D., 1987, Late Holocene slip rate along the San Andreas Fault near Cholame, California: Geological Society of America, Cordilleran Section, Abstracts with Programs v. 83, p. 451.

Stewart, S. and Hancock, P.L., 1990, What is a fault scarp?: Episodes, v. 13, no. 4, p. 256-263.

Stone, E.M., Grant, L.B., and Arrowsmith J R., 2002, Recent Rupture History of the San Andreas Fault Southeast of Cholame in the Northern Carrizo Plain, California: Bulletin of the Seismological Society of America, v. 92, no.3, p. 983-997.

Sylvester, A.G., 1988, Strike-slip faults: GSA Bulletin, v. 100, p. 1666-1703.

Thayer, M., 2006, Structural Geology of the San Andreas Fault Zone at Middle Mountain, near Parkfield, Central California: M.S. Thesis Arizona State University, 124 p.

Titus, S.J., C. DeMets, and Tikoff B., 2006, Thirty-five-year creep rates for the creeping segment of the San Andreas fault and the effects of the 2004 Parkfield earthquake: constraints from alignment arrays, continuous GPS, and creepmeters: Bulletin of the Seismological Society of America, v. 96, no. 4B, p. S250-S268 doi: 10.1785/0120050811.

Titus, S.J., Dyson, M., DeMets, C., Tikoff, B., Rolandone, F., and Burgmann, R., 2011, Geologic versus geodetic deformation adjacent to the San Andreas fault, central California: Geological Society of America Bulletin, v. 123, p. 794-820, doi: 10.1130/B30150.1.

Toké, N.A., and Arrowsmith, J R., 2006, Reassessment of the Slip Budget along the Parkfield Segment of the San Andreas Fault: Bulletin of the Seismological Society of America, v. 96, no. 4b, S339-348.

Toké, N.A., Arrowsmith, J R., Rymer, M.J., Landgraf, A., Haddad, D.E., Busch, M., Coyan, J., and Hannah, A., 2011, Late Holocene slip rate of the San Andreas fault and its accommodation by creep and moderate magnitude earthquakes at Parkfield, California: Geology, v. 39, no. 3, p. 243-246, doi: 10.1130/G31498.1.

Toth, C. Brzezinski D., SANYO, N., Parka, E., and Yeastily, N., 2007, LiDAR Mapping Supporting Earthquake Research of the San Andreas Fault: ASPRS 2007 Annual Conference Tampa, Florida May 7-11, 11 p.

U.S. Geological Survey, 2006, Quaternary fault and fold database for the United States, Last accessed October 2010: http//earthquakes.usgs.gov/hazards/qfaults/.

Vedder, J.G., Wallace, R.E., 1970, Map showing recently active breaks along the San Andreas and related faults between Cholame valley and Tejón Pass, California: U.S. Geological Survey Miscellaneous Geologic Investigations Map 1-574, scale 1:24,000.

Wallace, R.E., 1968, Notes on stream channels offset by the San Andreas fault, southern Coast Ranges, California, in Proceedings of conference on geologic problems of San Andreas fault system, Dickinson, W. R., and Grantz, A. (editors): Stanford University Publications, v. 11, p. 6-21.

Wallace, R.E., 1973, Surface fracture patterns along the San Andreas fault, in Proceedings of the Conference on Tectonic Problems of San Andreas Fault System, R.L. Kovach and A. Nur (editors): Stanford University Publications, Palo Alto, California, 248-250.

Weldon, R.J., Fumal, T., and Biasi, G.P., 2004, Wrightwood and the earthquake cycle: What a long recurrence record tells us about how faults work: GSA Today, vo. 14, no. 9, p. 4-10.

Weldon, R.J., Fumal, T.E., Biasi, G.P., and Scharer, K.M., 2005, Past and Future Earthquakes on the San Andreas Fault: Science, v. 308, p. 966-967.

Wells, D. L., and Coppersmith, K. J., 1994, New empirical relationships among magnitude, rupture length, rupture width, rupture area, and surface displacement: Bulletin of the Seismological Society of America, v. 84, no. 4, p. 974–1002.

Wesnousky, S.G., 1988, Seismological and structural evolution of strike-slip faults: Nature, v. 335, p. 340-343.

Wesnousky, S.G., 2006, Predicting the endpoints of earthquake ruptures: Nature, v. 444, p. 358-360, doi: 10.1038/nature05275.

Young, J.J., Arrowsmith, J R., Colin, L., Grant, L.B., and Goatee, B., 2002, Three-Dimensional Excavation and Recent Rupture History along the Cholame Segment of the San Andreas Fault: Bulletin of the Seismological Society of America, v. 92, no. 7, p. 2670-2688.

Zielke, O., Arrowsmith, J R., Grant-Ludwig, L., and Akciz, S.O., 2010, Slip in the 1857 and Earlier Earthquakes along the Carrizo Plain, San Andreas Fault: Science, v. 327, no. 1119-1122. DOI: 10.1126/science.1182781.

Zoback, M., Hickman, S., and Ellsworth, W., 2010, Scientific Drilling Into the San Andreas Fault Zone: EOS, Transactions, American Geophysical Union, v. 91, no. 22, p. 197-199.

TABLE 4.1. DESCRIPTIVE STATISTICS OF FAULT SCARP MAPPING ALONG THE SAN ANDREAS FAULT

Scarp Region	n	Avg. Scarp length (m)	Avg. step width (m)	Scarps per km	Avg. SAF Trend	Avg. Trend Diff[1]	Avg. Slope (deg)
central SAF (122km)	616	241 210 (Std. Dev.)	74 87	5.05	323 7	8.6 8.1	11.7 6.7
Carrizo Plain (14km)	60	258 230	16 17	4.29	321 1	3.8 4.5	7.8 4.8
Cholame 1 (28km)	159	280 189	97 91	5.68	324 5	8.5 7.6	9.3 5.1
Cholame 2 (14km)	54	274 299	41 41	3.86	322 2	5.1 4.1	10.6 6.2
Cholame 3 (14km)	76	311 273	96 108	5.42	322 5	7.5 6.3	14.4 4.7
Cholame Valley (15km)	88	187 129	83 104	5.86	332 11	12.2 10.7	7.4 4.5
Parkfield Valley (14km)	61	231 207	47 55	4.35	320 2	6.4 5.4	14.3 7.2
Middle Mtn. to Creeping (21km)	119	163 129	83 82	5.67	319 6	12.0 8.7	17.6 6.4
Qal	232	215 181	46 72	-	325 9	7.6 8.3	9.4 6.5
Other Rock	384	257 223	92 91	-	322 6	9.2 7.9	13.1 6.5

1 – Average difference between scarp and SAF trend in degrees.

Figure 4.1. The central San Andreas Fault is positioned at the northwest extent of the B4 LiDAR data set (thick red lines; Toth, 2007). This portion of the SAF has long been considered as four fault sections (often called segments): The Creeping, Parkfield, Cholame, and Carrizo sections (WGCEP: Field et al., 2008). This study considers B4-derived mapping analyses of fault scarp geometry and morphology along ~122 km of the central SAF (the area between the yellow diamonds). Additional active faults are plotted with thin red lines (US Geological Survey, 2006). Annotation is draped over a panchromatic Landsat image modified from a B4 overview map:
(http://www.earthsciences.osu.edu/b4/Site/B4%20Overview%20Maps.html)

N
Explanation
End points for this study
B4 LiDAR
Other Quaternary Active Faults
approx. central SAF section boundaries
120 km
B4
Mission Creek Fault
Garlock Fault
San Andreas Fault
San Jacinto Fault
Los Angeles, CA
Cajon Creek
Parkfield
Cholame
Carrizo
Creeping

Figure 4.2. A) Central SAF scarp mapping underlain by an SRTM-derived 30m digital hillshade model and 1:750k geologic map (Ludington et al., 2005). For a description of geologic units see the introduction. Note the many nearby active faults (white lines: US Geological Survey, 2006). B) Distance along the central SAF mapping analysis, annual precipitation (PRISM Climate Group, 2006), mean fault zone elevation extracted from 30m SRTM digital elevation model, and aseismic creep rate from the Bidart Fan paleoseismic site to the northwest terminus of the B4 LiDAR project on the Creeping section of the fault (Lisowski and Prescott, 1981; Murray et al., 2001; Lienkaemper, 2006; Murray et al, 2006; and Toke and Arrowsmith, 2006). Additionally the locations of paleoseismic sites are plotted along the fault (0 = Bidart Fan: Akciz et al., 2010, Grant and Sieh 1994; PF = Phelan Fan: Grant and Sieh 1993; WC = Wallace Creek: Sieh and Jahns, 1984 and nearby Liu-Zeng et al., 2006; LY4 site: Young et al., 2002, Stone et al., 2002 ; WT = Water Tank site: Sims, 1987; and MF = Miller's Field site: e.g., Toke et al., 2011). C) Local SAF trend (red dots) was determined at the starting node of each individual scarp by measuring the trend over 10 fault scarps to the southeast and to the northwest of that scarp (see text and Fig. 4.6). A five measurement moving average of the SAF trend is plotted with a black line. D) Difference in degrees between the local SAF trend and individual scarp orientations. Red data points are scarp trends oriented more north than the SAF and blue points are more west. A 20 measurement moving average of the absolute difference in trend is plotted with a black line.

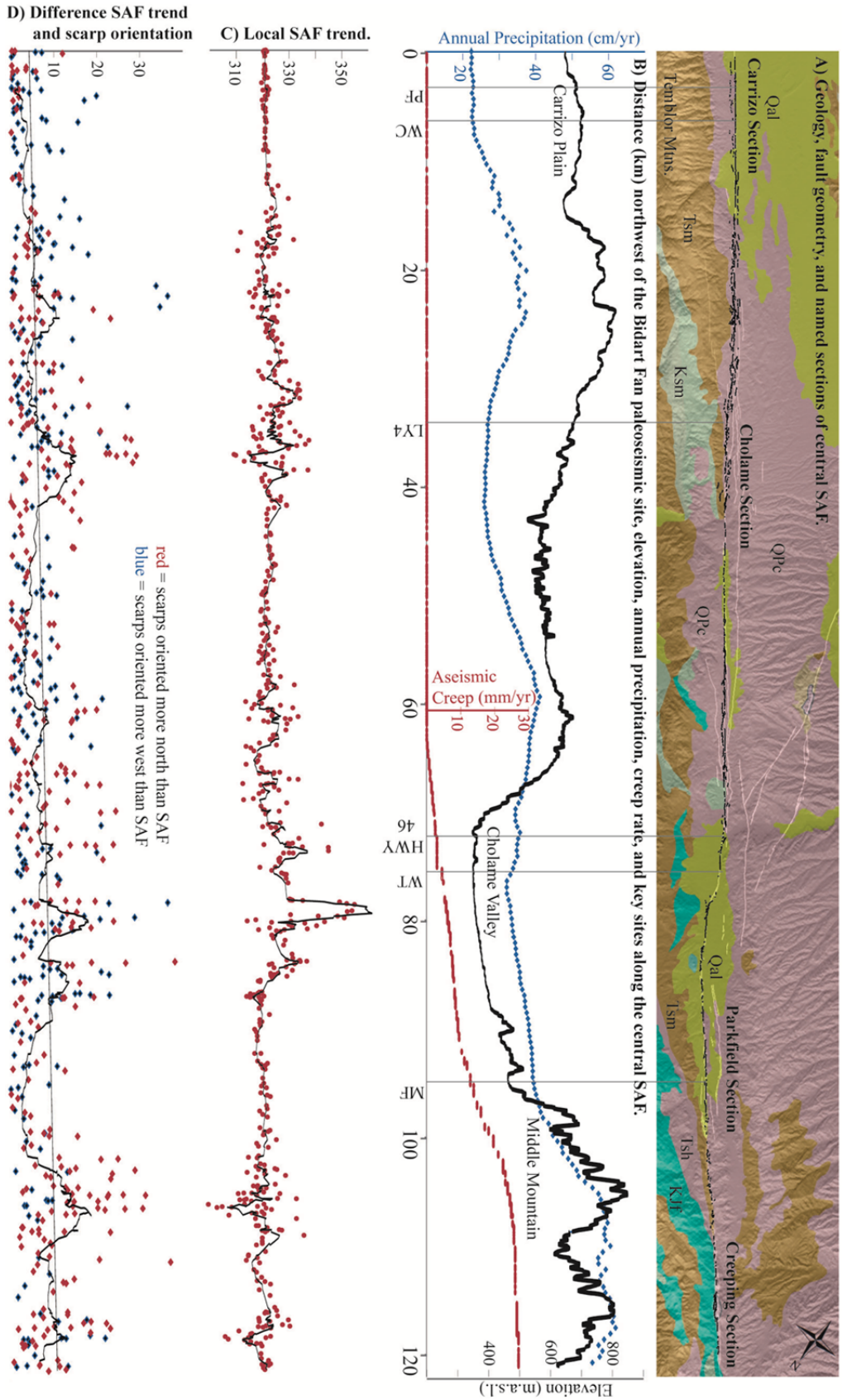
A) Geology, fault geometry, and named sections of central SAF.
Qal
Carrizo Section
Cholame Section
Parkfield Section
Creeping Section
Temblor Mtns.
Tsm
Ksm
QPc
Qal
Tsm
Tsh
Kjf
B) Distance (km) northwest of the Bidart Fan paleoseismic site, elevation, annual precipitation, creep rate, and key sites along the central SAF.
Annual Precipitation (cm/yr)
Carrizo Plain
Aseismic
Creep (mm/yr)
Cholame Valley
Middle Mountain
Elevation (m.a.s.l.)
PF
WC
LY4
46
HWY
WT
MF
C) Local SAF trend.
D) Difference SAF trend
and scarp orientation
red = scarps oriented more north than SAF
blue = scarps oriented more west than SAF

Figure 4.3. A) Central SAF scarp mapping underlain by an SRTM-derived 30m digital hillshade model and 1:750k geologic map (Ludington et al., 2005). For a description of geologic units see the introduction. Note the many nearby active faults (white lines: US Geological Survey, 2006). B) Distance along the central SAF mapping analysis, annual precipitation (PRISM Climate Group, 2006), mean fault zone elevation extracted from 30m SRTM digital elevation model, and aseismic creep rate from the Bidart Fan paleoseismic site to the northwest terminus of the B4 LiDAR project on the Creeping section of the fault (Lisowski and Prescott, 1981; Murray et al., 2001; Lienkaemper, 2006; Murray et al, 2006; and Toke and Arrowsmith, 2006). Additionally the locations of paleoseismic sites are plotted along the fault (see Fig. 4.2 caption). C) Absolute scarp step over (red points) width in meters. This was measured within the coordinate system of the local SAF trend from the endpoint of one scarp to the starting point of the next scarp. The value was assigned to the first scarp. See text for further description and Fig. 4.6 for an example of scarp ordering. A 20 scarp moving average is plotted (black line). D) The lengths of gaps along the SAF local trend where no scarps were mapped. The gap's position was assigned to the preceding scarp. While there are gaps in the prominent scarp mapping, this is not meant to imply that there is a gap in the fault (See text for explanation).

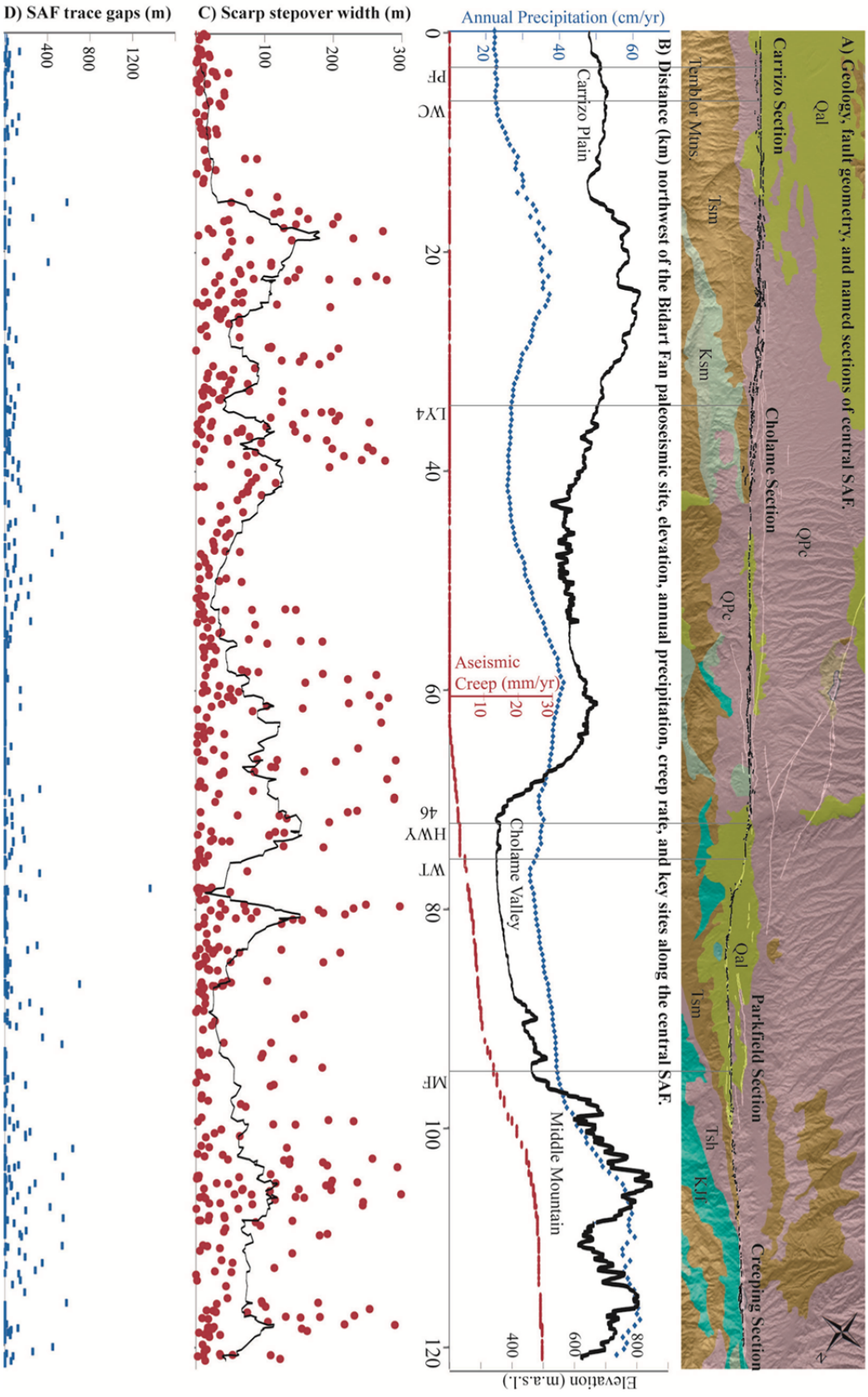
A) Geology, fault geometry, and named sections of central SAF.
Qal
QPc
Carrizo Section
Cholame Section
Parkfield Section
Creeping Section
Temblor Mtns.
Tsm
Ksm
Tsh
Kjf
B) Distance (km) northwest of the Bidart Fan paleoseismic site, elevation, annual precipitation, creep rate, and key sites along the central SAF.
Annual Precipitation (cm/yr)
Carrizo Plain
Aseismic Creep (mm/yr)
Cholame Valley
Middle Mountain
Elevation (m.a.s.l.)
PF
WC
LY4
HWY 46
WT
MF
C) Scarp stepover width (m)
D) SAF trace gaps (m)

Figure 4.4. A) Central SAF scarp mapping underlain by an SRTM-derived 30m digital hillshade model (DEM) and 1:750k geologic map (Ludington et al., 2005). For a description of geologic units see the introduction. Note the many nearby active faults (white lines: US Geological Survey, 2006). B) Distance along the central SAF mapping analysis, annual precipitation (PRISM Climate Group, 2006), mean fault zone elevation extracted from 30m SRTM digital elevation model, and aseismic creep rate from the Bidart Fan paleoseismic site to the northwest terminus of the B4 LiDAR project on the Creeping section of the fault (Lisowski and Prescott, 1981; Murray et al., 2001; Lienkaemper, 2006; Murray et al, 2006; and Toke and Arrowsmith, 2006). Additionally the locations of paleoseismic sites are plotted along the fault (see Fig. 4.2 caption). C) The ratio of mapped scarp length for each kilometer along the SAF trend. Where scarp length per kilometer is greater than 1 this indicates a complex surface expression of the fault with more than a single surface trace. Where the scarp length per kilometer is less than 1 this indicates a section of the fault with a significant proportion of scarp gaps (Fig. 4.4D). A 10 km moving average is plotted (black line). D) Mean scarp slope was extracted from B4 LiDAR DEMs using a focal statistics analysis in ArcGIS. A 20 scarp moving average is plotted (black line).

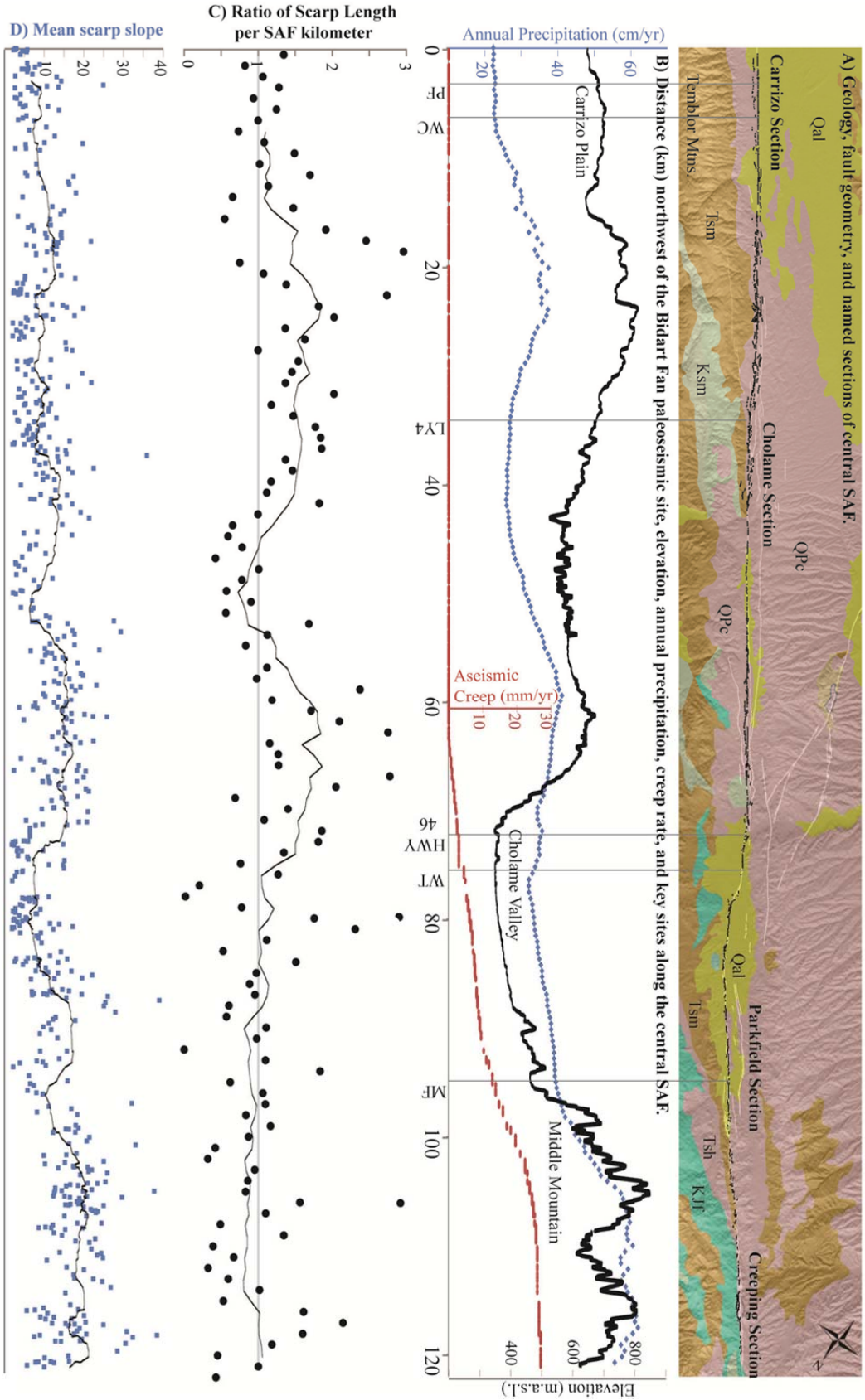
A) Geology, fault geometry, and named sections of central SAF.
Qal
QPc
Carrizo Section
Cholame Section
Parkfield Section
Creeping Section
Temblor Mtns.
Tsm
Ksm
Tsh
KJf
B) Distance (km) northwest of the Bidart Fan paleoseismic site, elevation, annual precipitation, creep rate, and key sites along the central SAF.
Annual Precipitation (cm/yr)
Carrizo Plain
Aseismic Creep (mm/yr)
Cholame Valley
Middle Mountain
Elevation (m.a.s.l.)
PF
WC
LY4
HWY 46
WT
MF
C) Ratio of Scarp Length per SAF kilometer
D) Mean scarp slope

Figure 4.5. A) 0.5 meter B4-LiDAR derived digital hillshade model 300 meters northwest of the Bidart Fan paleoseismic site along the SAF trend within the Carrizo section of the fault. This part of the fault has a geometrically simple array of fault scarps (black lines; Figs. 4.2- 4.4). B) Corresponding aspect map draped over the slope map with a 35% transparency. Examples of some of the prominent tectonically-produced landforms are highlighted with annotation. These observations were used in conjunction with the hillshade and combined aspect-slope image to map individual scarps. Only the most prominent scarps were mapped. Scarps were not considered continuous where there existed no surface evidence for them even if the next scarp along the trace was exactly aligned with the previous scarp (see uncertain dashed yellow examples in panel A). During the mapping process the locations of potential paleoseismic sites were recorded and briefly described and the locations of offset channels were recorded with a rough estimate of the displacement (black dots, some are annotated here and in Figs. 4.6-4.11). However, detailed analyses of these features (Appendix H) is not the focus of this paper's discussion. C) The combination of an optimally-oriented aspect map and slope map provides a visual aid for identifying subtle scarps such as this active secondary fault trace northwest of the main SAF. These secondary features were mapped, recorded, and are part of this paper's discussion but are not part of the scarp complexity metrics analysis (Figs. 4.2-4.4; see text for further explanation).

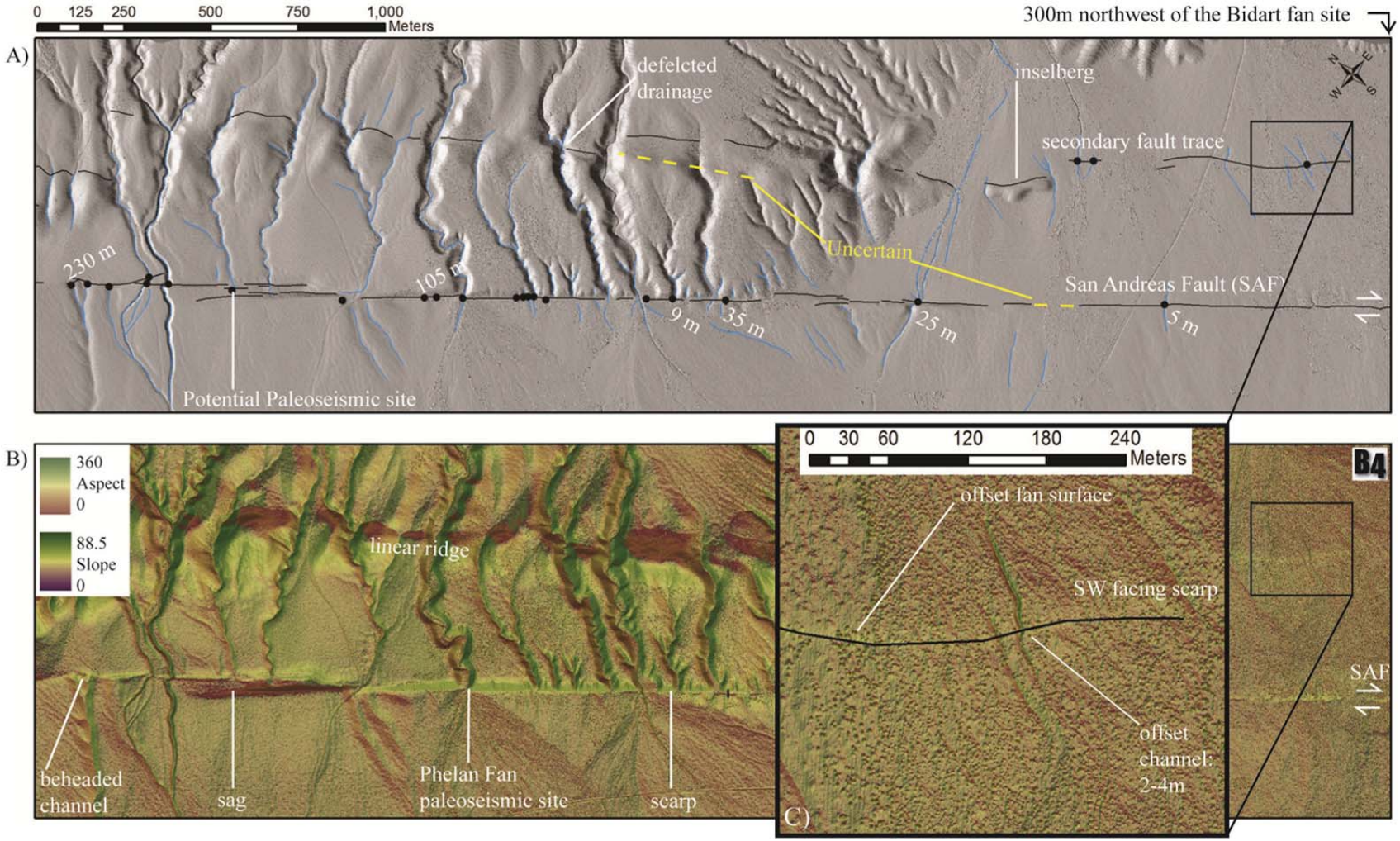
0 125 250 500 750 1,000
Meters
300m northwest of the Bidart fan site
A)
defelcted drainage
inselberg
secondary fault trace
Uncertain
San Andreas Fault (SAF)
230 m
105 m
9 m
35 m
25 m
5 m
Potential Paleoseismic site
B)
360
Aspect
0
88.5
Slope
0
linear ridge
beheaded channel
sag
Phelan Fan paleoseismic site
scarp
0 30 60 120 180 240
Meters
B4
offset fan surface
SW facing scarp
offset channel: 2-4m
SAF
C)

Figure 4.6. A) 0.5 meter B4-LiDAR derived digital hillshade model 20 kilometers northwest of the Bidart Fan paleoseismic site along the SAF trend. This portion of the fault displays a geometrically complex array of prominent fault scarps (black lines; Figs. 4.2-4.4). Using yellow annotation I provide an example of how fault scarp geometry was assessed. Starting from the southeast: Scarp step over width and length (Fig. 4.3C) are resolved by calculating the distance between the first scarp's end point and the next scarp's starting point (the hypotenuse of the step over) and then using simple trigonometry within the local coordinate system of the SAF trend (Fig. 4.2C). This coordinate system is defined as the trend between the end point of the 10^{th} scarp to the northwest and the 10^{th} scarp to the southeast. Calculating the SAF trend over a distance of 20 scarps removes the effect of individual scarp misalignments, but preserves the ability to measure changes in the overall trend. Only scarps considered to be the main trace are included in these analyses. The locations of potential paleoseismic sites are discussed in the text. B) Aspect map is draped over a slope map with 35% transparency. The local surficial geology is primarily QPc (marine sand and mudstones) with local veneers of Quaternary alluvium. C) An example of a cross sectional interpretation is provided from X to X'. Here, the active fault zone is at least as wide as the B4 LiDAR, however not all faults are considered to be the primary SAF trace because they likely merge with the main SAF > 2km below the surface and thus may not always rupture with the main trace.

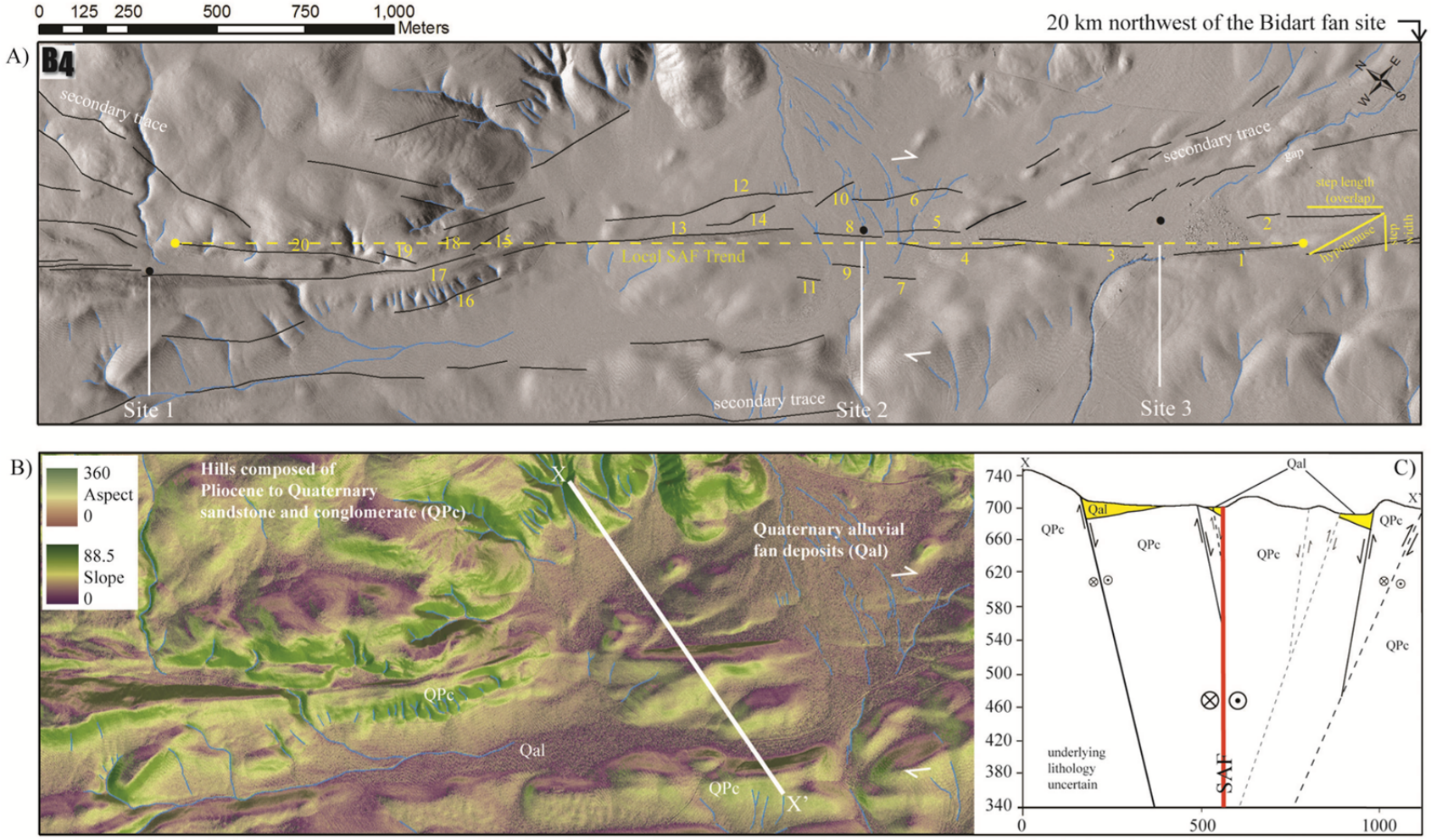
0 125 250 500 750 1,000
Meters
20 km northwest of the Bidart fan site
A)
B4
secondary trace
secondary trace
secondary trace
gap
step length (overlap)
step width
hypotenuse
Local SAF Trend
Site 1
Site 2
Site 3
B)
360
Aspect
0
88.5
Slope
0
Hills composed of Pliocene to Quaternary sandstone and conglomerate (QPc)
Quaternary alluvial fan deposits (Qal)
X
X'
QPc
Qal
C)
Qal
QPc
underlying lithology uncertain
SAF
740
700
660
620
580
540
500
460
420
380
340
0
500
1000

Figure 4.7. A) 0.5 meter B4-LiDAR derived digital hillshade model 43.7 kilometers northwest of the Bidart Fan paleoseismic site along the SAF trend. This portion of the fault displays a geometrically simple trace of scarps (black lines; Figs. 4.2-4.4). Here some of the fault scarp interpretation may have been obscured by a road that parallels the SAF scarps along the sides of this linear fault valley within an area of relatively high elevation. The local surficial geology is primarily QPc (marine sand and mudstones) with local veneers of Quaternary alluvium. B) Aspect map is draped over a slope map with 35% transparency. C) An example of a cross sectional interpretation is provided from X to X'. Here, the active fault zone is less than 100 meters wide, less than $1/10^{th}$ the width observed 23.7 km southeast (Fig. 4.6).

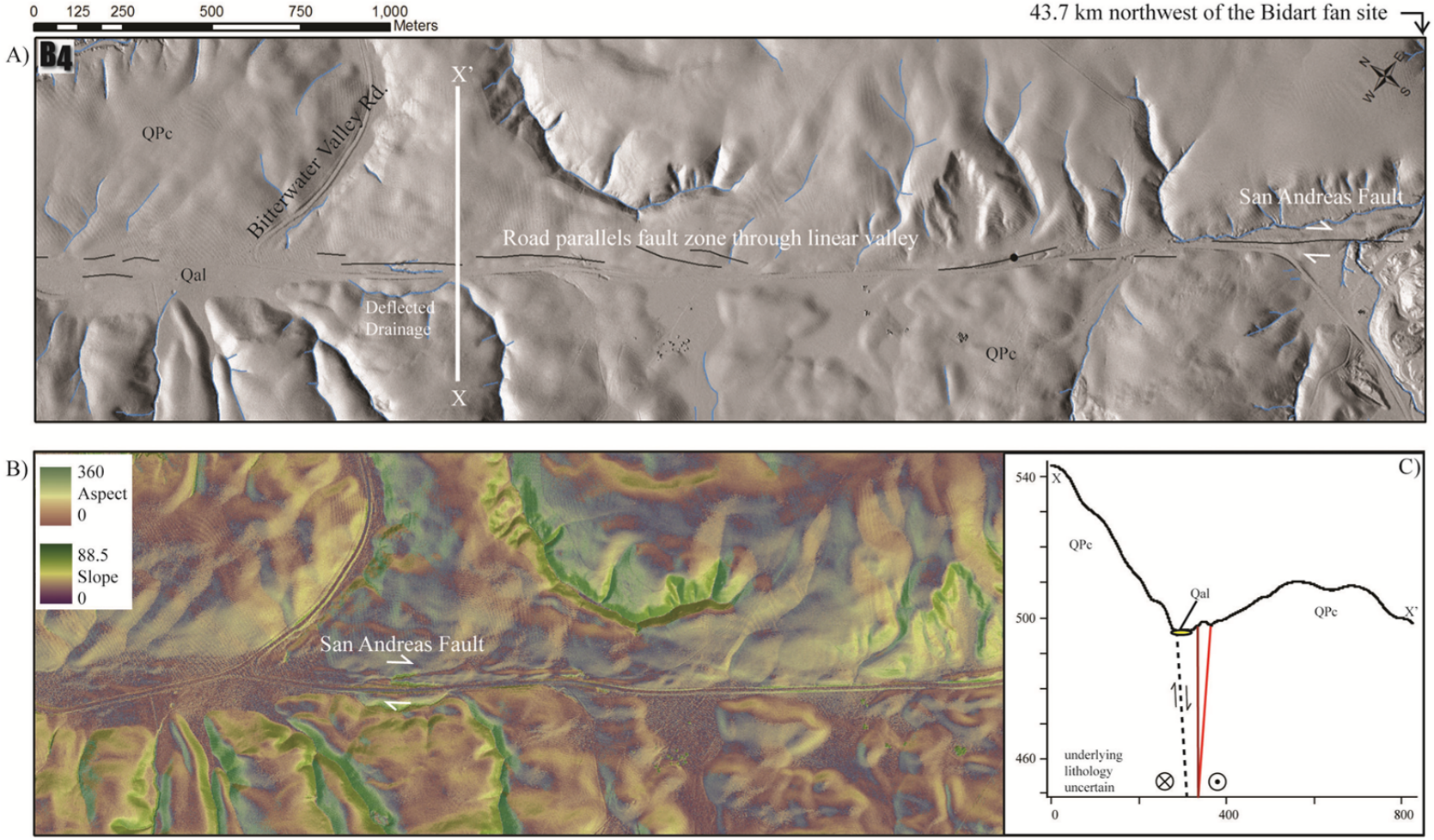
0 125 250 500 750 1,000
Meters
43.7 km northwest of the Bidart fan site
A)
B4
X'
X
QPc
Bitterwater Valley Rd.
Qal
Deflected Drainage
Road parallels fault zone through linear valley
San Andreas Fault
QPc
B)
360
Aspect
0
88.5
Slope
0
San Andreas Fault
C)
540
500
460
X
X'
QPc
Qal
QPc
underlying lithology uncertain
0
400
800

Figure 4.8. A) 0.5 meter B4-LiDAR derived digital hillshade model 60.4 kilometers northwest of the Bidart Fan paleoseismic site along the SAF trend. Mapped fault scarps are shown with black lines. This portion of the SAF is expressed at the surface as two fault traces bounding a topographic lobe and thus it has a high ratio of fault scarp length per kilometer of SAF (Figs. 4.4D). B) Aspect map is draped over a slope map with 35% transparency. This portion of the fault also displays an excellent example of a shutter ridge, deflected drainages as well as associated wind gaps across what appears to be an area of uplift SE of the fault which may be due to a small thrust fault.


0 125 250 500 750 1,000
Meters
60.4 km northwest of the Bidart fan site
A)
deflected drainages
SAF 2
SAF 1
sag
20 m
Thrust?
B)
360
Aspect
0
88.5
Slope
0
B4
Fault bounded topographic lobe
shutter ridge
fence line

Figure 4.9. A) 0.5 meter B4-LiDAR derived digital hillshade model 75 kilometers northwest of the Bidart Fan paleoseismic site along the SAF trend. Here the fault makes more than a 1 kilometer right step forming the Cholame Valley. Mapped fault scarps are shown with black lines. Here the 1966 Parkfield earthquake rupture trace (red lines, Crosby, 2004) is also displayed. The significantly-sized Cholame Creek (Fig. 4.10) flows from the northwest into the Cholame Valley, but does not exit the valley. Instead it fans out into the northern corner of the step over which appears to be the lone depocenter of this step over. On the southwest side of the step over channels have incised headward from the southeast. B) Within areas with low relief topography a slope map is more useful than the combined aspect and slope imagery. While prominent scarps are mostly absent within the step over, the pattern of distributed drainages is particularly curious and may be indicative of local regions of focused surface slip in creep and past earthquakes.

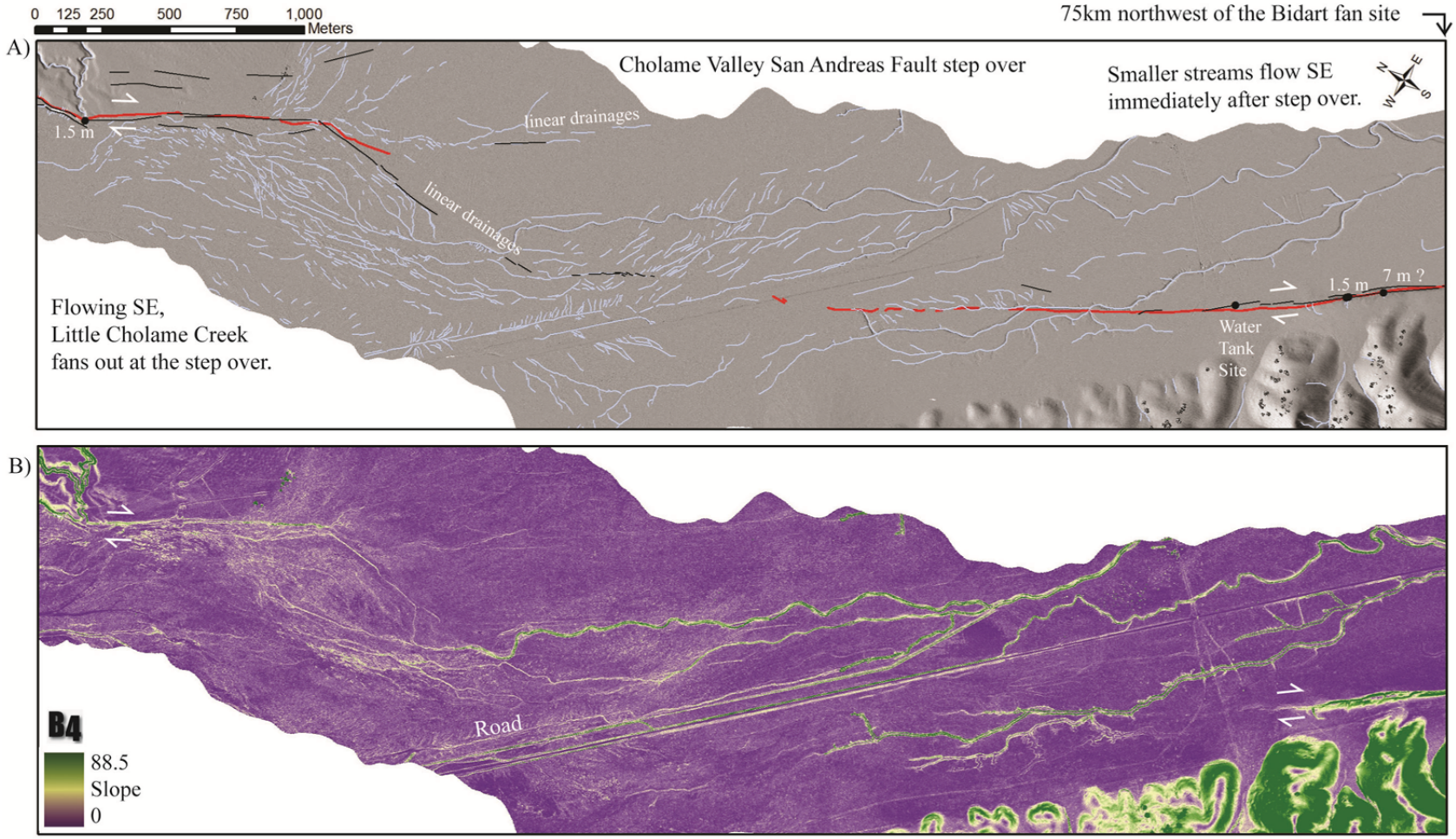
0 125 250 500 750 1,000
Meters
75km northwest of the Bidart fan site
A)
Cholame Valley San Andreas Fault step over
Smaller streams flow SE
immediately after step over.
N
E
S
W
1.5 m
linear drainages
linear drainages
Flowing SE,
Little Cholame Creek
fans out at the step over.
1.5 m
7 m ?
Water
Tank
Site
B)
B4
88.5
Slope
0
Road

Figure 4.10. A) 0.5 meter B4-LiDAR derived digital hillshade model 92.3 kilometers northwest of the Bidart Fan paleoseismic site along the SAF trend. Mapped fault scarps are shown with black lines. This portion of the fault displays relatively simple scarp geometry over the aperture of the B4 dataset, however, just beyond the data to the southwest is the Southwest Fracture Zone (SWFZ Figure 3.1 and Appendix B) which ruptured in the 1966 and 2004 Parkfield earthquakes. Additionally there was prominent surface cracking between the SWFZ and main SAF in 2004 which does not coincide with prominent scarps in the B4 data products. The Miller's Field site (Chapter 3) is located just northwest of Carr Hill in a fluvial terrace of the Little Cholame Creek. B) Aspect map is draped over a slope map with 35% transparency. This portion of the fault also displays excellent examples of several tectonic geomorphic indicators (see annotation).

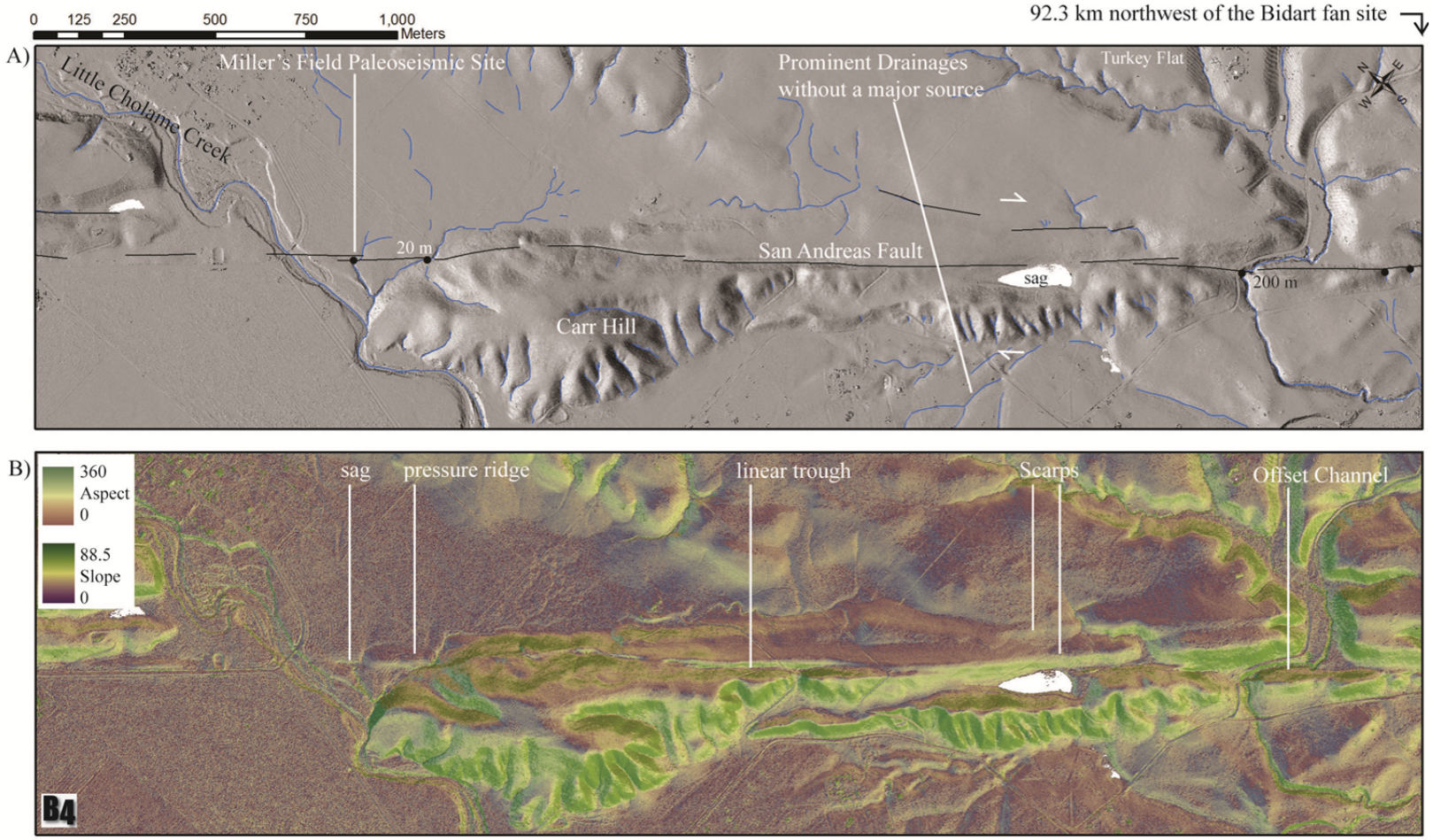
0 125 250 500 750 1,000
Meters
92.3 km northwest of the Bidart fan site
A)
Little Cholame Creek
Miller's Field Paleoseismic Site
Prominent Drainages
without a major source
Turkey Flat
20 m
San Andreas Fault
sag
200 m
Carr Hill
B)
360
Aspect
0
88.5
Slope
0
sag
pressure ridge
linear trough
Scarps
Offset Channel
B4

Figure 4.11. A) 0.5 meter B4-LiDAR derived digital hillshade model 116.7 kilometers northwest of the Bidart Fan paleoseismic site along the SAF trend. Mapped fault scarps are shown with black lines. This portion of the fault is the Creeping section which displays relatively complex scarp geometries and is a location where scarp slopes are high (Figs. 4.2-4.4). B) Aspect map is draped over a slope map with 35% transparency. This portion of the central SAF has the highest elevations and shortest wavelengths of topographic changes.

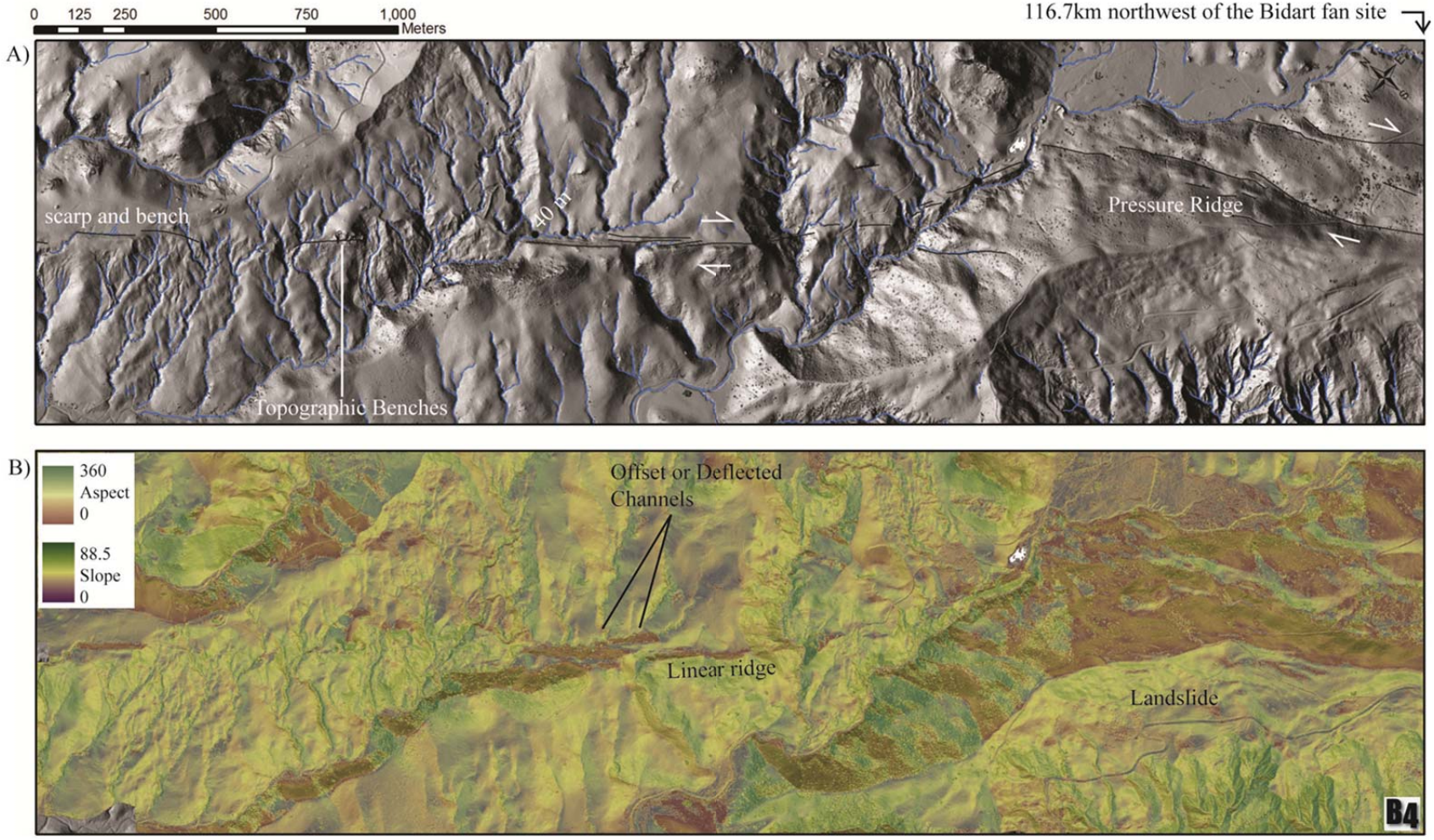
0 125 250 500 750 1,000
Meters
116.7km northwest of the Bidart fan site
A)
scarp and bench
40 m
Pressure Ridge
Topographic Benches
B)
360
Aspect
0
88.5
Slope
0
Offset or Deflected
Channels
Linear ridge
Landslide
B4

Figure 4.12. Boundaries between segments of varying fault scarp complexity are associated with areas where the main SAF (black lines mapped in this study) links with secondary and parallel faults that are not imaged by the B4 LiDAR (white lines: US Geological Survey, 2006). The extents of traditionally-described sections of the central SAF are plotted above the image. Distance along the fault, precipitation, and elevation graphs are included to make comparisons with the geometrical metrics on Figs. 4.2-4.4. Also, see table 4.1 for characterizations of each segment of varying fault scarp complexity.

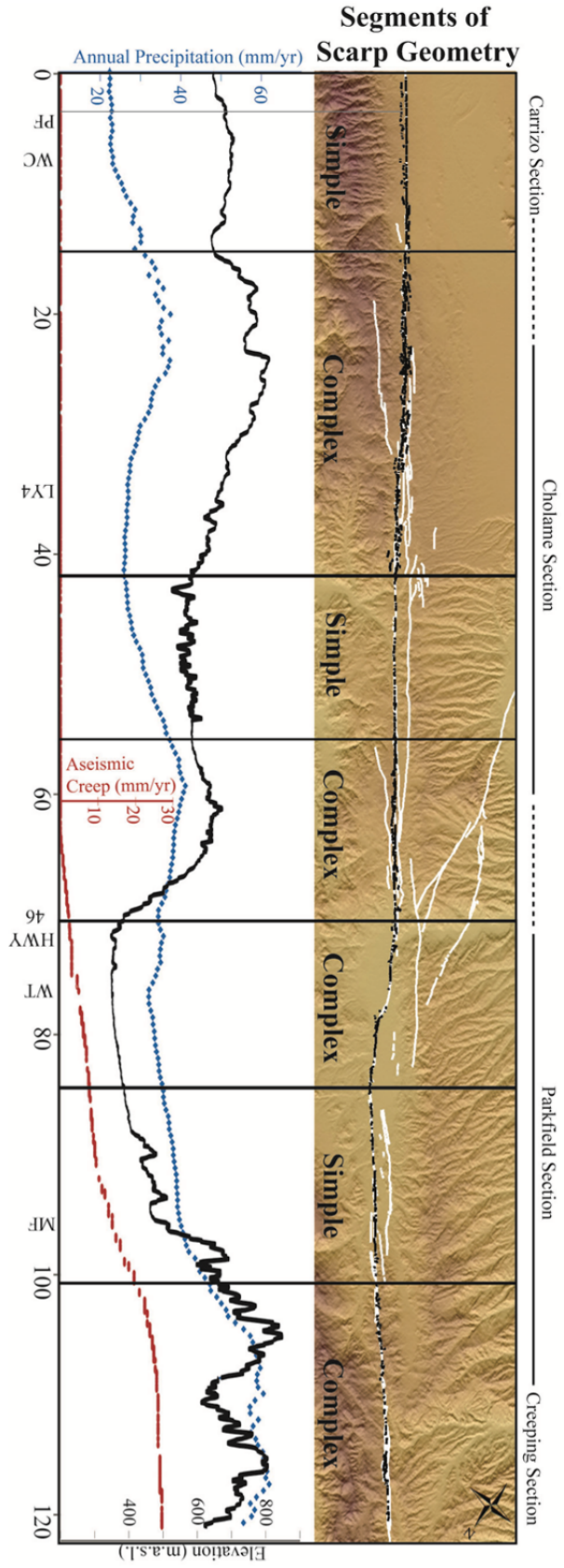
Segments of
Scarp Geometry
Annual Precipitation (mm/yr)
20
40
60
Simple
Complex
Simple
Complex
Complex
Simple
Complex
Aseismic
Creep (mm/yr)
10
20
30
0
PF
WC
20
LY4
40
60
46
HWY
WT
80
MF
100
120
400
600
800
Elevation (m.a.s.l.)
Carrizo Section
Cholame Section
Parkfield Section
Creeping Section
N

CHAPTER 5

CONCLUDING REMARKS

SUMMARY

This dissertation presents results from opposite ends of the seismic hazard analysis spectrum. Chapters 3 and 4 provide fundamental data about the slip rate, slip release mechanisms, and segmentation of the central San Andreas Fault. This data can be used to guide future earthquake science investigations and future probabilistic seismic hazard analyses. Chapter 2 demonstrates how seismic hazard analyses can be integrated with social science data to learn about the impact of hazards and regulation on the urban landscape and the people who may be affected by future earthquakes. This type of analysis is not typical of seismic hazard characterizations. Usually, such analyses are focused on minimizing economic losses by informing seismic engineering and insurance companies. However, economic losses do not capture the impact of hazards on socially vulnerable populations. Thus, chapter 2 represents another direction for earth scientists to apply hazards research. This route may prove equally valuable. In the concluding two sections, I provide additional commentary on the results presented herein and outline future directions for research on earthquake geology along the San Andreas Fault and the emerging field of environmental justice related to geologic hazards.

EARTHQUAKE GEOLOGY: RESULTS AND FUTURES

Chapter 3 presents evidence that the configuration of slip release behavior along the central SAF has persisted over thousands of years. This is an important finding because it supports the hypotheses that the composition of fault zone material plays a fundamental role in the dynamics of fault slip release and segmentation of fault zones. Long term configurations of slip behavior also provides reassurance for our current, yet evolving, models of seismic hazard analysis. This chapter also provides the first geologic slip rate measured along the Parkfield section of the San Andreas Fault. This rate is lower than measurements in the Carrizo Plain and suggests that nearby subsidiary faults may be important for accommodating plate boundary slip at the latitude of Parkfield.

Chapter 4 presents detailed fault scarp mapping along 122 kilometers of the central San Andreas Fault. This data provides new observations about variations in the complexity of residual fault scarp arrays. Fault scarp array complexity is spatially correlated to zones of convergence between subsidiary faults and the main SAF. In these regions of fault interaction scarp array complexity is high. The wavelength of these interactions is similar to the depth of the seismogenic crust. These results indicate that faults like the SAF have multiple levels of segmentation which may be important in the dynamics of large surface rupturing earthquakes. A hierarchy of fault segmentation helps to explain recent paleoseismic results along the central SAF which infer non-characteristic earthquake ruptures of varying slip and rupture length.

Future paleoseismic investigations along the central SAF should follow up on the implications extending from this dissertation by addressing the following questions: How active are sub parallel structures along the central SAF? Can differences in the activity of these structures explain the discrepancies observed in slip rates between Parkfield and the Carrizo? How does the activity along sub parallel faults relate to ruptures along the main SAF? Fault scarp mapping clearly shows that these faults influence one another. Do portions of the main SAF rupture with these secondary structures?

The hypothesis that fault segmentation scales with the depth of the seismogenic crust is compelling considering the results of chapter 4. The tool of LiDAR will be valuable for addressing this question because it can be used to systematically map entire plate boundary faults and quantify many metrics of segmentation. If along-strike segmentation scales with the depth of ruptures then we need to explain this result physically. Is segmentation related to deep crustal structure? Could it be linked to fault growth and fault interactions? To address these types of questions comprehensive imaging campaigns such as the B4 project should make greater efforts to image secondary faults so that we can better understand how these structures interact.

RELATING GEOLOGIC HAZARDS TO ENVIRONMENTAL JUSTICE

Fortunately, or unfortunately for the insurance companies, Chapter 2 shows that the wealthiest neighborhoods in Los Angeles are situated closest to the primary sources of seismic hazard in southern California. This is a common

situation within wealthy first world countries: the wealthiest communities are situated next to areas of great geologic beauty including mountain fronts, coastlines, and river fronts. These areas are associated with the greatest occurrence of natural hazards.

While it was not discussed in Chapter 2, I am not sure that this geographical relationship is the same in developing nations where we have not done as thorough a job of creating a perception of tamed nature. Low lying areas in coastal third world countries present the greatest risk of malaria. In such areas, those with more access to resources are able to implement preventative measures, which include moving. Additionally, within developing nations, cities are still arranged such that wealth is concentrated within the central city. Unlike the Los Angeles region, the surrounding hillsides are reserved for shanty towns. This type of city, located within a similarly seismogenic region, would have a very different spatial relationship between the hazard of earthquakes and the poorest residents. Finally, the important thing to remember when drawing conclusions about the impact of seismic hazard is that spatial distance from the primary hazard is not necessarily the determinant of outcome in a disaster. It may better be characterized by social vulnerability and the location relevant to human constructed environmental hazards such as toxic waste facilities or nuclear power plants that can fail in hazard events.

Many opportunities exist for exploring the relationships among geologic hazards, societal measures of control, and the impact of hazards on communities. In future analyses, effort should be made to go beyond the distributional analyses

presented here. For instance, Chapter 2 implies that unregulated fault zones may be occupied by slightly wealthier populations than those that are regulated. Distributional analysis cannot resolve the reason behind this difference. Are they wealthier because they have not been regulated? Are they free of regulation because they have wealth and political power? Some questions must be answered by talking to people. How do residents near fault zone parks perceive these spaces? We can guess that they enjoy them because of increased home value with proximity to the parks, but do the residents know of the hazard? Do they care? Distributional analyses are important for initial characterizations of socio-environmental interactions, but they cannot answer questions about perception or decision making. Qualitative research methods (e.g., interviews with residents and regulators, observation of park space usage, or surveys of these groups) must be employed. This type of research will require significantly more integration between earth science and social science.

I will conclude with a quote by John Dewey:

"*Arriving at one goal is the starting point to another.*"

APPENDIX A

CHAPTER 2 SUPPLEMENTARY:

LARGER REPRESENTATION OF PANELS FROM FIGURES 2.3

Figure 2.3 was produced for journal publication and it contains a dense amount of information. It is not ideally suited for 1.5 inch margins. This appendix breaks each panel of the figure into separate figures for readability. The relevant portions of their respective captions are included prior to each panel. Also see Table 2.2.

Figure 2.3, Panel A. Probabilistic seismic hazard map for the Los Angeles region (US Geological Survey, 2008) showing contours of peak ground acceleration (PGA), expressed in percent of gravity (%G), with a 10% probability of occurrence in the next 50 years. Earthquake rupture hazard is represented by Alquist-Priolo (AP) Act earthquake fault zones (black polygons) and other non-AP zone active faults which are shown with grey lines (U.S. Geological Survey, 2006). For each social indicator map AP zones (black polygons) and areas with the extreme ground shaking hazard are shown (PGA > 60% G: grey shading). The gap along San Jacinto AP zone is because for analyses these zones were clipped to the urban area.

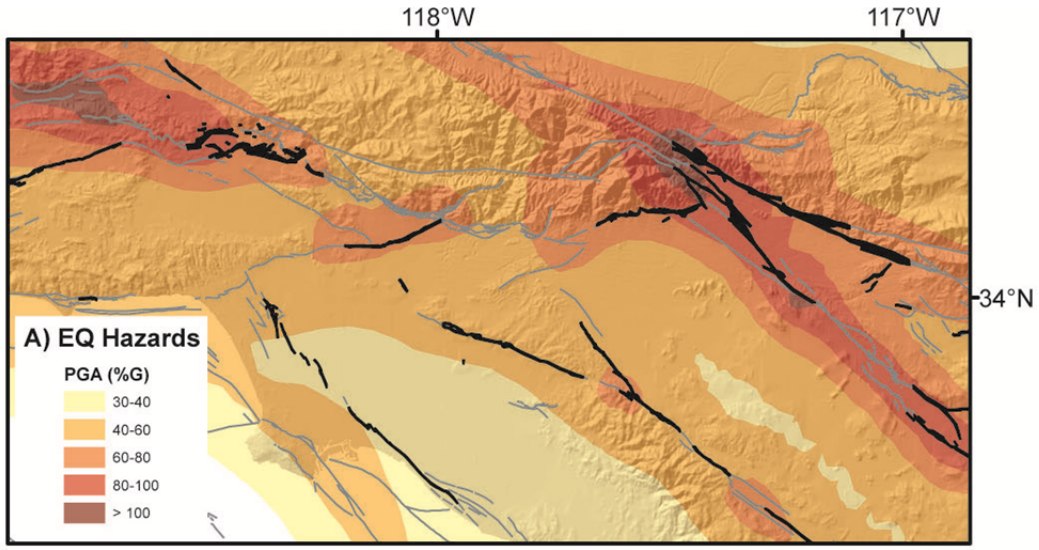

Figure 2.3, Panel B. Local economy and workforce is one of the seven indicators making up the social vulnerability calculation. This sub-index of the LA-SoVI is a combination of three natural break transformations: percent of population working; percent of population with a disability, percent of households with Social Security income. AP zones (black polygons) and areas with the extreme ground shaking hazard are shown (PGA > 60% G: grey shading). The gap along San Jacinto AP zone is because these zones were clipped to the urban area.

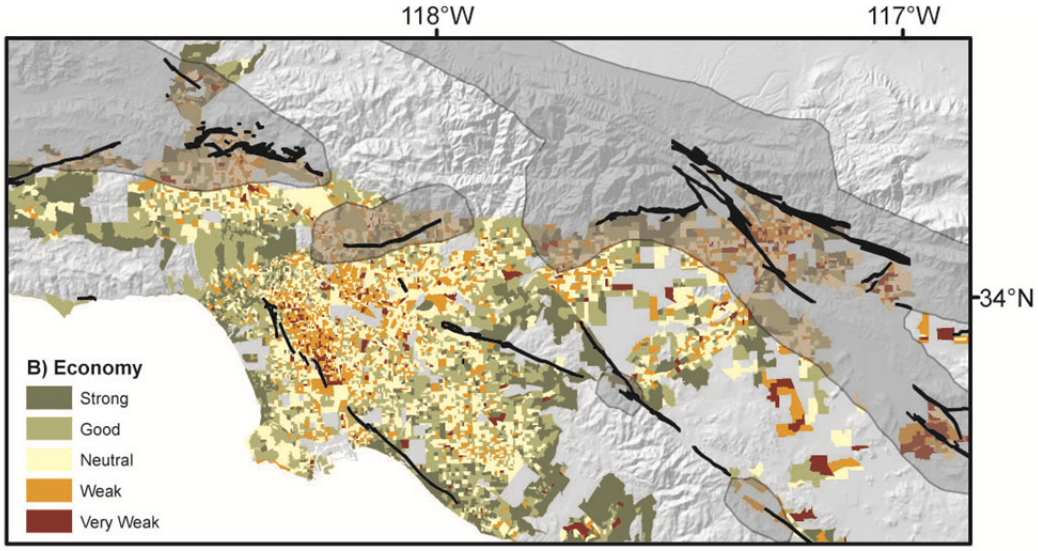

Figure 2.3, Panel C. An important component of the LA-SoVI is the proportion of underrepresented groups (percent female, percent recent immigrants, and percent minorities). Here we describe this part of the index as representation. Thus, where underrepresented groups are less prevalent representation is stronger. AP zones (black polygons) and areas with the extreme ground shaking hazard are shown (PGA > 60% G: grey shading). The gap along San Jacinto AP zone is because these zones were clipped to the urban area.

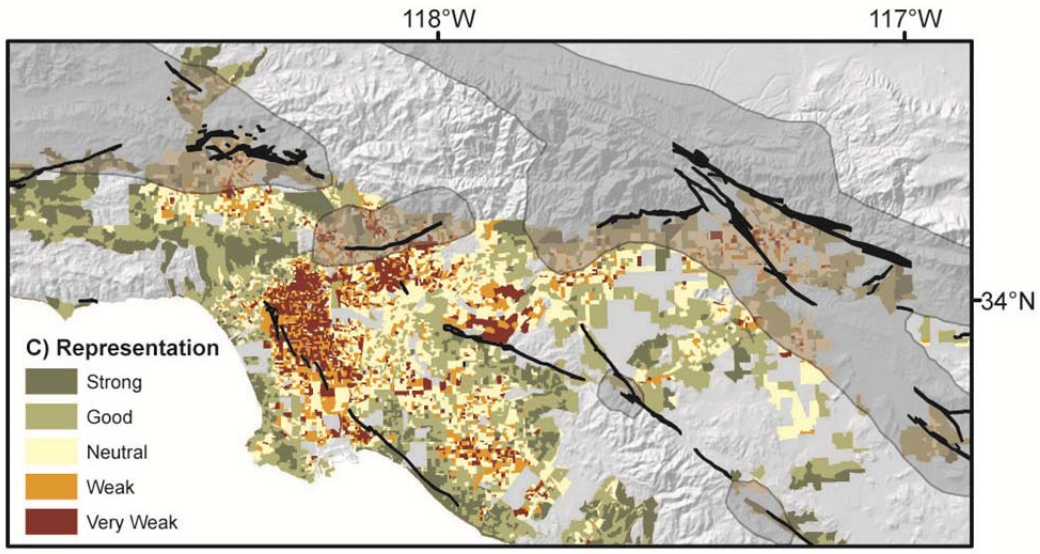

Figure 2.3, Panel D. Housing stock and tenure (percent of housing built before 1970, percent vacant, and percent renter occupied) is an important aspect of social vulnerability to earthquakes because housing built after the many earthquake regulations that were enacted in the 1970s are likely to better withstand ground shaking and because greater vacancy and proportions of renters are correlated with generally poorer economic and social conditions. AP zones (black polygons) and areas with the extreme ground shaking hazard are shown (PGA > 60% G: grey shading). The gap along San Jacinto AP zone is because these zones were clipped to the urban area.

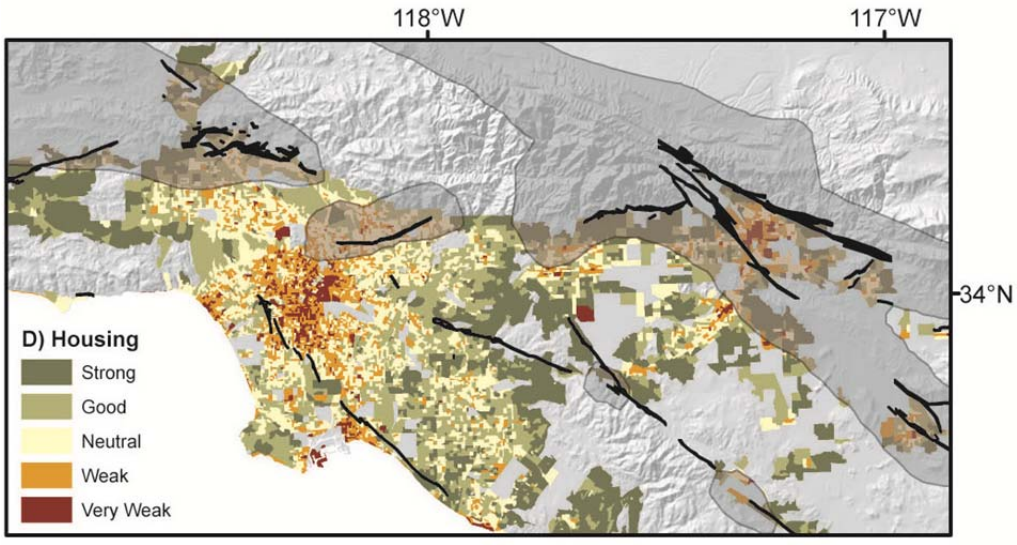

Figure 2.3, Panel E. The LA-SoVI takes into account the strength of social safety nets with the following three metrics: percent of population below 18 and over 65, percent single parent households, and percent single person households where the person is over 65. AP zones (black polygons) and areas with the extreme ground shaking hazard are shown (PGA > 60% G: grey shading). The gap along San Jacinto AP zone is because these zones were clipped to the urban area.

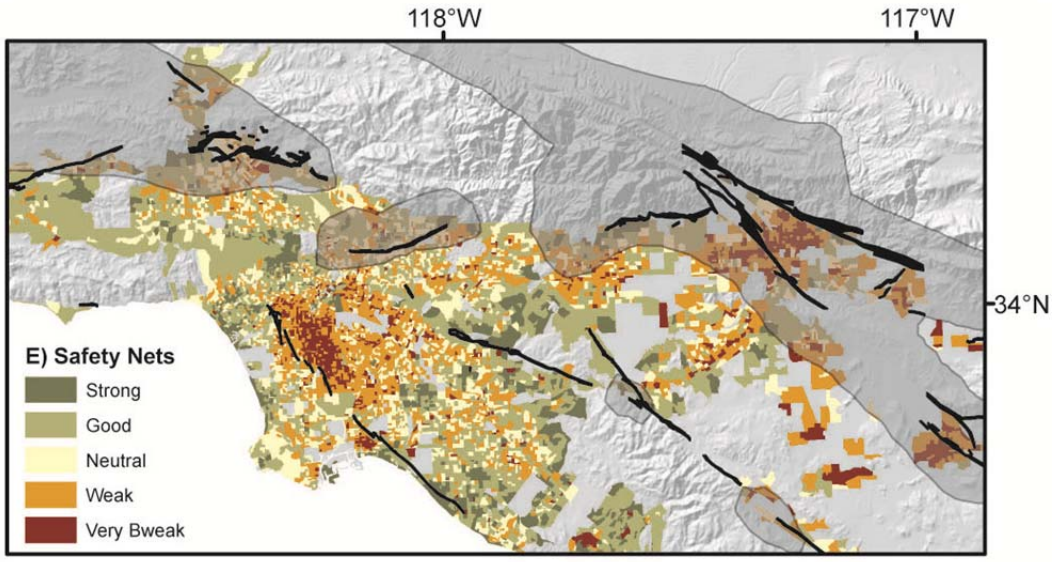

Figure 2.3, Panel F. Relative census block group wealth is accounted for by assessing the mean 1999 per capita income, the percent of households with income above $75K/year, and the percent of people below the poverty level. AP zones (black polygons) and areas with the extreme ground shaking hazard are shown (PGA > 60% G: grey shading). The gap along San Jacinto AP zone is because these zones were clipped to the urban area.

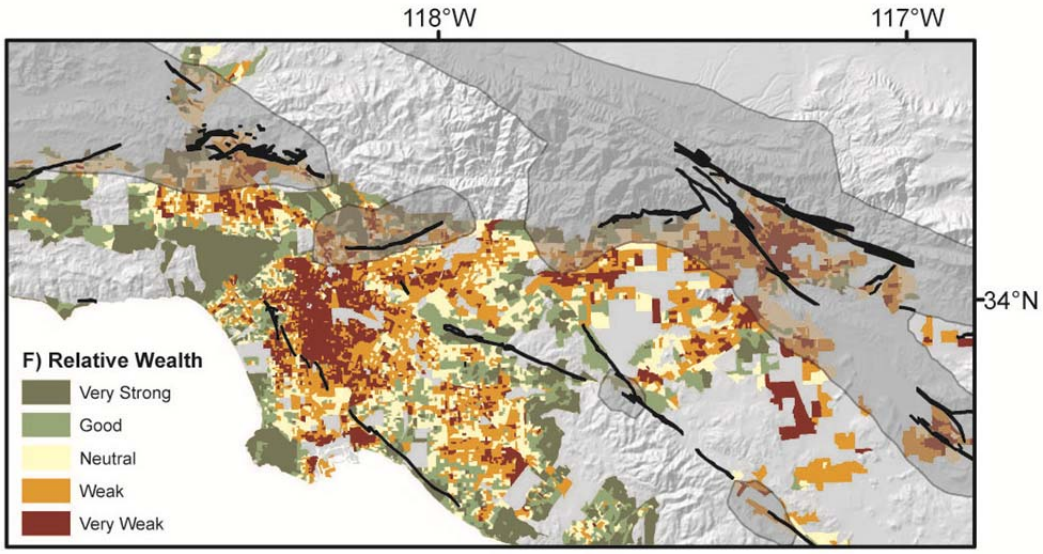

Figure 2.3, Panel G. Infrastructure dependence takes into account both physical infrastructure (percent of workers with a long commute and population density) as well as social infrastructure (percent of households receiving some form of public assistance). AP zones (black polygons) and areas with the extreme ground shaking hazard are shown (PGA > 60% G: grey shading). The gap along San Jacinto AP zone is because these zones were clipped to the urban area.

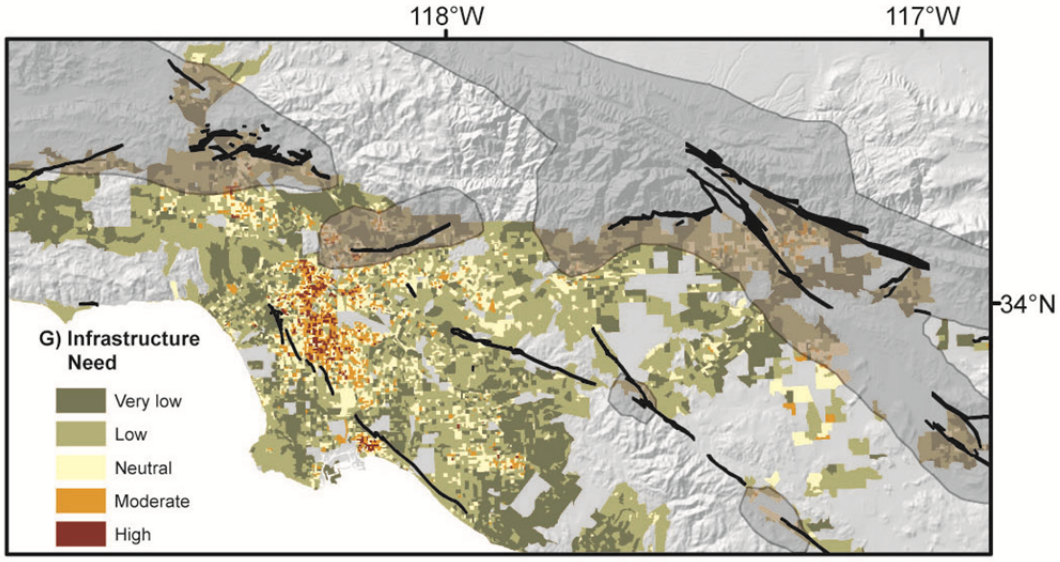

Figure 2.3, Panel H. Density of the built environment is described with housing units per square mile and average household size. AP zones (black polygons) and areas with the extreme ground shaking hazard are shown (PGA > 60% G: grey shading). The gap along San Jacinto AP zone is because these zones were clipped to the urban area.

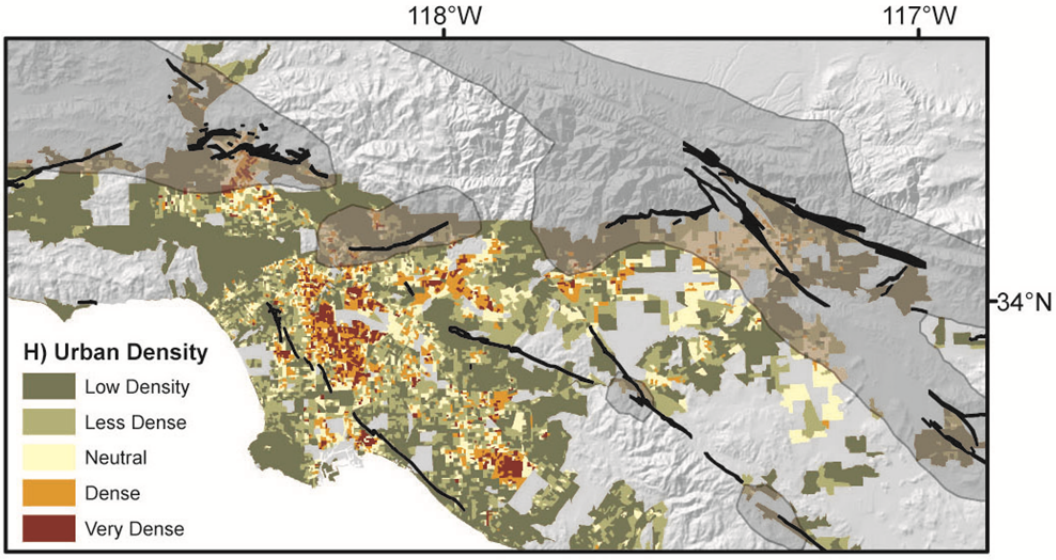

APPENDIX B

CHAPTER 3 SUPPLEMENTARY:

SOUTHWEST FRACTURE ZONE PILOT STUDY FIGURE

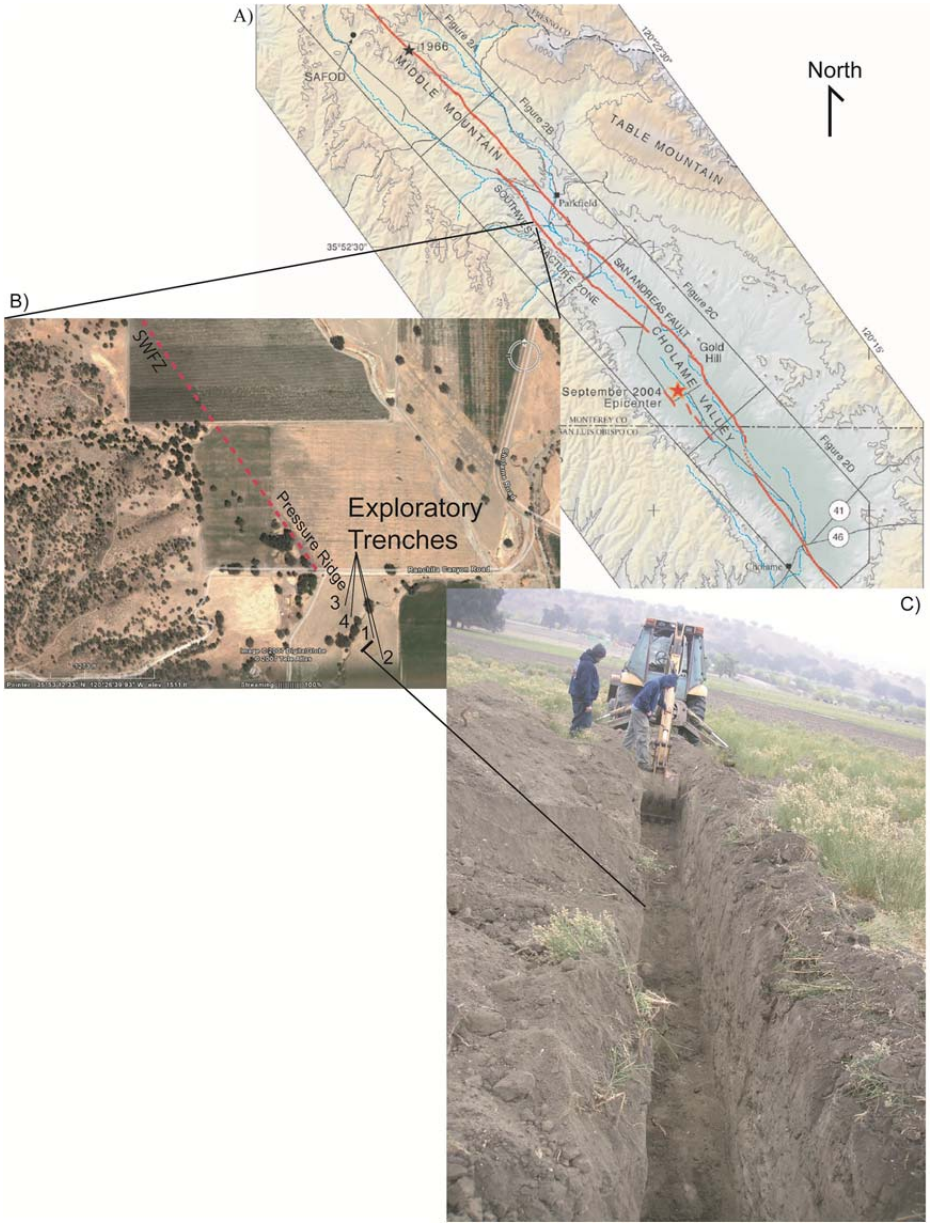

Figure B1. A) The Southwest Fracture Zone (SWFZ) is parallel and about 1 km SW of the main SAF along the Parkfield segment (map from Rymer et al., 2006). B) The SWFZ exploratory paleoseismic trenches (black footprint and sites 1-4) were located just south of Ranchita Canyon Road to the sides of an ephemeral stream incised into an alluvial fan extending from Ranchita Canyon. This area of

the SWFZ was defined tectonically by a prominent pressure ridge to the NW and a wide vegetation lineament at the trench site. C) The longest of the trenches was dug across a subtle scarp in the fan surface and into the wide vegetation lineament along the projection of surface fractures from the SE (observed in the 2004 earthquake). Unfortunately, the fan's stratigraphy was heavily bioturbated in each of the test trenches. This fan does not appear to be a good candidate for paleoseismic investigation.

REFERENCES CITED ONLY IN APPENDIX B

Rymer, M. J., Tinsley J. C., Treiman J. A., Arrowsmith J R., Clahan K. B., Rosinski A. M., Bryant W. A., Snyder H. A., Fuis G. S., Toke N., and Bawden G. W., 2006, Surface fault slip associated with the Parkfield, California, Earthquake: Bulletin of the Seismological Society of America, 96, no. 4B, S11–S27, doi: 10.1785/0120050830

APPENDIX C

CHAPTER 3 SUPPLEMENTARY:

RADIOCARBON ANALYSIS DATA TABLES

Table C1. Radiocarbon data from Miller's Field Site sag pond paleoseismic trenches arranged in stratigraphic order (see Fig. 3.3 and Appendix D). Pretreatment and analyses were performed by either the NSF-Arizona AMS facility at the University of Arizona (AA-#) or the KECK University of California Irvine AMS Facility (UCI-#). These facilities use the background correction of Stuiver and Polach, (1977).

Sample ID[1]	NSF-AMS#	Sample Description	Stratigraphic Unit[2]	Fraction Modern	+/- [3]	^{14}C age (years BP)	+/- [4]	2σ calibrated age (cal A.D. / B.C.)[5]	Modeled and Trimmed 2σ calibrated age (cal A.D. / B.C.)[6]
(2) 04MST-33	AA-61393 UCI-49998	charcoal	between MSW-103 and MSW-104 (laminated silt/clay)	0.7044 0.7548	0.0033 0.0011	2815 (detrital) 2260	37 15	400-350 B.C. (53.4 %) 290-230 B.C. (42.0%)	400-350 B.C. (53.4 %) 290-230 B.C. (42.0%)
(2) 04MST-9	AA-61386 UCI-49993	charcoal	between MSE-101 and MSE-102 (laminated Silt/clay)	0.7563 0.7544	0.0034 0.0011	2243 2265	36 15	400-350 B.C. (57.5%) 290-230 B.C. (37.9%)	400-350 B.C. (57.5%) 290-230 B.C. (37.9%)
07MST-P1	*UCI-49992*	*charcoal piece*	*MSE-103 (massive clayey silt)*	*0.7445*	*0.0010*	*2370*	*15*	*510-430 B.C. (23.8%) 420-390 B.C. (71.6%)*	*Detrital*
04MST-6	*UCI-49552*	*charcoal*	*MSE-103 (massive clayey silt)*	*0.7438*	*0.0015*	*2375*	*20*	*520-390 B.C.*	*Detrital*
04MST-18	UCI-49994	charcoal	lower charcoal stringer within MSE-108 (dark clay)	0.8790	0.0028	1035	30	890-920 A.D. (5.6%) 940-1040 A.D. (89.8%)	890-920 A.D. (6.7%) 940-1040 A.D. (88.7%)
04MST-17	*AA-61387*	*charcoal*	*MSE-110 (buried organic horizon)*	*0.8508*	*0.0037*	*1298*	*35*	*650-780 A.D.*	*Detrital*
04MST-26	*AA-61390*	*charcoal*	*MSE-110 (clayey silt)*	*0.7867*	*0.0035*	*1927*	*36*	*20-10 B.C. (1.0%) 0-140 A.D. (90.1%) 150-180 A.D. (2.3%) 190-220 A.D. (2.0%)*	*Detrital*
04MST-27	UCI-49996	charcoal	between MSE-111 and MSE-112 (clayey silt)	0.9430	0.0025	470	25	1410-1450 A.D.	1410-1450 A.D.
04MST-21	*UCI-49566*	*charcoal*	*MSE-112 (silty clay)*	*0.8663*	*0.0038*	*1155*	*40*	*770-980 A.D.*	*Detrital*

07MST-9	*UCI-49565*	*charcoal*	*MSE-112 (silty clay)*	*0.9186*	*0.0072*	*680*	*70*	*1220-1410 A.D.*	*Detrital*
04MST-22	*AA-61388*	*charcoal*	*MSE-112 (silty clay)*	*0.9221*	*0.004*	*652*	*35*	*1270-1330 A.D. (44.7%) 1340-1400 A.D. (50.7%)*	*Detrital*
04MST-3	UCI-49551	charcoal	MSE-112 (silty clay)	0.9493	0.0019	420	20	1430-1490 A.D.	1430-1460 A.D.
04MST-24	*AA-61389*	*charcoal*	*MSE-114 (laminated silt)*	*0.8311*	*0.0056*	*1486*	*55*	*1160-1300 A.D.*	*Detrital*
04MST-25	UCI-49554	charcoal	between MSE-114 and MSE-115 (laminated silt)	0.9485	0.0021	425	20	1430-1485 A.D.	1440-1470 A.D.
04MST-28	*UCI-49555*	*charcoal*	*top of MSE-115 (laminated silt/clay)*	*0.9287*	*0.0019*	*595*	*20*	*1300-1370 A.D. (72.2%) 1380-1410 A.D. (23.2%)*	*Detrital*
04MST-29	UCI-49997	charcoal	within MSE-115 (silty sand)	0.9488	0.0016	420	15	1435-1480 A.D.	1440-1480 A.D.
07MST-8	UCI-49564	charcoal	between MSE-117 and MSE-118 (silty sand)	0.9486	0.040	425	35	1410-1530 A.D. (86.2%) 1590-1620 A.D. (9.2%)	1440-1530 A.D. (91.0%) 1590-1620 A.D. (4.4%)
04MST-16	UCI-49553	charcoal piece	MSW-106 (clayey sand)	0.9545	0.0019	375	20	1440-1530 A.D. (67.6%) 1570-1630 A.D. (27.8%)	1440-1530 A.D. (67.6%) 1570-1630 A.D. (27.8%)
04MST-32	*AA61392*	*charcoal*	*MSE-118 (sandy clay)*	*0.7833*	*0.0049*	*1961*	*51*	*100 B.C.-140 A.D.*	*Detrital*
04MST-30	*AA61391*	*charcoal*	*MSE-119 (silty clay)*	*0.9558*	*0.0041*	*363*	*34*	*1440-1640 A.D.*	*Detrital*
04MST-31	UCI-49556	charcoal	MSE-119 (silty clay)	0.9761	0.0020	195	20	1650-1690 A.D. (22.2%) 1730-1810 A.D. (53.3%) 1930-1960 A.D. (20.9%)	1650-1690 A.D. (22.3%) 1730-1810 A.D. (52.3%) 1930-1960 A.D. (20.8%)

(1) Assigned sample name based upon: A) the year collected, B) the trench of collection, and C) the order of collection
(2) Stratigraphic unit: Trench name, east or west stratigraphy, higher numbers are younger layers. 2004 and 2007 units are correlative here, but different names were used in Toke et al., 2006. Here MSE-119 is equivalent to MSE-24 in 2004; MSW-106 here is equivalent to MSW-7 in 2004; MSE 5 from 2004 is subdivided to MSE 105-107; MSE 8 from 2004 is equivalent to MSE 109-110 here. For further explanation see figure D1 and Toke et al., 2006.
(3) Error value (2σ) assessed in the calculation of the modern fraction.
(4) Error value (2σ) assessed in the calculation of ^{14}C years before present.
(5) Determined using single samples in OxCal 3.10 (Bronk Ramsey, 1995; 2001; and 2005) and using the atmospheric data of Reimer et al., (2004).
(6) Same as (5), but sequenced, modeled, and trimmed in OxCal v3.10 after *removal of detrital samples*.

Table C2. Radiocarbon data, from Miller's Field Site pressure ridge paleoseismic trenches. Arranged by relative stratigraphic age (see Appendix E). Pretreatment and analyses were performed by either the NSF-Arizona AMS facility at the University of Arizona (AA-#) or the KECK University of California Irvine AMS Facility (UCI-#). These facilities use the background correction of Stuiver and Polach, (1977).

Sample ID[1]	NSF-AMS#	Sample Description	Stratigraphic Unit[2]	Fraction Modern	+/- [3]	^{14}C age (years BP)	+/- [4]	2σ calibrated age (cal A.D. / B.C.)[5]	Modeled and Trimmed 2σ calibrated age (cal A.D. / B.C.)[6]
07PT-SE14	UCI-49563	charcoal	PTE-033 (thin laminated silt/clay)	0.6498	0.0013	3460	20	1880-1730 B.C (87.6%) 1720-1690 B.C. (7.8%)	1880-1730 B.C. (87.7%) 1720-1690 B.C. (7.7%)
04PT-7	*AA-61382*	*charcoal*	*PTE-037 (thin laminated silt/clay)*	*0.6018*	*0.0029*	*4079*	*39*	*2870-2800 B.C. (16.3%) 2760-2480 B.C (79.1%)*	*Detrital*
(2) 07PT-NW9	UCI-49991 UCI-49560	charcoal	PTE-040 (clayey sand)	0.6884 0.6891	0.0009 0.0016	3000 2990	15 20	1310-1190 B.C. (91.2%) 1180-1160 B.C (1.5%) 1150-1130 B.C. (2.7%)	1320-1190 B.C. (92.3%) 1180-1160 B.C. (1.1%) 1150-1130 B.C. (2.0%)
04PT-3	*AA-61381*	*charcoal single piece*	*PTE-042 (thin laminated silt/clay)*	*0.6677*	*0.0033*	*3244*	*40*	*1620-1430 B.C.*	*Detrital*
(2) 04PT-8	*AA-61383 UCI-49990*	*charcoal single piece*	*PTE-043 (clayey silt)*	*0.6993 0.6940*	*0.0032 0.0009*	*2873 2935*	*37 15*	*1210-1040 B.C.*	*Detrital*
07PT-NW2	*UCI-49558*	*charcoal*	*PTE-043 (light grey silt/clay)*	*0.7007*	*0.0016*	*2855*	*20*	*1120-970 B.C. (86.5%) 960-930 B.C. (8.9%)*	*Detrital*
04PT-1	UCI-49989	charcoal	PTE-043 (clayey silt)	0.7299	0.0012	2530	15	800-530 B.C	810-660 B.C.
07PT-NW-1	UCI-49557	charcoal	PTE-047 (near boundary with sandy unit and C-horizon)	0.7293	0.0017	2535	20	800-740 B.C. (41.0%) 690-660 B.C (22.0%) 650-550 B.C. (32.4%)	780-740 B.C. (5.2%) 690-660 B.C. (40.5%) 650-560 B.C. (49.8%)
07PT-NW-4	UCI-49559	charcoal	PTE-048g (light grey clay)	0.7297	0.0015	2530	20	790-740 B.C. (34.5%) 690-660 B.C. (21.7%) 650-540 B.C. (39.2 %)	690-660 B.C. (8.8%) 650-540 B.C. (86.6%)
07PT-SE12	UCI-49562	charcoal	PTFZ-010 (dark clay in FZ)	0.8475	0.0017	1330	20	650-710 A.D. (85.7%) 740-770 A.D. (9.7%)	650-710 A.D. (87.4%) 740-770 A.D. (8.0%)
07PT-NW16	UCI-49561	charcoal	PTW-096 (clayey sand)	0.8465	0.0019	1340	20	640-700 A.D. (91.5%) 750-770 A.D. (3.9%)	640-700 A.D. (91.5%) 750-770 A.D. (3.9%)

04PT-13	AA-61384	Charcoal	PTFZ-005 (thin layer of leaf and other organic matter)	0.916	0.0039	705	35	1250-1320 A.D. (74.1%) 1350-1390 A.D. (21.3%)	1250-1320 A.D. (71.5%) 1350-1390 A.D. (23.9%)

(1) Assigned sample number based upon: A) the year collected, B) the trench of collection, and C) the order of collection.

(2) Stratigraphic unit: Trench name, east or west stratigraphy, higher numbers are younger layers. Units are correlative between 2007 and 2004 trenches however the unit names have been changed: Here PTW-096 is equivalent to PTW 5; PTE-039 is correlative to PTE 11; and PTE-048 is correlative to PTE 1.

(3) Error value (2σ) assessed in the calculation of the modern fraction.

(4) Error value (2σ) assessed in the calculation of ^{14}C years before present.

(5) Determined using single samples in OxCal v3.10 using the atmospheric data of Stuiver et al., (1998).

(6) Same as (5), but sequenced, trimmed, and modeled in OxCal v3.10 without clearly detrital samples.

REFERENCES CITED ONLY IN APPENDIX C:

Bronk Ramsey C. 1995 Radiocarbon Calibration and Analysis of Stratigraphy: The OxCal Program: Radiocarbon v. 3, no. 2, p. 425-430.

Bronk Ramsey C., 2001, Development of the Radiocarbon Program OxCal: Radiocarbon, v. 43, no. 2A, p. 355-363.

Bronk Ramsey, C., 2005. OxCal Program v 3.10.

Reimer PJ, MGL Baillie, E Bard, A Bayliss, JW Beck, C Bertrand, PG Blackwell, CE Buck, G Burr, KB Cutler, PE Damon, RL Edwards, RG Fairbanks, M Friedrich, TP Guilderson, KA Hughen, B Kromer, FG McCormac, S Manning, C Bronk Ramsey, RW Reimer, S Remmele, JR Southon, M Stuiver, S Talamo, FW Taylor, J van der Plicht, and CE Weyhenmeyer. 2004: Radiocarbon v. 46, p. 1029-1058.

Stuiver, M. and H.A. Polach (1977). Discussion: Reporting of 14C data: Radiocarbon v. 19, p. 355-63.

ADDITIONAL ACKNOWLEDGEMENTS

2004 radiocarbon samples were processed at the University of Arizona AMS facility in Tucson Arizona. 2007 samples were processed at the University of California, Irvine W. M. Keck Carbon Cycle Accelerator Mass Spectrometry Laboratory as a part of the 2008 SCEC Geochronology fund. We thank J. Southon for his helpful communication as we worked to get these samples processed.

APPENDIX D

CHAPTER 3 SUPPLEMENTARY:

MILLER'S FIELD SITE SAG POND TRENCH FIGURES 2004-2007

For completion all trench logs are included here. However, their quality is marginal at this scale. Please refer to the supplimentary online material of the published version of Chapter 3 (Toke et al., 2011) for high resolution graphics.

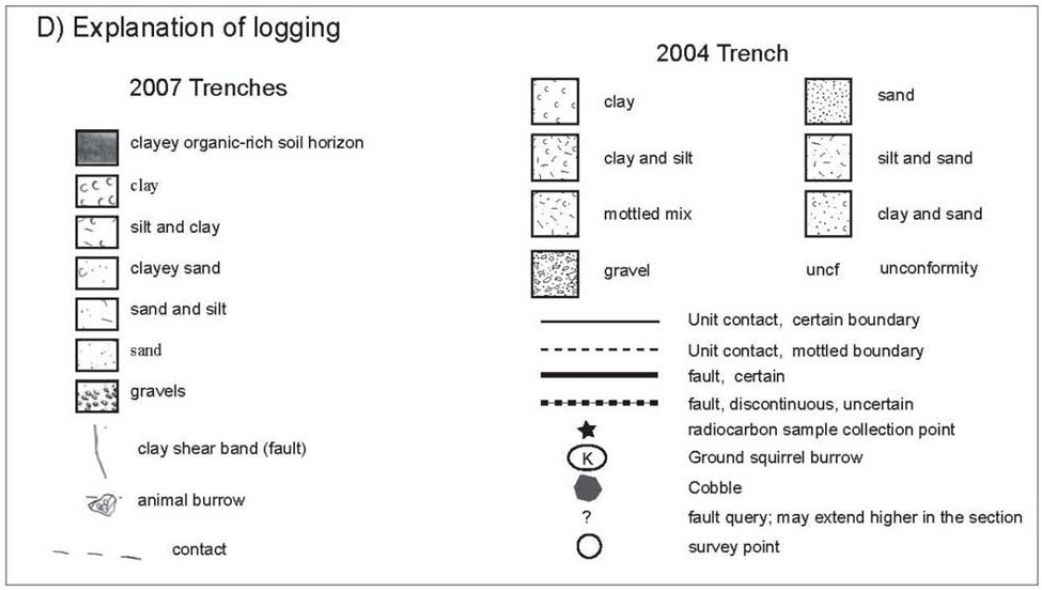

Figure D1. Explanation of paleoseismic logging for Appendices D and E.

Figure D2. The fault-perpendicular 2007 Miller Sag Trenches (a-c; Toke et al., 2011) exposed the same stratigraphic sequence as the 2004 MST trenches (d-f; Toke et al., 2006). However, the 2007 trenches revealed the continuity of the stratigraphy across fault zone 2 (FZ2) and provided additional radiocarbon samples. Here we plot a summary of the 2-sigma trimmed age ranges interpreted from all MST trenches (2004 and 2007) on the MST07se trench log within the corresponding unit. For detailed age ranges see Appendix C. The MST07se and MST04se photologs (b and e, respectively) provide a visual reference the logging interpretations. Note the obliquity of the fault surfaces exposed between FZ3 and FZ4 in the photologs (see Appendix F). The MSTnw trenches (c and f) were drawn with considerably less deformation interpretation because it was difficult to discern the clay shear bands on the sun facing side of the trench. Stratigraphy consisted of a variety of terrace deposits and reworked sag material (g). For a detailed explanation of individual units see Chapter 3. MST07parallel (h) exposed the tabular beds of overbank terrace deposits. The stratigraphy in the parallel trench exposes units MSE 102 - MSE 105 and intersects the 2004 and 2007 fault perpendicular trenches (unlogged zones).

a) 2007 Miller Sag Trench, southeast wall (MST07se)

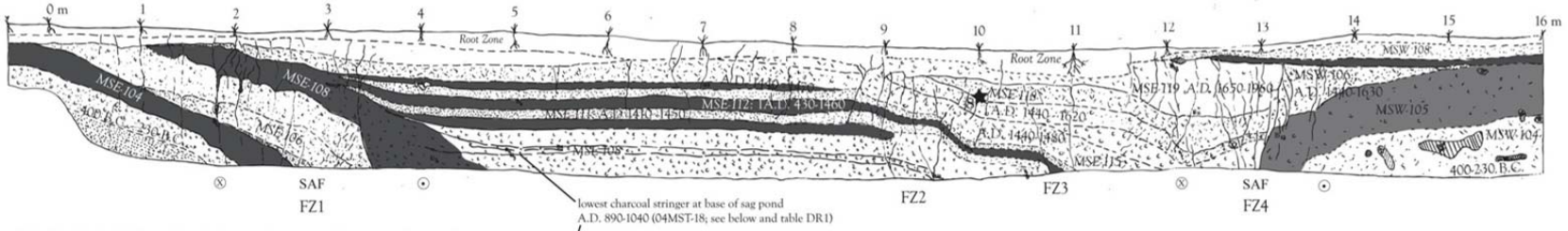

b) 2007 Miller Sag Trench, southeast photolog mosaic

c) 2007 Miller Sag Trench, northwest wall (MST07nw; flipped about the horizontal axis for comparison with MST07se)

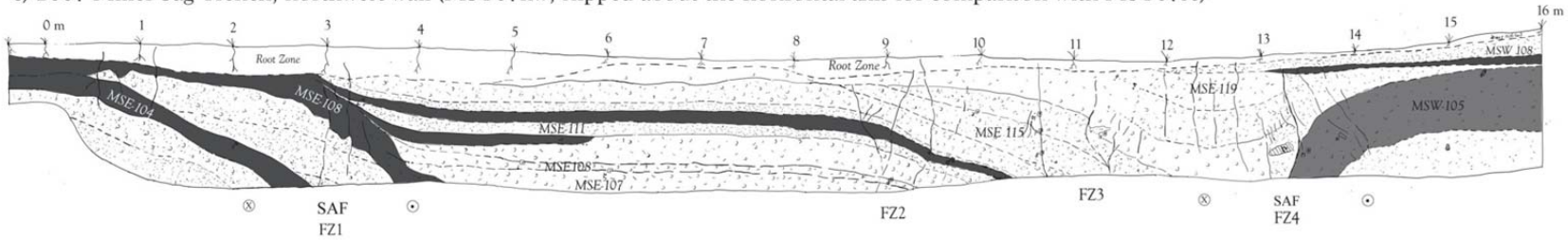

(d) 2004 Miller Sag Trench, southeast wall (MST04se).

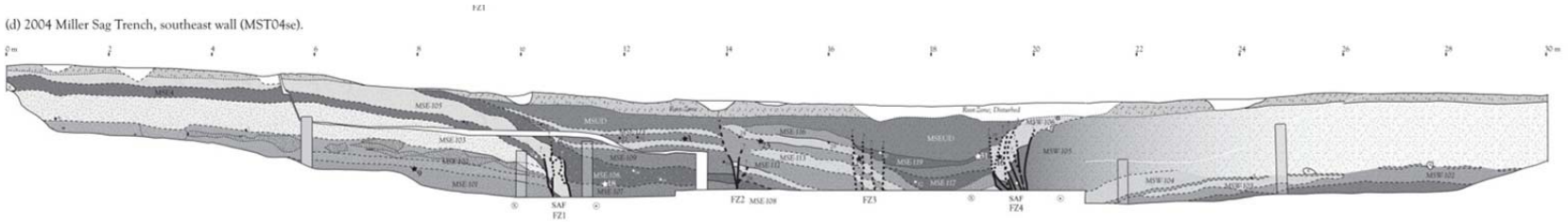

APPENDIX E

CHAPTER 3 SUPPLEMENTARY

MILLER'S FIELD SITE PRESSURE RIDGE TRENCH FIGURES 2004-2007

Figure E1.: Pressure Ridge Trenches (PT). Trench logs for the southeast (A; PT07se) and northwest (B; PT07nw) walls of the 2007 field season reveal the same stratigraphic sequence as the 2004 field season (C; PT04nw); for locations see Fig. 2.2. The stratigraphy displays oblique right-lateral deformation of fluvial overbank deposits and buried soil horizons (PTE-039). Units and deformation features are consistent between the 2004 and 2007 PT trenches, however here we have renamed the units. Please refer to Toke et al., 2006 to compare the unit naming changes and detailed descriptions of the units. Radiocarbon analyses are presented in Appendix C. On panel A, we provide the eight unit ages (those determined not to contain a significant detrital signal) amalgamated from both the 2004 and 2007 PT radiocarbon analyses. Non-detrital radiocarbon sample locations are denoted by bold black stars and numbering. Samples that have not contributed to the age chronology are denoted by smaller stars and numbering. SAF deformation along the pressure ridge is localized to one fault zone. This fault zone doubles in width in the upper 2m of the soil column and displays oblique clary shear bands (Appendix F) as well as significant oblique right-lateral offset; juxtaposing many different thicknesses of unit PTE-039. See Appendix D for logging explanation.

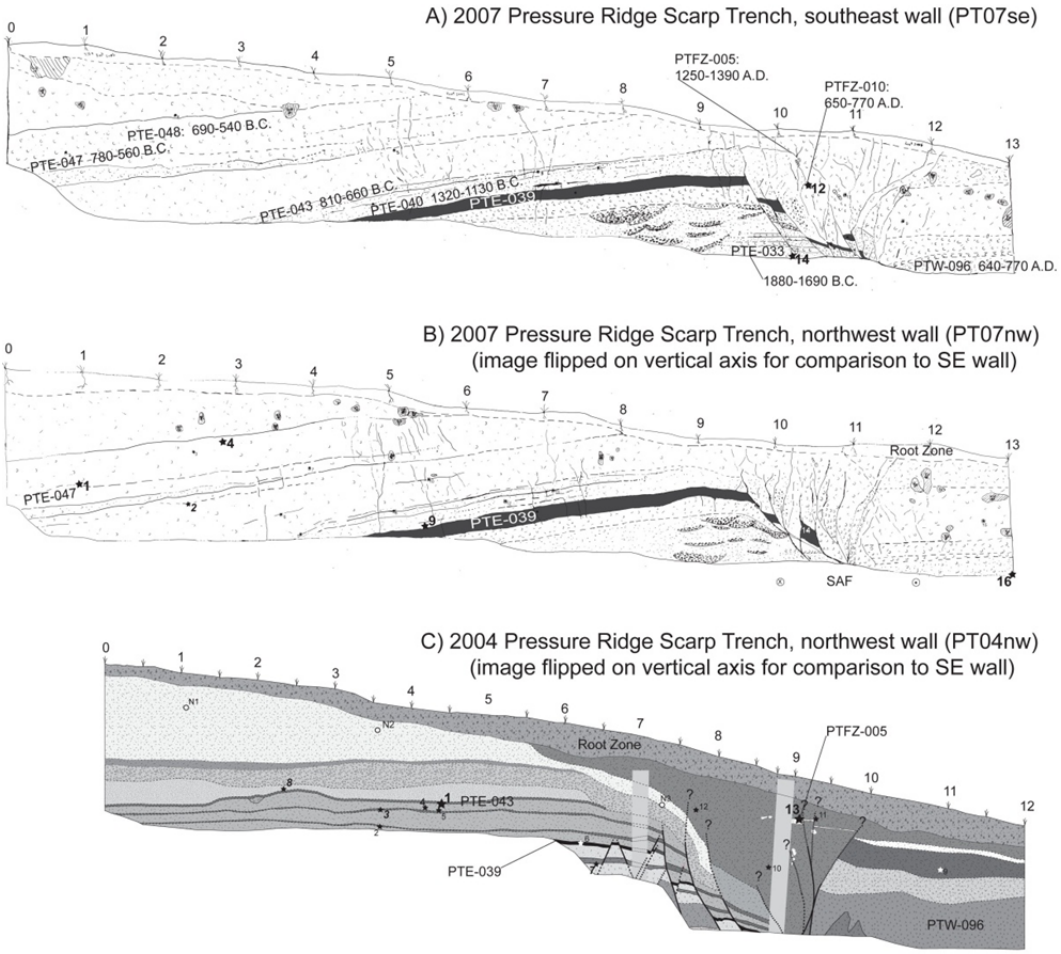
A) 2007 Pressure Ridge Scarp Trench, southeast wall (PT07se)
PTFZ-005:
1250-1390 A.D.
PTFZ-010:
650-770 A.D.
PTE-048: 690-540 B.C.
PTE-047 780-560 B.C.
PTE-043 810-660 B.C.
PTE-040 1320-1130 B.C.
PTE-039
PTE-033
1880-1690 B.C.
PTW-096 640-770 A.D.
B) 2007 Pressure Ridge Scarp Trench, northwest wall (PT07nw)
(image flipped on vertical axis for comparison to SE wall)
Root Zone
PTE-047
PTE-039
SAF
C) 2004 Pressure Ridge Scarp Trench, northwest wall (PT04nw)
(image flipped on vertical axis for comparison to SE wall)
Root Zone
PTFZ-005
PTE-043
PTE-039
PTW-096

APPENDIX F

CHAPTER 3 SUPPLEMENTARY:

PHOTOGRAPHS OF OBLIQUE FAULTS IN PALEOSEISMIC TRENCHES

Figure F1. Multiple clay shear band oblique deformation structures exposed in (A) MST07 and (B) PT07. (C) The 2004 Parkfield earthquake ruptured the surface as left stepping oblique en echelon opening mode surface fractures that grew via post-seismic afterslip (black fracture lines in C). A photo (D) of these surface cracks along the south side of the sag pond step-over with a field clip board for scale. We interpret that the oblique fault zone structures exposed within these paleoseismic trenches are a legacy of many moderate magnitude surface ruptures and aseismic creep.

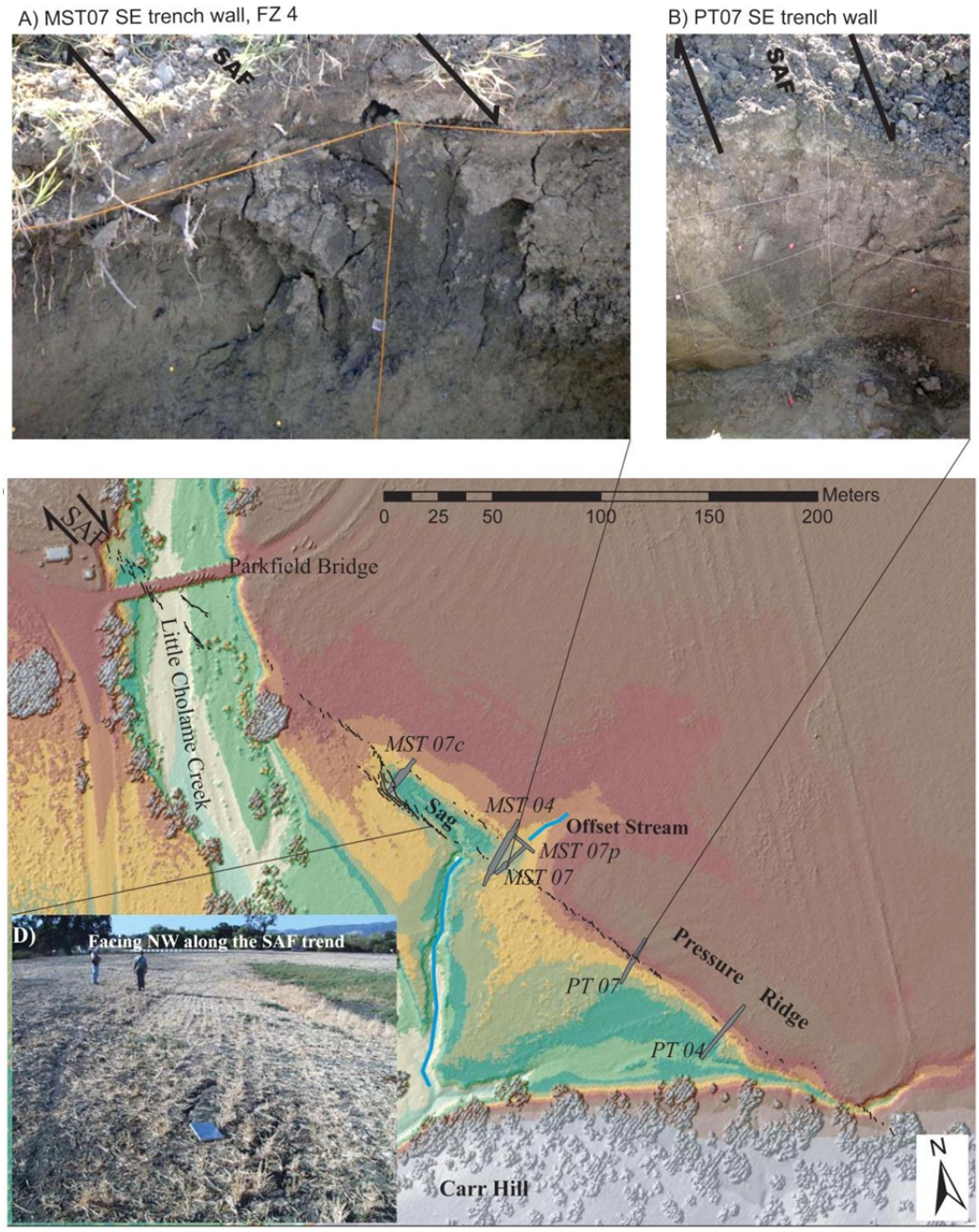
A) MST07 SE trench wall, FZ 4
SAF
B) PT07 SE trench wall
SAF
Meters
0 25 50 100 150 200
SAF
Parkfield Bridge
Little Cholame Creek
MST 07c
Sag
MST 04
Offset Stream
MST 07p
MST 07
Pressure Ridge
PT 07
PT 04
Carr Hill
N
D)
Facing NW along the SAF trend

APPENDIX G

CHAPTER 3 SUPPLEMENTARY:

SLIP RATE CALCULATION TABLE AND FIGURES

TableG1. Slip Rate Calculations

Measurement	Mean	Mode	Median	Bounds
		Gaussian Age and Displacement PDF Combinations*		
1-Sigma†				
Displacement (m)	20.75	20.75	20.75	+0.77 / -0.77
Age of displacement (ka)	0.79	0.79	0.79	+0.08 / -0.08
Slip rate (mm/year)	26.4	25.7	**26.2**	**+3.0 / -2.5**
2-Sigma†				
Displacement (m)	20.75	20.74	20.76	+2.15 / -2.15
Age of displacement (ka)	0.84	0.84	0.84	+0.27 / -0.27
Slip rate (mm/year)	25.4	23.6	**24.8**	**+11.9/ -6.4**
		Box Car Age and Displacement PDF combinations		
1-Sigma†				
Displacement (m)	20.75	18.5	20.75	+1.54 / -1.54
Age of displacement (ka)	0.79	0.56	0.79	+0.16 / -0.16
Slip rate (mm/a)	26.9	22.5	**26.2**	**+6.4 / -4.4**
2-Sigma†				
Displacement (m)	20.75	18.5	20.75	+2.15 / -2.15
Age of displacement (ka)	0.84	0.56	0.84	+0.27 / -0.27
Slip rate (mm/year)	25.8	20.6	**24.8**	**+12.6 / -6.9**
		Mixed Gaussian (Displacement) and Box Car (Age) PDF Combinations		
1-Sigma†				
Displacement (m)	20.75	20.75	20.75	+0.77 / -0.77
Age of displacement (ka)	0.79	0.56	0.79	+0.16 / -0.16
Slip rate (mm/a)	26.9	21.8	**26.2**	**+6.4 / -4.3**
2-Sigma†				
Displacement (m)	20.75	20.74	20.76	+2.15 / -2.15
Age of displacement (ka)	0.84	0.56	0.84	+0.27 / -0.27
Slip rate (mm/year)	25.7	20.3	**24.8**	**+12.2 / -6.6**
		Mixed Gaussian (Age) and Box Car (Displacement) PDF Combinations		
1-Sigma†				
Displacement (m)	20.75	18.5	20.75	+1.54 / -1.54
Age of displacement (ka)	0.79	0.79	0.79	+0.08 / -0.08
Slip rate (mm/year)	26.4	25.7	**26.2**	**+3.3 / -2.8**
2-Sigma†				
Displacement (m)	20.75	18.5	20.75	+2.15 / -2.15
Age of displacement (ka)	0.84	0.84	0.84	+0.27 / -0.27
Slip rate (mm/year)	25.5	23.7	**24.8**	**+12.0 / -6.6**

Note: Calculations were made using the slip rate software package of Zechar and Frankel, 2009. For visualization see below.

* Probability Density Functions

† The 1 and 2 sigma values (mean, mode, median) for age of offset depend upon the corresponding radiocarbon range (Appendix C).

Figure G1. The following four panels display all the permutations I ran (Guassian, boxcar, Age, and Displacement) for calculating slip rate probability density functions (PDFs) from the Miller's Field offset channel using the slip rate software of Zechar and Frankel (2009). The preferred slip rate PDF combination is a Gaussian Displacement PDF with a boxcar Age PDF (see Chapter 3 text, Panel D, and Fig. 3.4). Sigma bounds, median, mean, and modes for slip rate, displacement, and age of displacement are provided above. Radiocarbon age ranges are provided in Fig. 3.3 and Appendix C.

A) Slip Rate PDFs from Guassian Age and Displacement PDFs

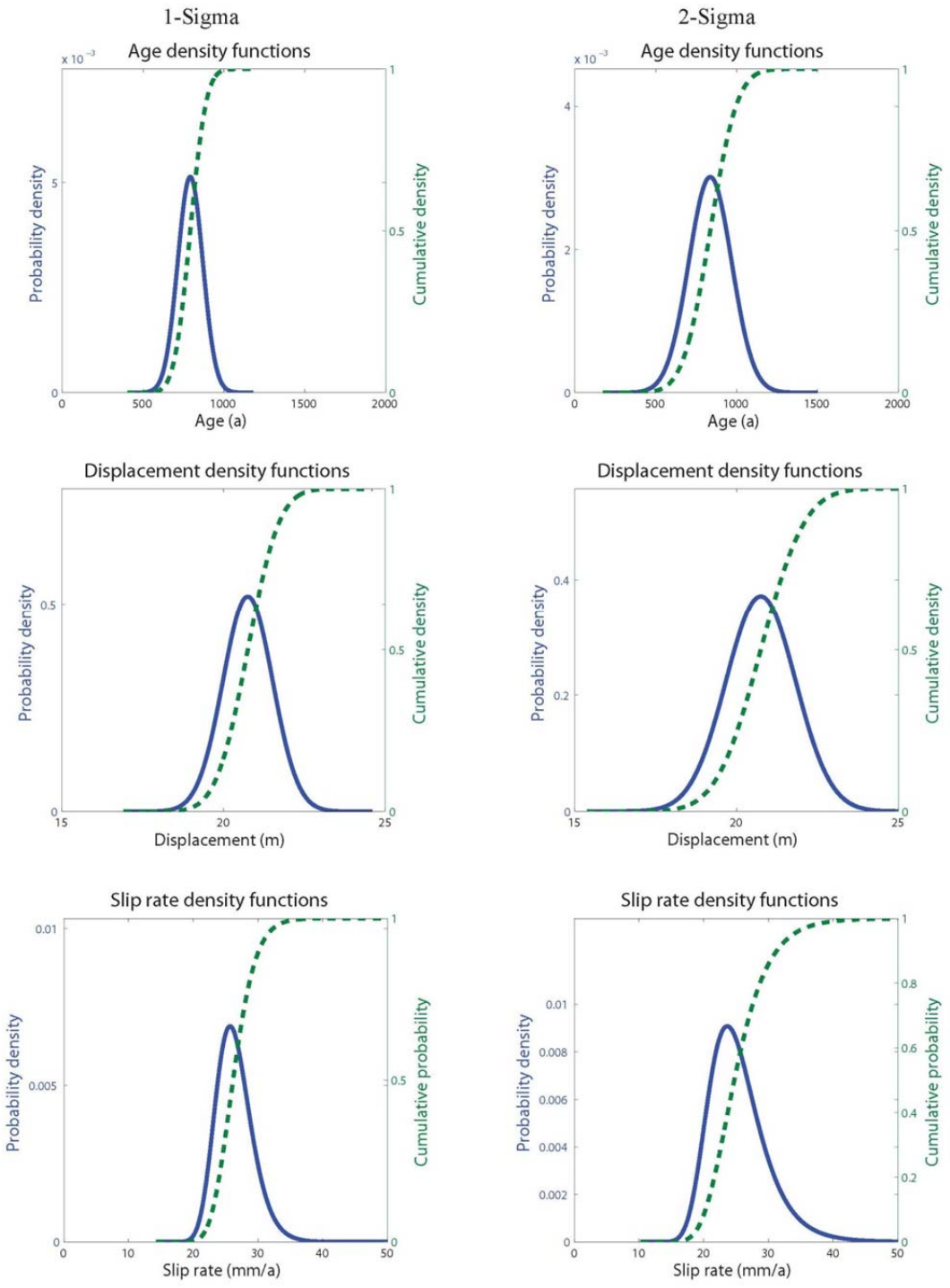

B) Slip Rate PDFs from Box Car Age and Displacement PDFs

1-Sigma

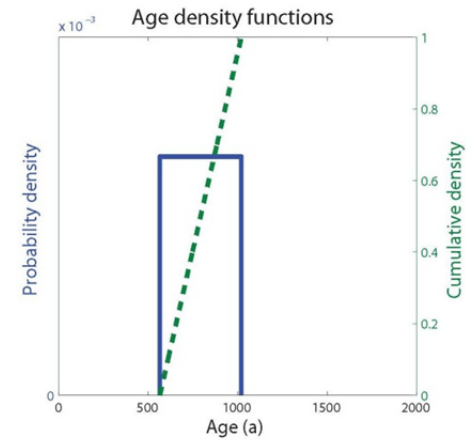

2-Sigma

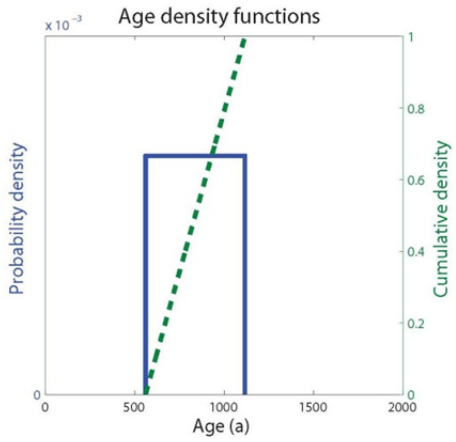

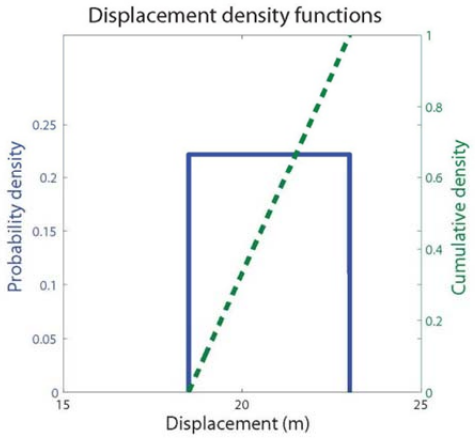

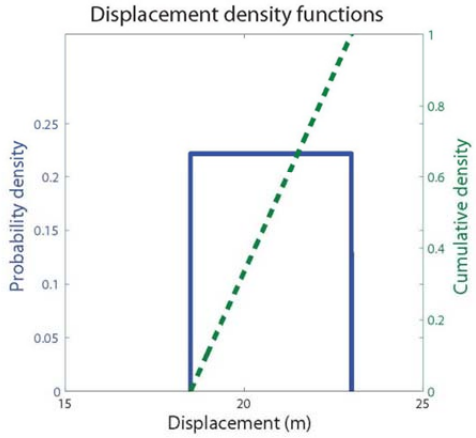

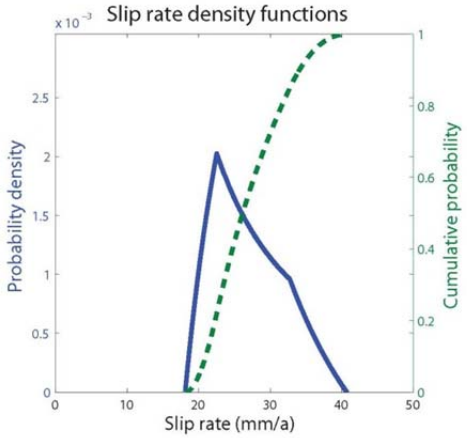

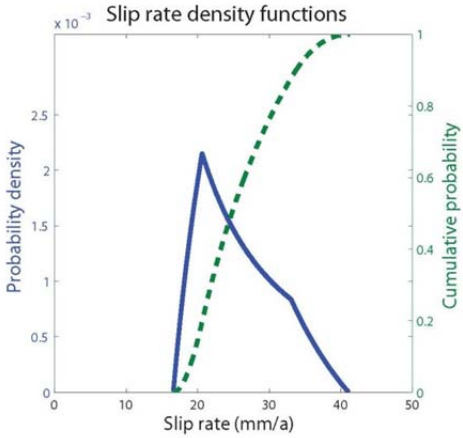

C) Slip Rate PDFs from Guassian Age and Displacement PDFs

1-Sigma

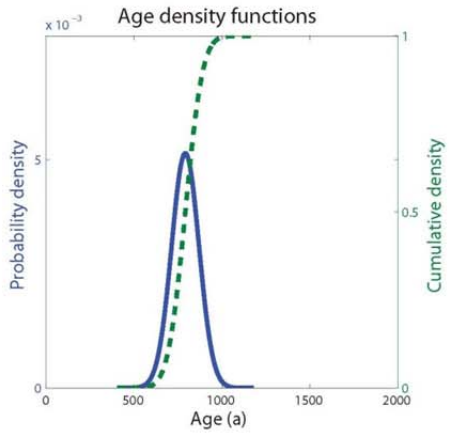

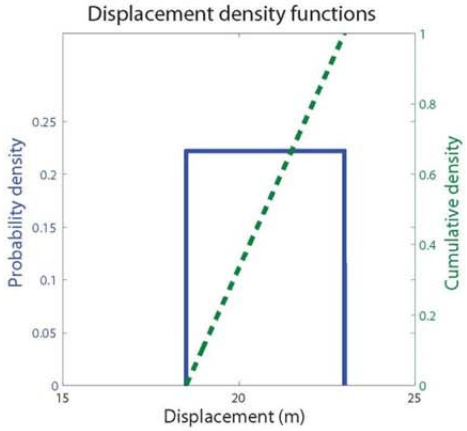

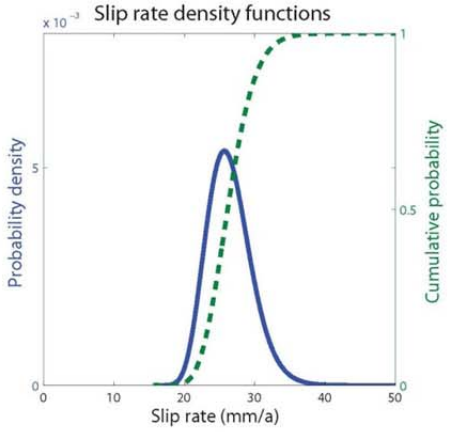

2-Sigma

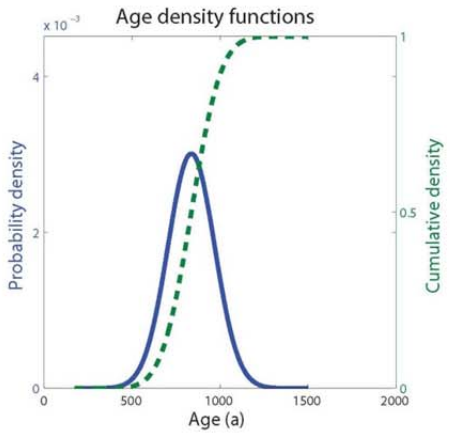

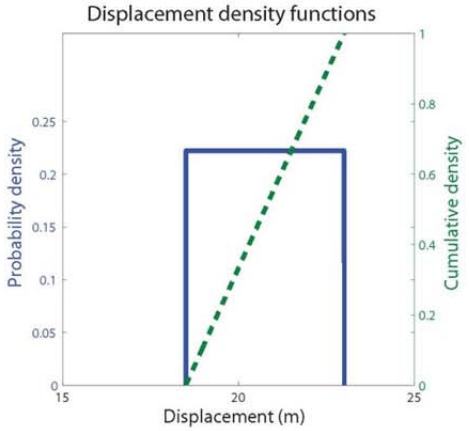

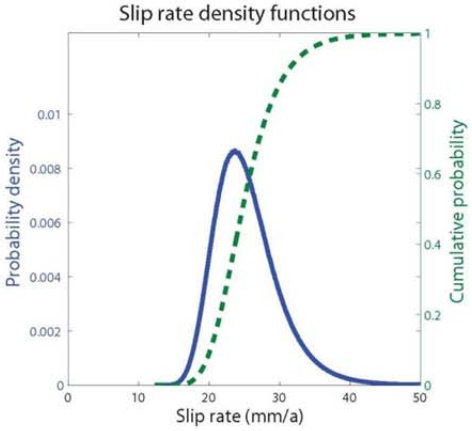

D) Slip Rate PDFs from Box Car Age and Displacement PDFs

1-Sigma

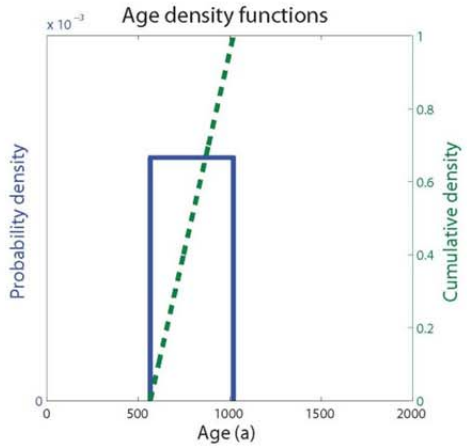

2-Sigma

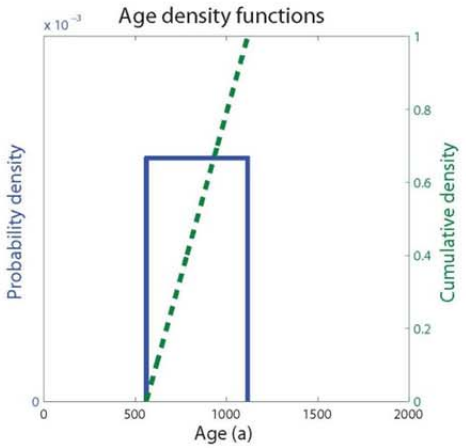

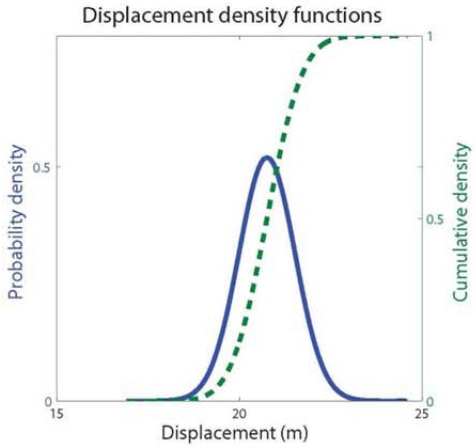

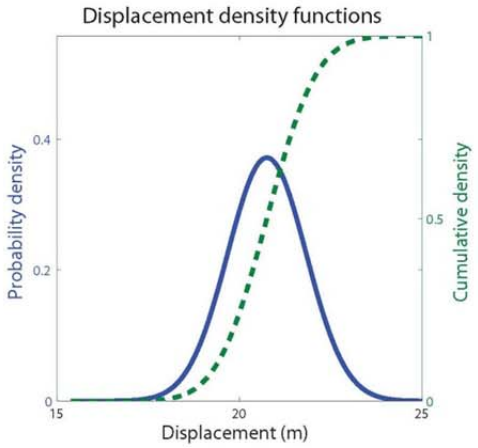

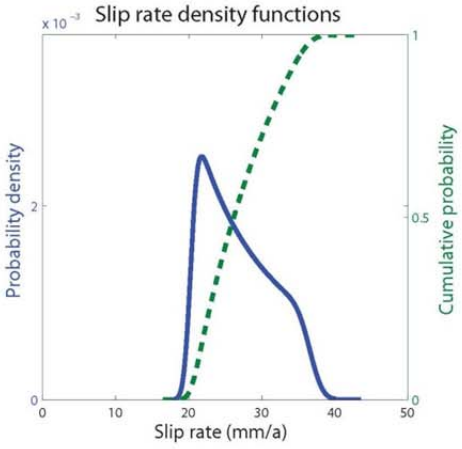

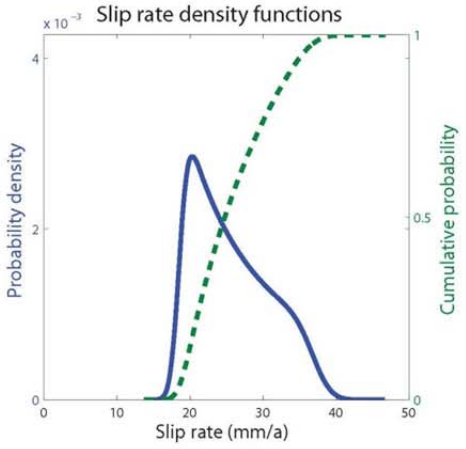

APPENDIX H

CHAPTER 4 SUPPLEMENTARY

TABLE OF LOCATIONS OF PALEOSEISMIC SITES AND GEOMORPHIC OFFSETS

TABLE H. Locations (decimal degrees) of geomorphic offsets and potential paleoseismic sites along the central San Andreas Fault from Bidart Fan site to the northwest extent of the B4 data set. Offset estimates are given to the nearest meter for those displaced less than 20 meters and to the nearest 5 meters for larger offsets. These offsets were measured using the ArcGIS measurement tool and are not meant to replicate the quantitative work of Zielke et al., 2010, but rather to document the location of offsets of different magnitudes and their relationship to existing and potential paleoseismic sites. A description of the type of landform that is offset is provided. The site notes column provides a brief synopsis of the potential paleoseismic sites identified along this mapping reach. Entries that do not contain site notes were not deemed promising for paleoseismic investigation. For those that were, I provide a general quality rating of their potential for paleoseismic investigation. This is a highly subjective rating that is largely based upon the potential for preservation of rupture evidence within recent sedimentation. Already existing sites are labeled as such. Locations along the main SAF are labeled with an (a), secondary structures are labeled with increasing numbers corresponding to each subsidiary structures that was mapped from southeast to northwest.

ID	Lat	Long	Distance NW of Bidart Fan (m)	Description	Offset Estimate (m)	Quality Rating	Main SAF?	Site Notes
1	35.23314178700	-119.78761929700	0.00	offset channel, multiple traces	4	existing	a	Bidart Fan
2	35.23375857090	-119.78823364100	88.38	offset channel and sag, multiple traces	10	existing	a	Bidart Fan
3	35.23428756530	-119.78874611400	163.31	offset channel	20		a	next to Bidart Fan
4	35.23899644450	-119.78779779700	501.59	offset channel subsidiary fault	3	promising	b	FScarp CZ, Pos. Offset, Test Dist. Slip, 400m NE
5	35.23939166510	-119.79410655200	910.08	offset channel	5		a	
6	35.24322148660	-119.79219445100	1118.16	offset channel? subsidary fault	1	questionable	b	FScarp CZ, Pos. Offset, Test Dist. Slip, 400m NE
7	35.24357413550	-119.79253615800	1168.12	offset channel? subsidary fault	2	questionable	b	FScarp CZ, Pos. Offset, Test Dist. Slip, 400m NE
8	35.24423089430	-119.79921685100	1622.58	offset channel	25		a	
9	35.24801407280	-119.80321459900	2178.27	offset channel?	35	questionable	a	
10	35.24907063950	-119.80429482700	2331.27	offset channel	9		a	
11	35.24950872900	-119.80483733600	2400.41	NO	0	promising	a	CZ, main SAF, simple fan strat
12	35.25144220340	-119.80696973000	2689.74	offset channel	25		a	
13	35.25179837400	-119.80715782600	2730.75	offset channel	5		a	
14	35.25188588730	-119.80727072600	2744.83	offset channel	20		a	
15	35.25197340040	-119.80738362600	2758.92	offset channel?	5	questionable	a	

ID	Lat	Long	Distance NW of Bidart Fan (m)	Description	Offset Estimate (m)	Quality Rating	Main SAF?	Site Notes
16	35.25206014860	-119.80752946500	2774.93	offset channel?	20		a	
17	35.25311514090	-119.80867567900	2931.76	buried offset	7	existing	a	PHelan Fan Site (Grant and Sieh, 1993)
18	35.25364352510	-119.80921037000	3007.97	offset fan head	70	promising	a	CZ, main SAF, slip rate site
19	35.25381778190	-119.80946911800	3037.90	offset fan head	105	promising	a	CZ, main SAF, slip rate site
20	35.25539857480	-119.81125989500	3276.68	large offset fan surface	340	promising	a	CZ, main SAF, long slip rate
21	35.25769369900	-119.81333917700	3593.56	NO	0	promising	a	CZ, main SAF, closed basin, fan strat
22	35.25910810710	-119.81453095300	3783.69	offset channel	20		a	
23	35.25945863940	-119.81496066700	3838.57	offset channel	15		a	
24	35.25955304650	-119.81477711900	3836.41	offset channel	3		a	
25	35.26015944300	-119.81583108400	3949.53	offset	125	promising	a	CZ, main SAF, filled offset channel, slip rate
26	35.26060105430	-119.81622000600	4009.78	offset channel	230		a	
27	35.26095311460	-119.81658385200	4061.00	offset channel	230		a	
28	35.26438999000	-119.81994484300	4549.60	NO	0	promising	a	CZ, main SAF, closed basin, fan strat
29	35.26764330180	-119.82344262500	5030.89	offset channel	80		a	
30	35.26834634470	-119.82421437300	5135.84	offset channel	8		a	

ID	Lat	Long	Distance NW of Bidart Fan (m)	Description	Offset Estimate (m)	Quality Rating	Main SAF?	Site Notes
31	35.26887541940	-119.82471632200	5210.18	offset channel	9		a	
32	35.26922796340	-119.82505828000	5260.13	offset channel	11		a	
33	35.26931417450	-119.82522613100	5277.38	offset channel	30		a	
34	35.26948993250	-119.82541907400	5303.61	offset channel	55		a	
35	35.26966723020	-119.82554613000	5326.17	offset channel	11		a	
36	35.26993022440	-119.82586300100	5367.07	offset channel	11		a	
37	35.27010598130	-119.82605594800	5393.31	offset channel	22		a	
38	35.27028327820	-119.82618300600	5415.69	offset channel	5		a	
39	35.27125391390	-119.82707401300	5550.25	offset channel	140	existing	a	Wallace Creek Site
40	35.27160234050	-119.82759169900	5610.24	offset channel	75		a	
41	35.27186738380	-119.82782073100	5646.15	offset channel	45		a	
42	35.27274717450	-119.82874158800	5774.84	offset channel	150		a	
43	35.27292189810	-119.82897847500	5803.58	offset channel	115		a	
44	35.27327545620	-119.82927654100	5850.87	offset channel	75		a	
45	35.27537157640	-119.83214124800	6198.16	large offset fan surface	540	promising	a	CZ, main SAF, long slip rate WCfan
46	35.27678756980	-119.83325674300	6383.77	large offset fan surface	540	promising	a	CZ, main SAF, long slip rate WCfan
47	35.28805393260	-119.84094879900	7791.13	Not apparent	0	promising	b	CZ, sub. fault, fan strat., nearby offsets
48	35.28944450950	-119.84314106300	8037.72	offset channel?	3	questionable	b	CZ, sub. fault offset
49	35.28955017000	-119.84631075800	8228.65	offset channels	50		a	

ID	Lat	Long	Distance NW of Bidart Fan (m)	Description	Offset Estimate (m)	Quality Rating	Main SAF?	Site Notes
50	35.29060758650	-119.84733718800	8378.62	offset channel	35		a	
51	35.29271850440	-119.84955489700	8687.76	offset channel	55		a	
52	35.29606296430	-119.85297038900	9171.89	offset channel	45		a	
53	35.30907998320	-119.86660051200	11075.75	offset channel	35		a	
54	35.30946194280	-119.86949486500	11273.42	offset channel subsidary fault	4		c	
55	35.30981434070	-119.86983719100	11323.41	offset channel subsidary fault	4		c	
56	35.31093101880	-119.86835923500	11336.74	NO	0	questionable	a	CZ, main SAF, basin, pos. hum. dist.
57	35.33065085700	-119.88807275000	14165.60	NO	0	promising	a	CZ, main SAF, basin, F. complex, good?
58	35.35047848700	-119.91064925900	17163.88	offset channel subsidary fault?	2	questionable	c	
59	35.35954952730	-119.91571704600	18242.05	offset channel?	4	questionable	a	
60	35.36181279150	-119.91903325900	18625.34	offset channel?	50	questionable	a	
61	35.38100225340	-119.93794951200	21362.78	Probably	0	promising	a	Chol, main SAF, complex, hanging basin, offset?
62	35.38671269120	-119.94402291200	22201.59	Many small	0	promising	a	Chol, main SAF, complex, hanging basin,.

ID	Lat	Long	Distance NW of Bidart Fan (m)	Description	Offset Estimate (m)	Quality Rating	Main SAF?	Site Notes
63	35.40013489120	-119.95905243200	24211.49	NO	0	promising	a	Chol, main SAF, basin, could be good.
64	35.40904471780	-119.96691946200	25431.69	NO	0	promising	a	Chol, main SAF, basin, could be good.
65	35.45067687700	-120.00361755500	31124.62	offset channel?	20	questionable	a	
66	35.45074992830	-120.00430317000	31169.60	offset channel?	10	questionable	a	
67	35.45897685170	-120.01051364800	32234.43	offset channel?	40	questionable	a	
68	35.46408934030	-120.01511082900	32938.10	offset channel	6		a	
69	35.46955572430	-120.01996422800	33686.79	Not apparent	0	existing	a	LY4 site (Stone et al., Young et al., 2002)
70	35.49197145380	-120.04249096400	36907.90	offset channel	50		a	
71	35.49552233310	-120.04820132100	37539.79	offset channel?	15	questionable	a	
72	35.49664399600	-120.04661267900	37543.91	Not apparent	0	promising	a	Chol, main SAF, basin, complex not all slip
73	35.49885851080	-120.04814011400	37821.62	offset channel	50		a	

ID	Lat	Long	Distance NW of Bidart Fan (m)	Description	Offset Estimate (m)	Quality Rating	Main SAF?	Site Notes
74	35.50596485070	-120.05579353500	38872.27	offset channel?	10	questionable	a	
75	35.50874577900	-120.05985597600	39344.53	offset terrace?	20	questionable	a	
76	35.54171372970	-120.09231445700	44042.30	offset channel	10		a	
77	35.57580722480	-120.12617885600	48916.10	probably	0	promising	a	Chol, main SAF, basin, pos. offset channel
78	35.58369713620	-120.13468278200	50082.59	offset channel?	4	questionable	a	
79	35.58993331500	-120.14091709100	50976.40	offset channel?	20	questionable	a	
80	35.59054742020	-120.14155896100	51066.03	offset fan	20		a	
81	35.59309440640	-120.14410802000	51431.18	offset channel	25		a	
82	35.59414481820	-120.14529664100	51589.93	offset channel	4		a	
83	35.59415057700	-120.14507619200	51602.71	offset channel?	4	questionable	a	
84	35.59564680290	-120.14644781400	51809.51	offset channel	45		a	
85	35.59573078240	-120.14668281600	51830.53	offset channel	15		a	
86	35.59581793070	-120.14679656900	51844.60	offset channel	5		a	
87	35.59748323780	-120.14859417800	52091.05	offset channel	120		a	
88	35.59976515680	-120.15093467200	52421.48	offset channel?	25		a	
89	35.60555975020	-120.15679003500	53254.54	offset channel	45		a	
90	35.60588343010	-120.15819320600	53364.22	offset channel	55		a	
91	35.60625424250	-120.15779948600	53371.76	offset channel	40		a	
92	35.60659063840	-120.15871761600	53454.22	offset channel	135		a	

ID	Lat	Long	Distance NW of Bidart Fan (m)	Description	Offset Estimate (m)	Quality Rating	Main SAF?	Site Notes
93	35.60712010250	-120.15914675900	53524.22	offset channel	60		a	
94	35.60791472920	-120.15977394700	53627.81	offset channel	4		a	
95	35.60861845580	-120.16043067700	53725.89	offset channel	30		a	
96	35.60967128720	-120.16152052500	53878.93	offset channel	90		a	
97	35.61186752240	-120.16368180700	54191.43	offset channel	40		a	
98	35.61195291360	-120.16386174900	54209.29	offset channel	40		a	
99	35.61203859440	-120.16403066800	54226.52	offset channel?	4	questionable	a	
100	35.61641059630	-120.16912538500	54896.19	offset channel	5		a	
101	35.61896445540	-120.17138949600	55241.38	offset channel?	10	questionable	a	
102	35.61930829180	-120.17202116000	55307.05	offset channel	30		a	
103	35.62019170250	-120.17269623800	55421.62	offset channel	65		a	
104	35.62052535600	-120.17371381800	55506.96	offset channel?	15	questionable	a	
105	35.62168668610	-120.17410191100	55629.14	offset channel	25		a	
106	35.62177031520	-120.17434804200	55650.44	offset channel?	10	questionable	a	
107	35.62255932070	-120.17518499500	55766.31	offset channel	50		a	
108	35.62273471900	-120.17536853600	55791.93	offset channel	30		a	
109	35.62422355390	-120.17700585500	56014.05	offset channel	70		a	
110	35.62464457280	-120.17812630500	56114.97	offset channel	5		a	
111	35.62873706210	-120.18354268500	56773.39	offset channel	10		a	
112	35.63046242160	-120.18304819400	56890.04	offset channel	110		a	
113	35.63125077300	-120.18390737900	57007.17	offset channel?	40	questionable	a	
114	35.63319076650	-120.18551880200	57265.52	offset channel	100		a	
115	35.63397938920	-120.18636701400	57382.04	offset channel	200		a	

ID	Lat	Long	Distance NW of Bidart Fan (m)	Description	Offset Estimate (m)	Quality Rating	Main SAF?	Site Notes
116	35.63722295850	-120.18979669500	57857.75	NO	0	questionable	a	Chol, main SAF, sag ponds small basins
117	35.64010456040	-120.19327848500	58305.74	offset channel?	10	questionable	a	
118	35.64131630430	-120.19515938800	58518.56	offset channel?	7	questionable	a	
119	35.64306640180	-120.19712805800	58782.10	offset channel?	10	questionable	a	
120	35.64491410970	-120.19881365800	59037.32	offset channel?	5	questionable	a	
121	35.64729694410	-120.20070839700	59349.90	offset channel	30		a	
122	35.64764941010	-120.20100953300	59397.38	offset channel	40		a	
123	35.64887686960	-120.20229514700	59576.61	offset channel	8		a	
124	35.65536254480	-120.20916840900	60528.08	offset channel?	20	questionable	a	
125	35.67883680400	-120.23446348600	63991.72	offset channel?	45	questionable	a	
126	35.68411447050	-120.23927176800	64721.65	NO	0	promising	a	Chol, main SAF, sag pond, small basin
127	35.70674529100	-120.26218636700	67977.39	offset channel?	105	questionable	a	
128	35.71241772180	-120.26900332800	68849.82	offset channel?	70	questionable	a	
129	35.71575607140	-120.27216752800	69315.15	offset channel	80		a	
130	35.72003215020	-120.27729323200	69957.57	offset channel	5		a	
131	35.72187220720	-120.27921416700	70222.19	offset channel	105		a	
132	35.72468672700	-120.28174986100	70607.71	offset channel	3		a	
133	35.74013792570	-120.29341578500	72621.63	offset channel?	3		a	
134	35.74278265140	-120.29555871500	72973.16	offset channel?	20	questionable	a	PKF, main SAF, slip rate site?
135	35.75236578340	-120.30427864600	74293.65	offset channel	7		a	
136	35.75323888220	-120.30529868700	74424.76	offset channel	2		a	

ID	Lat	Long	Distance NW of Bidart Fan (m)	Description	Offset Estimate (m)	Quality Rating	Main SAF?	Site Notes
137	35.75324070470	-120.30523243100	74427.88	offset channel	1		a	
138	35.75622546550	-120.30810883200	74847.91	Offset fan?	0	promising	a	Water Tank Site (Sims)
139	35.79162497610	-120.32824698400	79037.72	offset channel?	2	promising	a	Also small sags, could be paleosite.
140	35.79465132610	-120.32960107800	79373.74	offset channel?	2	questionable	a	
141	35.80763692870	-120.34224609600	81213.04	offset channel?	7		a	
142	35.81765885870	-120.34802153200	82385.44	Not apparent	0	promising	a	Pkf, main SAF, sag ponds with source
143	35.82143823500	-120.35144442700	82903.36	offset terrace	80		a	
144	35.82325246780	-120.35424269800	83223.05	offset terrace	80	promising	a	PKF, main SAF before SWFZ, Slip rate site
145	35.83874834450	-120.37045562300	85481.35	offset channel?	15	questionable	a	
146	35.84085600480	-120.37241522500	85773.24	offset channel?	2	questionable	a	
147	35.84992967530	-120.38300484100	87162.75	offset channel?	80	questionable	a	PKF, main SAF, possible slip rate site?
148	35.85421014010	-120.38779155400	87805.51	large offset channel?	750	questionable	a	PKF, main SAF, date age of channel fill.
149	35.87222681830	-120.41025916700	90648.27	offset channel	600	promising	a	PKF, main SAF, Date age of terrace, cosmo?
150	35.87337766070	-120.41098390500	90787.48	offset terrace?	2	questionable	a	

ID	Lat	Long	Distance NW of Bidart Fan (m)	Description	Offset Estimate (m)	Quality Rating	Main SAF?	Site Notes
151	35.87372383260	-120.41148590900	90846.55	offset channel	10		a	
152	35.87424748860	-120.41208410900	90925.94	offset channel	90	promising	a	date fan material for slip rate, others near
153	35.87468114020	-120.41267845300	90997.73	offset channel	160		a	
154	35.87730061070	-120.41562537600	91392.11	offset channel	200	promising	a	PKF, main SAF, slip rate by dating terrace fill
155	35.89251302260	-120.43198255200	93635.67	offset channel?	25	questionable	a	same as MF site sag channel?
156	35.89382090940	-120.43351194700	93836.13	offset channel	20	existing	a	Miller's Field Site (Toke et al.)
157	35.90861738980	-120.44857321700	95965.18	NO	0	questionable	a	PKF, main SAF, sag with source
158	35.91535257310	-120.45563405800	96947.74	offset channel	60		a	
159	35.94398756730	-120.48743261900	101232.02	offset channel	35		a	
160	35.94416336770	-120.48758440800	101255.73	offset channel	10		a	
161	35.99910775870	-120.55575001600	109915.56	offset channel?	10	questionable	a	
162	35.99989790480	-120.55645085500	110022.84	offset channel?	3		a	
163	36.04285089590	-120.60257406600	116350.81	offset channel	25		a	
164	36.04889614700	-120.61127128700	117376.58	offset channel?	240	questionable	a	
165	36.04958790430	-120.61223494700	117492.05	offset channel?	120	questionable	a	
166	36.05010939130	-120.61286906200	117573.42	offset channel?	40	questionable	a	
167	36.06203470390	-120.62672047400	119393.99	NO	0	questionable	a	creeping, main SAF, sag pond

BIOGRAPHICAL SKETCH

Nathan Toké (pronounced Toe-Kay) was born October 21st, 1980 in Randolph, Vermont to Carolyn Garland and Arun Toké. As a child Nathan spent many days outside exploring the forests, streams, and other aspects of the local landscape. Nathan attended People's Academy High School in Morrisville, Vermont where he graduated in 1999 as Salutatorian. He then moved on to the University of Vermont with a Vermont Scholar's Award, was a member of the John Dewey Honors Program, and graduated cum laude in May 2003 with a B.S. in Geology. Working with Paul Bierman, Nathan wrote an honors thesis studying the impact of urbanization on soil infiltration capacity and storm water runoff chemistry. In the summer following UVM Nathan attended the University of Arizona's geology field camp and in August 2003 he moved to Tempe, AZ to begin a M.S. in Geological Sciences at Arizona State University. His Master's thesis working with Ramón Arrowsmith provided the first paleoseismic records for the Parkfield segment of the San Andreas Fault (SAF) and contributed a review of central SAF active tectonics using historical records of aseismic creep and earthquakes to construct a SAF slip budget. That research provided the background and motivation for chapters 2-3 of this dissertation. Following his M.S. Nathan returned to ASU to pursue a Ph.D. He was awarded an NSF IGERT in urban ecology fellowship which prompted him to further explore his interests in urban geoscience that were initially developed during his undergraduate thesis. Nathan found it difficult to separate himself from active tectonics research. As a result, he linked his interest in active tectonics and seismic hazards with coursework in urban geography and a study of feedbacks between seismic hazard, regulations, urban form and environmental justice. IGERT-sponsored workshops have also lead Nathan to develop research interests in interdisciplinary pedagogy and sustainable urban development. Nathan will begin his career as an Assistant Professor of Earth Science at Utah Valley University in August 2011 were he will continue to focus his efforts on the interfaces between the environment and society.